



# LUND UNIVERSITY

## Adhesive Joints in Timber Engineering. Modelling and Testing of Fracture Properties

Serrano, Erik

2000

[Link to publication](#)

*Citation for published version (APA):*

Serrano, E. (2000). *Adhesive Joints in Timber Engineering. Modelling and Testing of Fracture Properties*. [Doctoral Thesis (compilation), Structural Mechanics]. Division of Structural Mechanics, Lund University, PO Box 118, SE-221 00, LUND, Sweden,.

*Total number of authors:*

1

### General rights

Unless other specific re-use rights are stated the following general rights apply:

Copyright and moral rights for the publications made accessible in the public portal are retained by the authors and/or other copyright owners and it is a condition of accessing publications that users recognise and abide by the legal requirements associated with these rights.

- Users may download and print one copy of any publication from the public portal for the purpose of private study or research.
- You may not further distribute the material or use it for any profit-making activity or commercial gain
- You may freely distribute the URL identifying the publication in the public portal

Read more about Creative commons licenses: <https://creativecommons.org/licenses/>

### Take down policy

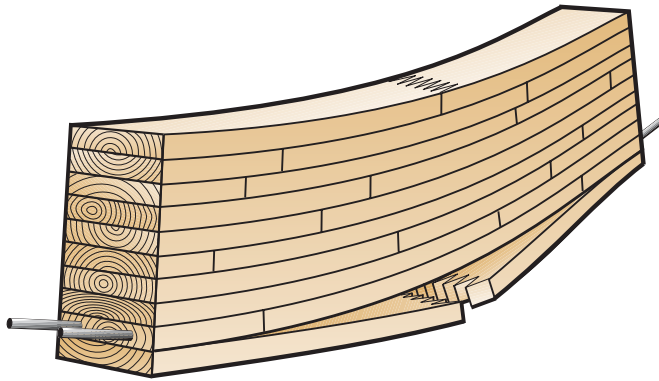
If you believe that this document breaches copyright please contact us providing details, and we will remove access to the work immediately and investigate your claim.

LUND UNIVERSITY

PO Box 117  
221 00 Lund  
+46 46-222 00 00



**LUND**  
UNIVERSITY



# **ADHESIVE JOINTS IN TIMBER ENGINEERING - MODELLING AND TESTING OF FRACTURE PROPERTIES**

ERIK SERRANO

Department  
of  
Mechanics  
and  
Materials

Structural Mechanics

*Doctoral Thesis*



*Department of Mechanics and Materials*  
Structural Mechanics

ISRN LUTVDG/TVSM--00/1012--SE (1-173)  
ISBN 91-7874-095-9 ISSN 0281-6679

ADHESIVE JOINTS IN  
TIMBER ENGINEERING  
- MODELLING AND TESTING  
OF FRACTURE PROPERTIES

Doctoral Thesis by  
ERIK SERRANO

Copyright © Erik Serrano, 2000.  
Printed by KFS i Lund AB, Lund, Sweden, October 2000.

For information, address:  
Division of Structural Mechanics, LTH, Lund University, Box 118, SE-221 00 Lund, Sweden.  
Homepage: <http://www.byggmek.lth.se>



*To Anna-Lena, Daniel  
and Alexander*

*To Signe, Anita and Alfonso*

“... as Rose collects the money in a canister  
who comes sliding down the banister  
the vicar in a tu-tu, he's *not* strange  
he just wants to live his life this way ...”

*'Vicar in a tutu', Morrissey*

# Acknowledgements

We all want to live our lives in our own ways, but this is not possible of course, without the help of others. Since I do not want to risk forgetting to mention anyone, I would first of all like to express my thanks to all of those who know or feel that they in some way have contributed to my thesis.

However, some persons have been more involved in my work than others. Thus, to all my supervisors, both present and former, I express my deepest gratitude. These include Dr. Per Johan Gustafsson, Adj. Prof. Hans Jørgen Larsen, Prof. Hans Petersson and Adj. Prof. Carl-Johan Johansson. It has been a pleasure and above all an honour to work with these internationally recognised experts, who have contributed to my work in so many ways; including their co-authoring of various of the papers presented, their encouragement and guidance, and their part in the fruitful discussions we have had within the areas of fracture mechanics and timber engineering.

Special thanks as well to Prof. Göran Sandberg, head of the Division of Structural Mechanics. During a somewhat chaotic period in my life, he made it possible for me to come back and once again enjoy the companionship of the Division of Structural Mechanics after a few months of “leave”.

The work presented in the thesis has been mainly carried out within two research projects. One of these has been supported by the Swedish Council for Building Research (BFR project no. 19960633) and the other project (GIROD) has been supported by the European Commission (DG XII) through grant no. SMT4-CT97-2199. This financial support from both sources is gratefully acknowledged. The GIROD-project has been coordinated by SP – the Swedish National Testing and Research Institute. Apart from Lund University, the Otto-Graf Institute at the University of Stuttgart (Germany), the University of Karlsruhe (Germany) and TRADA Technology (UK) have been involved. The co-operation of all these partners in the research project is also gratefully acknowledged.

Finally, a special thanks to Mr. Bertil Enquist and to Mrs. Rizalina Brillante for carrying out the major part of the test programmes. Without their skilful handling of the test specimens and testing machines, this work would never have been possible<sup>1</sup>.

Lund, October 2000

Erik Serrano

---

<sup>1</sup>Without experiments you will end up with a YAM!





# Abstract

This thesis, which is a compilation of seven papers, concerns the mechanical testing, numerical analysis and constitutive modelling of wood-adhesive bonds in timber engineering. Applications such as finger-joints, glued-laminated timber and glued-in rods are considered. The experimental studies include the testing of the fracture characteristics of wood-adhesive bonds, including both wood-to-wood bonds and glued-in rods of either steel or glass fibre reinforced polyester. The numerical studies relate to the strength of finger-joints, laminated beams and glued-in rods for timber structures.

In the experimental studies, the complete stress-displacement response of small specimens, particularly their fracture softening behaviour beyond peak stress, was recorded. A major outcome from the experiments is that wood-adhesive bonds can behave in a fracture-softening manner, and that it is possible to record this under stable conditions.

In one of the numerical studies the finite element method was employed to analyse the stress distribution around zones of low stiffness in a laminated beam. A fracture mechanics analysis was also performed of the delamination of a laminated beam. The results show that the often made assumption of a stress redistribution taking place around weak zones is not necessarily true. Another finding is that the delamination of an initially cracked glulam beam tends to be increasingly dominated by mode II failure as the lamination thickness decreases.

In another study, also related to finger-joints and laminated beams, the finger-joint failure in a glulam beam was simulated using a nonlinear fictitious crack model with stochastic properties. The results show the proposed approach to be able to account for such phenomena as the size effect and the laminating effect. Another observation is that finger-joint fracture energy, i.e. the ductility, has a major influence on lamination and beam strength. The influence of bondline defects on the tensile strength of a finger-joint was also investigated. It was demonstrated that even a small defect in the form of a glue-line void, can have a relatively strong influence on the tensile strength. It was also demonstrated that the strength of finger-joints is largely influenced by the outermost finger.

A nonlinear 3D finite element model was employed in a parameter study of glued-in rods in timber structures, a strain-softening model being used to characterise the adhesive layer. Parameter studies in relation both to the fracture energy and the geometrical parameters and to loading conditions were performed. The results show that the fracture energy is of major importance for the pull-out load capacity, that the model in question can be used to predict size effects and that loading in a pull-compression manner results in lower load-bearing capacities than loading in a pull-pull manner.

Finally, an interface model based on damage mechanics is suggested for the modelling of wood-adhesive interfaces. This model accounts for joint dilatation and post-cracking friction. Also, a homogenisation scheme is presented for combining the proposed model with ordinary plasticity models for the adhesive bulk. This homogenisation procedure is based on assumptions regarding the stress and strain gradients typical of thin bondlines.

**Keywords:** adhesive, bending strength, constitutive modelling, damage, experiment, finger-joint, finite element method, fracture mechanics, glued-in rod, glued-laminated timber, joint, laminated beams, laminating effect, numerical simulation, size effect, stress distribution, tensile strength, test method, wood



# Contents

<b>I</b>	<b>Introduction and Overview</b>	<b>1</b>
<b>1</b>	<b>Introduction</b>	<b>3</b>
1.1	Adhesive Joints in Timber Engineering . . . . .	3
1.2	Background . . . . .	4
1.3	Organisation of the Thesis . . . . .	6
<b>2</b>	<b>Overview of Present Study</b>	<b>7</b>
2.1	Aim, Scope and Original Features . . . . .	7
2.2	Strategy and Methods . . . . .	8
2.3	Results and Discussion . . . . .	10
<b>II</b>	<b>Appended Papers</b>	<b>15</b>
<b>Paper I</b>	<i>“Numerical Investigations of the Laminating Effect in Laminated Beams”</i> . ASCE – Journal of Structural Engineering, 125(7) 740–745, 1999.	
<b>Paper II</b>	Chapters 3 and 4 from <i>“Finger-joints for Laminated Beams. Experimental and numerical studies of mechanical behaviour”</i> .	
<b>Paper III</b>	<i>“Influence of Bondline Brittleness and Defects on the Strength of Timber Finger-joints”</i> . International Journal of Adhesion and Adhesives, 19(1) 9–17, 1999.	
<b>Paper IV</b>	<i>“Modeling of Finger-joint Failure in Glued-laminated Timber Beams”</i> . Sub- mitted for publication, ASCE – Journal of Structural Engineering, 2000.	
<b>Paper V</b>	<i>“Glued-in Rods for Timber Structures. – A 3D Model and Finite Element Parameter Studies”</i> . Accepted for publication, International Journal of Ad- hesion and Adhesives, 2000.	
<b>Paper VI</b>	<i>“Glued-in Rods for Timber Structures. – An Experimental Study of Soft- ening Behaviour”</i> . Submitted for publication, Materials and Structures, 2000.	
<b>Paper VII</b>	<i>“A Damage-plasticity Modelling Approach for Wood Adhesive Bonds”</i>	



# **Part I**

## **Introduction and Overview**



# Chapter 1

## Introduction

### 1.1 Adhesive Joints in Timber Engineering

Wood-adhesive joints play an important role in modern timber engineering. In order to add value to the raw material, several highly engineered wood-based products have been developed. Often these involve the use of adhesive joints. Typical examples of such *re-constituted* materials are glued laminated timber (glulam) and laminated veneer lumber (LVL). In each of these, adhesive joints are used both for lengthwise splicing and for interlaminar bonding. Another example of an adhesive joint application in timber engineering is that of glued-in rods which allow stiff and strong beam-to-column connections or column foundations to be obtained.

In order to fully understand and model the behaviour of such structural elements as glulam beams, one must also understand the behaviour of their adhesive bondlines. Although adhesive bondlines often represent only a small part of a structural component, they are often crucial parts for the strength and the reliability of the structural component. A typical adhesive bondline in timber engineering has a thickness in the range of 0.1–1 mm, which is several orders of magnitude smaller than the scale of the structural components, one of approximately 0.1–10 m, Figure 1.1.

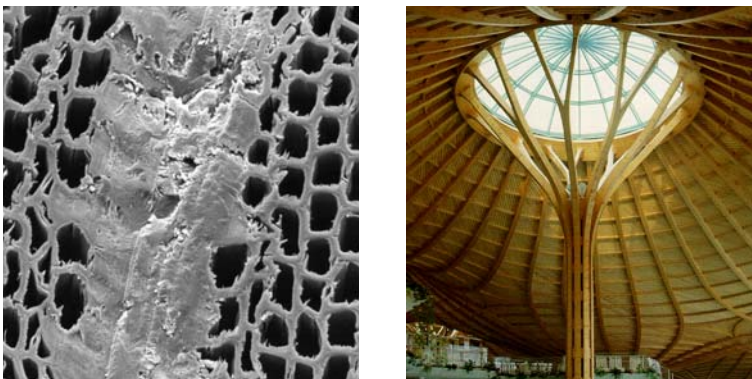


*Figure 1.1: Adhesive bonds based on phenol-resorcinol (left) are often used in the production of glued-laminated timber (right).*



The work presented in the thesis concerns experimental and numerical studies of mechanical behaviour on both these scales. The work also concerns new methods for bridging the gap between the two scales, making it possible to incorporate knowledge of the mechanical behaviour of a thin bondline into analysis on the structural-component-size scale.

## 1.2 Background

### 1.2.1 Wood As a Building Material

The advantages of using wood as a building material are well known: it has an attractive appearance, is easy to work with, its strength/weight ratio is high, it has comparatively good heat-insulation properties, it retains its strength for a reasonably long period of time if exposed to fire, it is a fully renewable building material and, finally, it is a building material that does not contribute to the green-house effect. There are certain well-known disadvantages, as well, in the use of wood. As a “living” material, its properties vary within a wide range; wood is also a highly anisotropic material, with low strength perpendicular to the grain; finally, wood is known to be sensitive to exposure to moisture.

The large variability in strength, for example, is due to more than simply variations between different trees and stands. Even within a single log, the variability can be extensive. This can be explained by the presence of such anomalies as reaction wood, knots, spiral grain and density variations. Differences in climate during the life of a tree, along with a variety of other factors, likewise influence the variability of the material properties within a log.

Even if one considers wood to be a homogeneous material, it is still a challenging task to measure the basic material properties that are needed for a simple linear elastic stress analysis. Wood is a highly anisotropic material that is often regarded as being orthotropic. The degree of anisotropy is extremely high; typical ratios of Young’s moduli and tensile strengths in different directions, are in the order of 1:30–1:50. The strength in tension and in compression also differ (in all directions), and the failure characteristics vary from brittle failure (tension parallel to the grain) to quasi-brittle failure (tension perpendicular to the grain and shear) to ductile failure (compression). Instead of regarding wood and timber as cheap and unsophisticated materials compared with materials that are man-made, we should indeed endeavour to meet the challenge that nature provides and develop further the methods used for testing and analysing wood and wood-based materials so as to discover new applications for wood and timber products.

### 1.2.2 Engineered Wood-based Materials

To avoid some of the disadvantages of solid wood, several engineered wood-based materials have been developed over the years. Many of these are produced using the same basic approach: cutting solid wood into smaller pieces (sheets, laminations or even fibres) and putting them together again by pressing and gluing them, sometimes at elevated temperatures, as in the case of fibreboards. Such reconstituted materials are more *homogeneous* than solid wood, and their material properties, such as stiffness and strength, do not vary as much as in solid wood. If the raw material is disintegrated into fibres or particles,

which are then randomly oriented in the end product, the result is a material that is less orthotropic than solid wood. In such reconstituted materials, the properties of the raw material have been levelled out, the lower variability attained being favourable since it results in higher design values.

### 1.2.3 Wood-adhesive Bonds

To obtain a reconstituted material that is reliable, it is of utmost importance to have reliable adhesive systems. As far as laminated products such as glulam and LVL are concerned, there are two types of adhesive bonds: those between the different laminations or sheets, and those in the lengthwise splice of continuous laminations. Lengthwise splicing involves the use of scarf joints for LVL and of finger-joints for glulam. Finger-joints are also used in the production of structural timber.

The wood-adhesives most commonly employed in structural applications today are phenol-resorcinol based adhesives (PR), (melamine) urea formaldehyde ((M)UF), polyurethanes (PUR) and epoxies (EPX). Epoxy-based adhesives are reliable and are well suited for structural purposes but are not preferred in some countries for reasons of the working-environment.

### 1.2.4 Glued-laminated Timber and Finger-joints

For approximately a century, glued laminated timber or *glulam*, has been used as a material with enhanced performance as compared with solid wood. Glulam is obtained by stacking a number of boards or laminations on top of each other to form a beam cross-section.

In order to obtain laminations of arbitrary length, the boards are finger-jointed prior to being glued together to form the cross-section desired. A commonly used adhesive in Sweden has traditionally been phenol-resorcinol (PR), for finger-jointing as well as for the gluing of laminations. During the last ten years or so, however, the use of melamine-urea-formaldehyde (MUF) adhesive has increased, since this adhesive has the advantage of being transparent, in contrast to PR adhesive, which is dark brown. After the laminations have been glued to form a particular cross-section, the beam is planed to obtain the shape desired.

The advantages of glulam as compared with solid timber are often said to be the following:

- Improved strength and stiffness, mainly because the variability of these parameters is less than in solid wood.
- Freedom in the choice of cross-sections, lengths and curvatures of the beams.
- Possibility to match the lamination qualities within the cross-section in relation to the expected stress levels (strong, high-quality laminations being placed in the outermost zones of the cross-section).
- Improved accuracy of dimensions and stability of shape during exposure to variations in moisture.

### 1.2.5 Glued-in Rods

To obtain reliable connections in timber frame corners or column foundations, large, steel-based, connectors are often used. Typically, these are dowel-type fasteners or bolted connections with large, visible steel plates mounted on the exterior of the timber member. Another method of connecting timber members which is less common, but is more appealing from an aesthetic point of view is the use of bonded-in or glued-in rods.

During the past twenty years or so, glued-in rods have been used in several countries, although mainly in Scandinavia and in Germany. At least two different principles are employed in the manufacture of glued-in rod connections. A method often used in Sweden is to drill an oversized hole into the timber (or glulam), inject the desired amount of adhesive and then insert a threaded rod. When the rod is pressed into the hole the adhesive overflow, if it occurs, indicates that the amount of adhesive was sufficient. Another method is to drill a hole of slightly smaller diameter than the nominal diameter of a threaded rod, which should also contain a lengthwise groove. A second hole is drilled perpendicular to the first and close to the bottom of the first hole. The threaded rod is then screwed into the timber, adhesive being injected under high pressure, through the second hole, until adhesive pours out at the free end of the rod. This second method does not rely completely on the adhesive bond, but is more of an ordinary mechanical joint with large screws. In the following, this second approach will not be dealt with further.

The production of glued-in rods is a relatively easy process and needs no special equipment. It should be noted, however, that in order to obtain reliable joints of high and uniform quality all gluing should be performed in a factory environment and not at a building site.

## 1.3 Organisation of the Thesis

The first part of the thesis is an introduction to the work and an overview of it. The overview can be regarded as an extended abstract of the *seven appended papers*, which form the second part of the thesis. The appended papers are presented in an order designed to make it easy to relate the results of the different studies to each other. Since this order differs from the order in which the papers were written, the references from one paper to another do not form a continuous “flow”. It is inevitable as well that some of the discussions in the different papers are overlapping. *Papers I, II* and *III* have been published previously, [16, 15, 17]. *Paper II* is an excerpt (chapters 3 and 4) from the author’s licentiate thesis concerned with an experimental study. These chapters are included here in unchanged form for the sake of completeness, since several of the other papers refer to this experimental study. A brief summary of some of the experiments is also given in *Paper III*.

# Chapter 2

## Overview of Present Study

### 2.1 Aim, Scope and Original Features

The aims of the individual studies are given in the separate papers and will not be repeated here in detail. The aim of the thesis as a whole, however, is to contribute to the field of timber engineering in terms of experimental methods, rational modelling and numerical methods for the mechanical analysis of wood-adhesive joints. The scope and original features developed to fulfil this aim are as follows:

*Paper I* reports on strength and stiffness analyses of laminated beams in bending. The methods traditionally used for such analyses are addressed. It is demonstrated, by use of simple linear elastic analysis that some of the basic assumptions commonly made in such analyses can be questioned. These assumptions relate to the stress distribution in laminated beams and to load sharing between laminations.

*Paper II* concerns testing of the mechanical properties of adhesive bondlines and finger-jointed laminations. The results of this study were later used in *Paper IV*. The bondlines are tested in order to record their strain-softening behaviour. Experiments of this type have been reported previously in [18], but the original idea here is that the bondline specimens are cut from finger-joints. This results in the wood fibres being slightly slanted and not being parallel to the bondline. An experimental study of the behaviour of finger-jointed laminations in tension under clamped conditions is also presented. Here, a new evaluation method was used for assessing the normal force and the bending moments that evolve during the testing of the clamped specimen.

*Paper III* reports on a numerical study of the mechanical behaviour of finger-joints. Such studies have been previously reported, but here the response of a complete finger-joint is simulated, instead of using assumptions regarding the boundary conditions of a small part in the interior of a finger-joint. The key issue in this paper is the influence of bondline brittleness and of defects on the strength of a finger-joint.

*Paper IV* suggests a new modelling approach to the simulation of finger-joint failure in glulam beams. It involves the use of a stochastic fictitious crack model to characterise a finger-joint. Unlike previous studies of finger-joints, this model makes it possible to study the progressive failure of a finger-joint.

*Paper V* reports the first three-dimensional finite element model of glued-in rods, a model based on nonlinear fracture mechanics. In earlier work, the writer co-authored a paper concerned with a simpler, two-dimensional analysis [10]. A three-dimensional

model makes it possible to account both for more complex geometries and for general states of stress, without having to assume axi-symmetry for example.

*Paper VI* suggests a new method for evaluating the ductility of glued-in rods. This evaluation method relates the ductility of a glued-in rod to the slope of the descending part of the recorded stress vs. deformation response. In the test series presented, which represents the first large test series ever concerned with the fracture softening of glued-in rods, several rod-adhesive combinations were tested. The effect of wood density and of load-to-grain angle on strength, stiffness and ductility was also examined.

*Paper VII*, finally, suggests a new constitutive model for wood-adhesive bondline interfaces. This model, based on damage mechanics, incorporates the effects of joint-dilatation and post-cracking friction. A modelling approach which combines the suggested interface model with a traditional elasto-plastic model of the adhesive bulk is also presented.

## 2.2 Strategy and Methods

The strategy employed can be characterised as a micro-to-macro approach in which the results at a micro level are used in the subsequent analysis at a higher level. As an example, a constitutive model for wood-adhesive bondline interfaces is suggested in *Paper VII*. This model can be used in the analysis of a finger-jointed lamination for example, such as in *Paper III*. Such an analysis results in a prediction regarding the mechanical behaviour of a finger-joint, a behaviour that can be used as an input in the glulam modelling approach adopted in *Paper IV*.

Another way of describing the strategy employed, is in terms of the methods used on different scales, where performing an experimental study provides the information needed for the theoretical models used to characterise the bondline, for example. These small-scale bondline tests are also subjected to numerical analyses, the material parameters being determined in an iterative manner. Using a set of appropriately calibrated parameters, the constitutive model is employed in numerical analyses of structural-sized joints. These analyses can then be calibrated again and be verified by tests on a larger scale. Having a calibrated model of a structural-sized joint, it is possible to conduct parameter studies of factors which influence joint strength, for example.

A brief review of the methods used in the present study in relation to certain previous work by others is provided below.

### 2.2.1 Experimental Studies

Over the years there have been a number of experimental studies of the behaviour of *finger-joints*. Examples of this are the work done by Selbo [14], Johansson [8, 9], Radovic and Rohlfing [13], Ehlbeck *et al.* [6] and Colling [5]. The experimental study presented in *Paper II* likewise concerns the behaviour of finger-joints. The test setup used was designed especially to simulate the constraints placed on a lamination when it is contained in a beam. This basic idea has also been employed in other experimental investigations [5]. A single lamination tested in pure tension without clamping, tends to bend because of knots and other anomalies. This is due to the stiffness not being constant over the cross-section of the lamination. If the same lamination was contained in a glulam beam, the rest of the beam would prevent such bending.

In both *Papers II* and *VI*, test methods for the determination of fracture mechanical properties are presented. The test methods employed and evaluation of the test results rely on the use of small-size specimens. Using a specimen of small size yields a more uniform stress distribution than using one of larger size, and also allows the strain-softening response to be monitored in a stable way. By a stable test is meant one which includes the complete descending part of the stress vs. deformation curve of the bondline, beyond peak stress. The test must be performed under displacement control in order to record the results beyond peak stress. It is also essential that the complete test setup, including load-cells, grips and the material surrounding the potential fracture area, be stiff. A stiff setup ensures that a stable fracture can take place, since the amount of elastic energy released at unloading corresponds to the amount of energy dissipated within the fracture process zone. If the setup is not sufficiently stiff, the energy surplus leads to a sudden and unstable failure. The material parameters determined here are strength, stiffness, fracture energy and shape of the stress vs. deformation curve. Fracture mechanical testing of this type has been performed previously on cementitious materials [12], and also on solid wood [4] and wood-adhesive bonds [18].

## 2.2.2 Constitutive Models and Numerical Analyses

Studies concerning numerical analysis of the mechanical behaviour of finger-joints have been reported by Aicher and co-workers [1, 2, 3], Milner and Yeoh [11] and Wernersson [18]. In [1, 2, 3] linear elastic fracture mechanics theory and plasticity theory were used, in [11] linear elastic stress analyses were performed, and in [18] a model similar to the one used here was developed and applied. However, all the studies deal with only a small part of a finger-joint using boundary conditions simulating the behaviour of a single finger in the interior of an infinitely wide lamination. Instead, in the present study, a complete finger-jointed lamination is analysed.

Several models have been proposed for analysing the behaviour of laminated beams in bending such as those of Foschi and Barrett (1980), of Ehlbeck et al. (1985) and Colling (1990) – the latter two known as the “Karlsruhe model”, and of Hernandez *et al.* (1992), Nestic *et al.* (1994), Faye *et al.* (1996) and Renaudin (1997). All these models, except those of Hernandez *et al.* and of Nestic *et al.*, involve a subdivision of the glulam member into elements, frequently standard finite elements. Loading is applied to the beam, the stresses in all the elements being evaluated. This is done at the centroid of the element, each element having the same height as the lamination. The models of Hernandez *et al.* and Nestic *et al.* use transformed section methods (based on beam theory) to calculate the stresses at mid-depth in each lamination, so as to determine the ultimate load-bearing capacity of the beam. In all of these models, the stress at the mid-depth of a lamination is used as a measure of the risk of failure.

The constitutive models employed in the thesis are of three different types. In *Paper IV*, a *fictitious crack model* having stochastic properties was used to characterise the behaviour of a finger-joint in a glulam beam. A standard, commercial finite element program was used in *Monte Carlo simulations* to obtain strength statistics for beam bending and for pure tension in a single lamination.

In *Papers I, III* and *V*, a nonlinear model based on *fracture mechanics* is used for bondline characterisation. This model is a slightly modified version of a model developed by Wernersson [18], implemented in a commercial finite element code as a *crack band*

*model*. The original model was two-dimensional involving two stress components only. In *Paper V* the model was expanded to include the three stress components acting on a plane of failure in three dimensions. The model is believed to be useful for most cases, although it has certain drawbacks. It is formulated as a nonlinear elastic model with strain softening, and, consequently, it will behave unrealistically if unloading occurs. The model also fails to take proper account of the influence of joint dilatation and frictional forces at compressive normal stresses perpendicular to the bondline. Especially in the case of glued-in threaded rods in which the failure is located in the rod-adhesive interface, the wedging action and the frictional forces can be of importance. The constitutive interface model suggested in *Paper VII* includes the features of unloading, joint dilatation and friction. This new model is formulated in terms of *damage mechanics*.

## 2.3 Results and Discussion

Some of the major results and conclusions of the present work are summarised here. For a more complete review the reader is referred to the individual papers that are appended.

### 2.3.1 Experimental Studies

In *Paper II* the main results are the measured material characteristics, such as strength, fracture energy and the shape of the stress vs. displacement curve of the adhesive bonds. Three different adhesives were tested (PR, PVAc and PUR) under three different loading conditions (shear, mixed mode and normal deformation). The adhesives differed distinctively in their behaviour in terms of strength and ductility. For example, estimates of shear strength were of approximately 19 and 9 MPa for the PR and PVAc adhesives, respectively. The corresponding fracture energies were 1250 and 2080 J/m<sup>2</sup>, respectively. Another result of the experiments performed on finger-jointed laminations, was that the test setup revealed an apparent lamination factor of approximately 1.10. Thus, if a conventional test method and evaluation method had been used, the tensile strength of the lamination would have been underestimated by approximately 10%.

The main result of *Paper VI* was the determination of strength, fracture energies and the shapes of the stress vs. deformation curves. Three different adhesives were tested: a fibre-reinforced PR (PRF), PUR and EPX. These three adhesives differed distinctively in terms of strength, ductility and the failure mode. For the EPX adhesive, various load-to-grain angles were tested. A threaded steel rod was used for all the adhesives, and a fibre-reinforced polyester (FRP) rod was also used together with EPX. Use of an FRP rod had no decisive influence on the stress vs. deformation behaviour recorded.

### 2.3.2 Constitutive Models and Numerical Analyses

A common hypothesis regarding what contributes to the so-called laminating effect in glulam beams is that weak zones with low stiffness are less exposed to high stresses since the stiffer material surrounding them acts as a “magnet” to stresses [7]. This hypothesis is addressed in *Paper I*. In this paper, it is concluded that these assumptions, for the stress distribution close to weak zones such as knots or finger-joints, are not necessarily true. For example, in that study a stiffness reduction of 25% in a 30 mm wide zone in

the outer tension lamination of a glulam beam was introduced. This stiffness reduction lowered the average tensile stress in the lamination by only 3%. Another result of this study concerns the failure modes obtained in laminated beams. It is demonstrated that *if* the outer tension lamination in a laminated beam has failed, the subsequent behaviour *can* be stable, but only for laminations with a thickness of approximately 10 mm or less.

The numerical study of finger-joint strength presented in *Paper III* highlights various interesting details. It is shown that even small defects can have a decisive influence on finger-joint strength. Since even an undamaged finger-joint contains geometrical discontinuities in terms of sharp corners, for example, the marked influence which a small defect can have is somewhat surprising. For example, introducing a glue-line void as small as 1 mm in a finger-jointed lamination, was found to reduce the strength by approximately 10%. Another finding is that the outermost finger in a finger-joint has a decisive effect on the strength of that joint. Introducing the above-mentioned small defect in the bondline of the outer finger was found to influence the strength as much as when this same defect was introduced in all the bondlines (22 of them in the present case). This has implications for comparing finger-joint tensile strength with glulam beam bending strength, since in the latter case the finger-jointed lamination is restrained, so that the outermost finger is highly reinforced.

The major finding of the study reported in *Paper IV* is that the suggested modelling approach can be useful if properly calibrated to experimental data. The modelling of the finger-joint by use of a fictitious crack model and of stochastic material data provides a more detailed modelling of a finger-joint, thus contributing to a basic understanding of the phenomenon of finger-joint failure in glulam beams.

The parameter study presented in *Paper V* results in a better understanding of the behaviour of glued-in rods. The use of a nonlinear fracture mechanics model accounts for such phenomena as the effect of glued-in length on the average shear stress at failure. The present three-dimensional FE-model also permits complex geometries and material orientations to be analysed.

The constitutive interface model in *Paper VII* allows a more realistic modelling of wood-adhesive joints. The model incorporates the effect of damaged-induced dilatation, i.e. the tendency of the joint, when under shear loading, to move perpendicular to the bondline plane. If this movement is constrained, which it is to a greater or lesser degree depending on the stiffness of the surrounding structure, compressive normal stresses will develop. The model presented accounts for this and also adds frictional stress. In *Paper VII*, a modelling approach which should be useful in the analysis of thin bondlines is outlined. The basic idea is that of using a homogenisation scheme and making use of certain assumptions regarding the stress and strain gradients across the bondline.

### 2.3.3 Future Work

The author feels that the modelling approach suggested in *Paper IV* should be further investigated, since, thus far, no calibration or verification of the model in terms of beam bending test data has been performed. Another interesting development of the modelling approach proposed would be to employ stochastic modelling for the bondlines between the laminations as well. In principle, it would also be possible to use the stochastic fictitious crack model approach to model wood failure.



The finger-joint modelling presented in *Paper III* concerned a finger-jointed lamination in tension. A further development of this modelling could be to include a full three-dimensional approach. This would make it possible to simulate the flatwise bending tests used in finger-joint production control. It would also make it possible to simulate the behaviour of a complete finger-joint in a beam which is normally exposed to a combination of tension and bending.

The constitutive model outlined for the bondline interface has not been implemented in any finite element code. Doing so should be straightforward. However, the homogenisation method for thin bondlines suggested in *Paper VII* is probably less easy to implement.

# Bibliography

- [1] Aicher, S., Klöck, W. *Spannungsberechnungen zur Optimierung von Keilzinkenprofilen für Brettschichtholz-Lamellen*. Bauen mit Holz Vol. 92(5), pp. 356–362, 1990.
- [2] Aicher, S., Klöck, W. *Finger joint analysis and optimization by elastic, nonlinear and fracture mechanics finite element computations*. Proceedings 1991 International Timber Engineering Conference, London, UK 1991.
- [3] Aicher, S. and Radovic, W., *Untersuchungen zum Einfluß der Keilzinkengeometrie auf die Zugfestigkeit keilgezinkter Brettschichtholz-Lamellen*. Holz als Roh- und Werkstoff., (57) pp. 1–11, 1999.
- [4] Boström, L. *Method for determination of the softening behaviour of wood and the applicability of a nonlinear fracture mechanics model*. PhD thesis. Report TVBM-1012. Lund University, Division of Building Materials, Lund, Sweden, 1992.
- [5] Colling, F. *Tragfähigkeit von Biegeträgern aus Brettschichtholz in Abhängigkeit von den festigkeitsrelevanten Einflußgrößen*. Berichte der Versuchsanstalt für Stahl, Holz und Steine der Universität Fridericiana, Karlsruhe, 1990.
- [6] Ehlbeck, J., Colling, F. *Die Biegefestigkeit von Brettschichtholzträgern in Abhängigkeit von den Eigenschaften der Brett lamellen*. Bauen mit Holz Vol. 89(10), pp. 646–655, 1987.
- [7] Falk, R. H., and Colling, F. *Laminating effects in glued-laminated timber beams* Journal of Structural Engineering, ASCE, 121(12), 1857–1863, 1995.
- [8] Johansson, C-J. *Strength of finger-joints for glued laminated timber*. Teknisk Rapport 1986:09. Borås Sweden, 1986. (In Swedish).
- [9] Johansson, C-J. *Strength of finger-joints for glued laminated timber. Determination of bending strength and tensile strength of finger-jointed laminations from five Swedish manufacturers*. Teknisk Rapport SP-RAPP 1983:10. Borås, Sweden, 1983. (In Swedish).
- [10] Johansson, C-J., Serrano, E., Gustafsson, P. J. and Enquist, B. *Axial strength of glued-in bolts. Calculation model based on non-linear fracture mechanics - A preliminary study*. Proceedings CIB-W18. Meeting twenty-eight. Copenhagen, Denmark, 1995.
- [11] Milner, H. R., Yeoh, E. *Finite element analysis of glued timber finger joints*. ASCE Journal of structural engineering. Vol. 117(3), pp.755–766, 1991.

- [12] Petersson, P.-E., *Crack Growth and Development of Fracture Zones in Plain Concrete and Similar Materials*. Report TVBM-1006, Lund University, Division of Building Materials, Lund, Sweden, 1981.
- [13] Radovic, B., Rohlfing, H. *Untersuchungen über die Festigkeit von Keilzinkenverbindungen mit unterschiedlichem Verschwächungsgrad*. Forschungsvorhaben I.4-34701, FMPA, Stuttgart, 1986.
- [14] Selbo, M. L. *Effect of joint geometry on tensile strength of finger joints*. Forest Products Journal Vol. 13(9), pp. 390–400, 1963.
- [15] Serrano, E., *Finger-joints for laminated beams. Experimental and numerical studies of mechanical behaviour*. Report TVSM-3021, Lund University, Division of Structural Mechanics, 1997.
- [16] Serrano, E. and Gustafsson, P. J. *Influence of bondline brittleness and defects on the strength of timber finger-joints*. International Journal of Adhesion and Adhesives. 19(1):9–17, 1999.
- [17] Serrano, E. and Larsen, H. J. *Numerical investigations of the laminating effect in laminated beams*. Journal of Structural Engineering, ASCE, 125(7) pp. 740–745, 1999.
- [18] Wernersson, H. *Fracture characterization of wood adhesive joints*. Report TVSM-1006, Lund University, Division of Structural Mechanics, 1994.

**Part II**  
**Appended Papers**



# *Paper I*



*Numerical Investigations of the  
Laminating Effect in Laminated Beams*

*by*

*Erik Serrano and Hans Jørgen Larsen*

*Journal of Structural Engineering, ASCE 125(7) 740-745*



# Numerical Investigations of the Laminating Effect in Laminated Beams

Erik Serrano<sup>1</sup> and Hans Jørgen Larsen<sup>2</sup>

*Journal of Structural Engineering, ASCE 125(7) 740-745*

## Abstract

The paper presents numerical results concerning the so-called laminating effect of laminated beams. Using the finite element method it is shown that the often made assumption of a stress redistribution taking place around weak zones is not necessarily true. A fracture mechanics approach to a possible explanation for the laminating effect is also presented. Here a nonlinear fracture mechanics model is used to verify a hand calculation formula based on linear elastic fracture mechanics. An important outcome is that for an initially cracked laminated beam, the failure mode tends to be dominated by shear failure in the outermost lamination, as the lamination thickness decreases.

**Keywords:** laminated beams, stress distribution, fracture mechanics, laminating effect

## 1 Introduction

In order to predict the behaviour of glued-laminated timber (glulam), it is essential to understand the effect of strength increase of laminations as a result of bonding them into a glulam beam, the so-called laminating effect. This effect, is often defined as a laminating factor,  $k_{lam}$ , given by (Falk and Colling (1995)):

$$k_{lam} = \frac{f_{m,beam}}{f_{t,lam}} \quad (1)$$

where  $f_{t,lam}$  is the tensile strength of the lamination and  $f_{m,beam}$  is the bending strength of the beam, evaluated using ordinary beam theory. This is a formal definition linked to the assumption that the load bearing capacity of a glulam beam is essentially governed by the tensile strength of its outer laminations. Furthermore it is assumed that the stiffness and the strength of the laminations are positively correlated i.e. a weak zone is also a zone with low stiffness.

The laminating effect has been explained by Foschi and Barrett (1980) and Larsen (1982):

---

<sup>1</sup>Division of Structural Mechanics, Lund University, P.O Box 118, SE-221 00, Lund, Sweden. Telephone: +46 46 222 95 88. Fax: +46 46 222 44 20.

<sup>2</sup>Adj. Prof. Division of Structural Mechanics, Lund University, P.O Box 118, SE-221 00, Lund, Sweden.



1. In a glulam beam, the defects are smeared out resulting in a more homogeneous material than solid wood. The probability of a defect having a serious influence on the strength of the beam is less than it is in a single lamination. This is referred to as a dispersion effect.
2. A single lamination tested in pure tension by applying a centric tensile force, may bend laterally due to knots and unsymmetrically placed anomalies. This is due to the stiffness not being constant across the cross-section of the lamination. If the same lamination was contained in a glulam beam exposed to bending, the rest of the beam would prevent such lateral bending. This is referred to as an effect of test procedure.
3. A lamination that contains knots or other zones of low stiffness will be reinforced by adjacent laminations when it is contained in a glulam beam. This is due to the fact that the stiffer and stronger laminations take up a larger part of the tensile stresses. This is referred to as a reinforcement effect.

The above three explanations are related to the beam being built up of laminations. In addition to this,  $k_{lam} \neq 1.0$  can be caused by a nonlinear stress-strain performance of the material or due to different strength in compression than in tension leading to a beam having a bending strength different from its lamination tensile strength. These reasons for  $k_{lam} \neq 1.0$  are however not related to the number and thickness of the laminations.

An effort to explain and quantify the different contributions to the laminating effect has been presented by Falk and Colling (1995). Experimental data showing such laminating factors are found in the works of Larsen (1982), and Falk et al. (1992). Larsen found that for different beam compositions the laminating factor varied from 1.06 to 1.68. The investigation of Falk et al. yielded laminating factors in the range of 1.35 to 1.65.

In the present study, emphasis is put on the third item above, and on the possibility of introducing new explanations to the laminating effect based on fracture mechanics. The study presented here is a part of a research project dealing with the mechanical behaviour of finger-joints and laminated beams presented in Serrano (1997).

## 2 Present Studies

Two types of simulations of laminated beam behaviour are presented here. The first is a linear elastic analysis of a beam subjected to a pure bending moment, using varying stiffness parameters. These analyses were carried out in order to study the influence of stiffness variation on the stress distribution in a beam. The second type of laminated beam simulations concerns the nonlinear behaviour of the bond line of the outermost lamination. These simulations were performed in order to study the possibility of predicting the laminating effect by use of a fracture mechanics approach. Both types of simulations are performed assuming plane stress conditions.

## 3 Influence of Stiffness Variation on Stress Distribution

### 3.1 Background

In analysing a beam of non-homogeneous cross-section, an assumption commonly made is that plane sections perpendicular to the beam axis remain plane and perpendicular when the beam is deformed. This assumption leads to the well-known result of a piecewise linear stress distribution over the cross-section of a glulam beam consisting of laminations differing in their modulus of elasticity. According to these assumptions, a zone of lower stiffness would be subjected to stresses of lesser magnitude, in line with the reduction in stiffness.

It is therefore often claimed that a small zone (e.g. a knot) of lower stiffness, would be subjected to stresses of smaller magnitude. Assuming a positive correlation between strength and stiffness a low stiffness implies a lower strength of the material, but in line with the discussion above of relaxation of low stiffness zones this will not have a severe effect on the global load bearing capacity of a beam.

The present analyses show that a low stiffness zone is not necessarily relaxed in the way described above.

### 3.2 Analyses

The load-case analysed is that of a glulam beam subjected to pure bending. The linear elastic analyses are performed using plane stress, 4-node, finite elements. At the boundaries where the bending moments are applied, plane sections of the beam are assumed to remain plane during loading. The beam is 315 mm in height, (7 laminations, each 45 mm thick) 600 mm in length and 100 mm in width. There is assumed to be a zone of lower stiffness in the outer tension lamination. The weak zone is 45 mm in height, its length varying from 7.5 mm to 600 mm in the different analyses. The finite element mesh used in the analyses is shown in Figure 1. In the weak zone, all the stiffness parameters are reduced by the same percentage, the surrounding material being assigned the engineering constants of  $E_x=12000$  MPa,  $E_y=400$  MPa,  $G_{xy}=600$  MPa, and  $\nu_{xy}=0.53$ . The rather high value of the Poisson's ratio was reported in Gustafsson and Enquist (1988) for pine (*pinus sylvestris*) and is also in accordance with values given by Kollmann and Côté (1968) for spruce.

Two types of analyses were performed. In the first series of analyses, the length of the weak zone was varied from the same length as the beam (600 mm) to the length of two finite elements in the fine-meshed area (7.5 mm), see Figure 1. In these cases, the stiffness parameters  $E_x$ ,  $E_y$  and  $G_{xy}$  in the weak zone were assumed to be reduced by 25%. In the second series of analyses, the influence of varying the stiffness reduction was investigated. The weak zone, 30 mm in length, was reduced in stiffness by 25, 50, 75 and 100%, respectively. In both types of analyses, the height of the weak zone was taken to be the same as the lamination thickness, i.e. 45 mm.

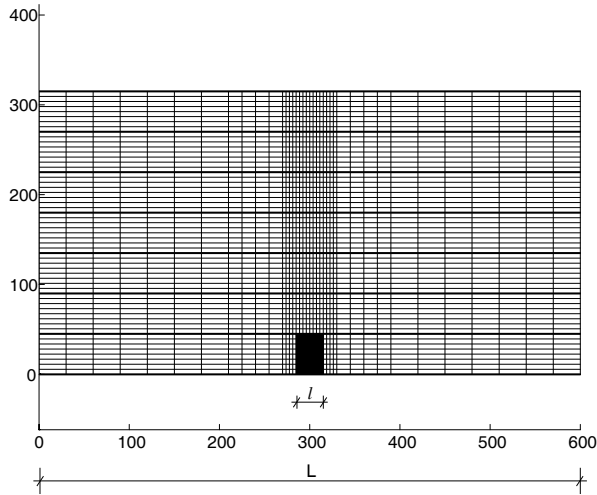


Figure 1: Finite element mesh. The dark area is the weak zone, having in the figure a length of 30 mm.

### 3.3 Results

The results of the finite element analyses are shown in Figures 2–5. The stress distributions shown in these figures all correspond to the same bending moment. The normalized stress shown is the stress divided by the maximum stress as calculated by the conventional flexure formula for a homogeneous beam. Figure 2 shows the influence of the length of the weak zone on the stress distribution in the mid-section. As expected, when the weak zone is as long as the beam, the stress distribution is indeed piecewise linear, in accordance with beam theory. A reduction in the extension of the weak zone results in a redistribution of the axial stresses. In the limiting case, as the length of the weak zone approaches zero, the stress distribution is found to approach the linear one expected in a homogeneous cross-section. According to beam theory, the length of the weak zone should not affect the stress distribution at all. Here beam theory is equivalent to the assumption of plane cross sections of a beam that initially were perpendicular to the beam axis remain plane and perpendicular to the beam axis under loading. For an orthotropic material with its material directions parallel to the beam axis and to such cross sections, the stresses will be uniaxial for pure bending. Furthermore, the stresses at a certain cross section depend only on the bending moment at this cross-section.

Figure 3 shows the stress distribution in the mid-section of the beam for a length of the weak zone of 30 mm. This figure also shows the stress distribution as predicted by beam theory. The reduction of the stresses in the weak zone is very local.

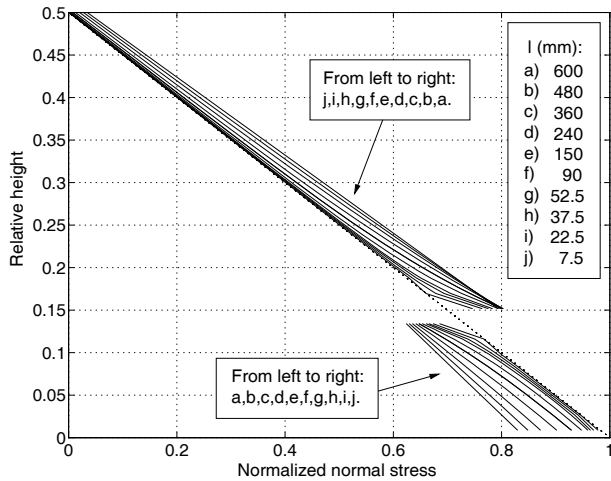


Figure 2: Influence of the length of the weak zone on the stress distribution in the mid-section in the case of a stiffness reduction of 25% in the weak zone.

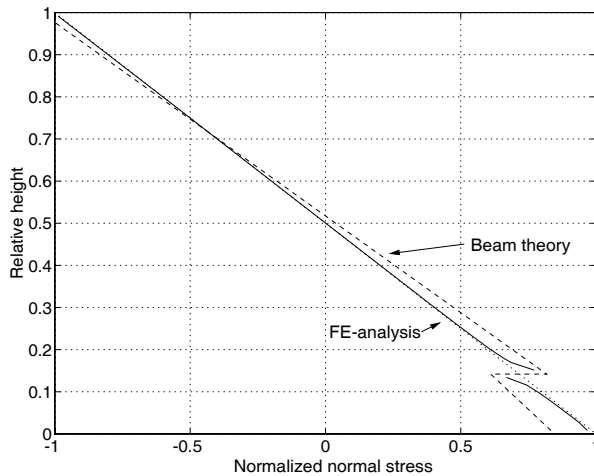


Figure 3: Stress distribution in the mid-section of the beam for a length of the weak zone of 30 mm as calculated with plane stress finite elements (solid line) and according to beam theory (dashed line). The stiffness reduction is 25%.

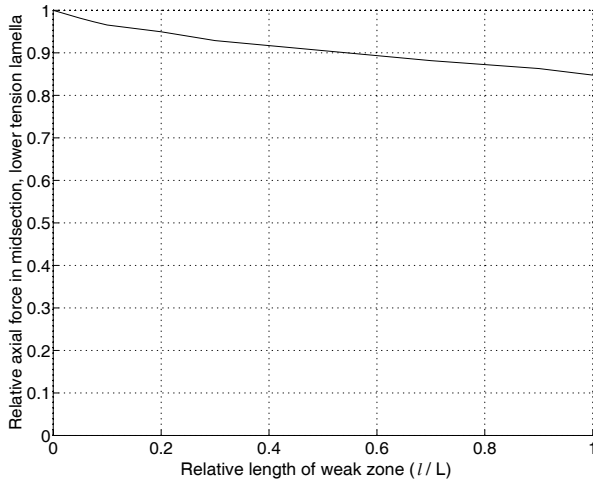
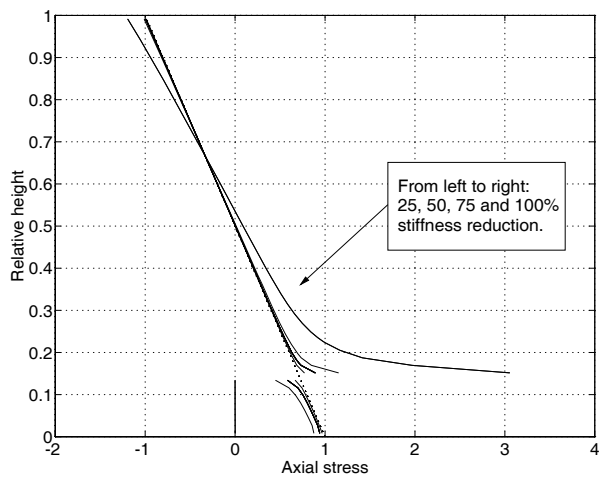


Figure 4: Influence of the length of the weak zone on the axial tensile force in the outermost lamination. The stiffness reduction is 25%.

In Figure 4 the influence on the axial tensile *force* (i.e. the mean stress in the outermost lamination) in the weak zone is shown. In the case of a weak zone 30 mm in length, the axial force is reduced by only about 3% for a stiffness reduction of 25%. According to beam theory the reduction would be 15.3%, which coincides with the FE-result obtained when the weak zone is extended all along the beam.

In Figure 5 the influence of the stiffness reduction on the stress distribution in the mid-section is shown. The four curves represent a 25, 50, 75 and 100% reduction in stiffness, respectively. As expected, for a 100% reduction in stiffness, the stresses in the weak zone are zero, since the weak zone then represents a hole or a notch.

The analyses suggest that the simple assumption that a local and proportional reduction in stiffness and strength has only minor influence on beam strength is *not* valid for small zones such as knots and finger-joints. Since the stress reduction in a small zone is far from proportional to the stiffness reduction, the stress is closer to the strength of the material in a small weak zone than one would expect by intuition.



*Figure 5: Influence of the magnitude of stiffness reduction on the stress distribution in the mid-section. The curves represent 25, 50, 75 and 100% stiffness reduction, respectively. The weak zone has a length of 30 mm.*

## 4 Laminating Effect as Predicted by Fracture Mechanics

### 4.1 General Remarks

Consider a glulam beam consisting of several layers of laminations, each having the same thickness  $\Delta h$ , Figure 6. The load case studied is that of a beam subjected to a pure bending moment. The load-bearing capacity of the beam is assumed to be governed by its behaviour on the tension side, and the material is assumed to behave linear elastically in compression. In the outer tension lamination, the beam contains a weak zone representing a knot or a finger-joint. When the weak zone has failed, the load-bearing capacity of the beam and its subsequent behaviour, may be governed by crack propagation in the direction of the beam. The grain direction is assumed to coincide with the length axis of the beam. This situation is illustrated in Figure 6

### 4.2 A Hand Calculation Formula

Based on the assumptions of *linear elastic* fracture mechanics (LEFM), Petersson (1994) derived an expression for the critical bending moment,  $M_c$ , at which a crack will propagate:

$$M_c = \sqrt{\frac{2 \cdot G_c \cdot b \cdot E_x \cdot I}{1/\alpha^3 - 1}} \quad (2)$$

where  $E_x$  denotes the modulus of elasticity in the fibre direction,  $G_c$  the fracture energy at crack propagation (the energy required to extend the crack a unit area),  $I$  the moment of inertia of the beam ( $bh^3/12$ ,  $b$  is the beam width and  $h$  its height) and  $\alpha$  the ratio  $(h - \Delta h)/h$ . To use Equation (2), the fracture energy must be known. Since the fracture energy for wood varies from approximately 200–400 J/m<sup>2</sup> for pure mode I to about three times this value for pure mode II, the current mixed mode state must be known for an accurate choice of the value of  $G_c$  to be made. However, if the mode I value of  $G_c$  is used with (2) what is obtained is a lower bound and often a fairly accurate approximation.

If a more sophisticated analysis is desired, one needs not only to calculate the current degree of mixed mode behaviour at crack propagation, but also to account for the effect of the gradual development of the fracture zone and its non-zero size. A nonlinear fracture mechanics approach such as that used in the present work allows this to be solved. To verify Equation (2), a series of finite element analyses were performed using a bond line model based on nonlinear fracture mechanics described in Wernersson (1994). In this model gradual fracture softening and mixed mode behaviour are considered.

### 4.3 A Finite Element Analysis

The case studied is that of a beam of height  $h = 450$  mm and length  $l = 1600$  mm, cf. Figure 6. The plane end-sections of the beam are assumed to remain plane during deformation and the results from the simulations are presented as formal bending stresses,  $(M/(bh^2/6))$ . To investigate the laminating effect, five different lamination thicknesses  $\Delta h$  were studied, namely 50, 25, 12.5, 6.25 and 3.125 mm. In each case the length of

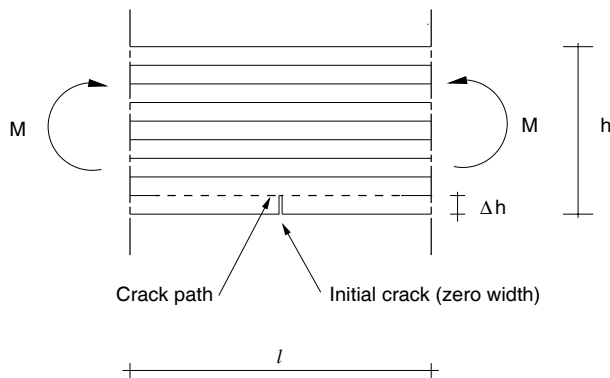


Figure 6: A laminated beam with an initial crack of a length equal to the lamination thickness. The dashed line represents the crack path at crack propagation.

the initial crack was assumed to be equal to the lamination thickness, as indicated in Figure 6.

The elements representing the bondline and located along the crack path are 0.8 mm long. The bondline data needed to define its behaviour include the strengths in pure mode I and II and the corresponding fracture energies. The values of these quantities were chosen in accordance with those reported by Wernersson (1994) i.e. 6.5 and 10 MPa strength in modes I and II, respectively, the corresponding fracture energies being 360 and 980 J/m<sup>2</sup>.

The wood was modelled as a linear elastic orthotropic material with the engineering constants of  $E_x=16800$  MPa,  $E_y=560$  MPa,  $G_{xy}=1050$  MPa, and  $\nu_{xy}=0.45$ . The engineering constants used here were chosen from Serrano (1997) and are therefore not the same as those used in the previous section. The elements representing the wood are 4-node isoparametric plane stress elements or triangular constant strain elements for mesh refining. The deformed beam at maximum load, corresponding to a bending stress of 37.9 MPa in the outermost lamination, is shown in Figure 7.

The results of the five different lamination thickness simulations are shown in Figure 8. The five simulations are represented by circles, whereas the dashed lines represent results based on Equation (2) with  $G_c = G_{Ic} = 360$  J/m<sup>2</sup> and  $G_c = G_{IIc} = 980$  J/m<sup>2</sup>. A major outcome of the simulations is that, as the lamination thickness decreases, the crack propagation is increasingly governed by mode II.

Another way of presenting the results of the finite element analyses is shown in Figure 9, displaying the strong nonlinearity. This figure presents the formal bending stress in the outer lamination as a function of the position of the tip of the fracture process zone (as measured from the symmetry line). For all the analyses, the load reached a plateau-value. Since this corresponds to the propagation of a fully developed fracture process zone, constant in shape, LEFM can be expected to provide an accurate estimate of the peak load, provided the proper mixed-mode value of  $G_c$  is employed.

Figure 10 shows the stress distribution along the bond line of the outermost lamination at peak load for the cases of  $\Delta h$  being 50, 12.5 and 3.125 mm, respectively. In the area where no damage has occurred the stress distribution is more uniform for thicker laminations. More important however is that the sizes of the fracture process



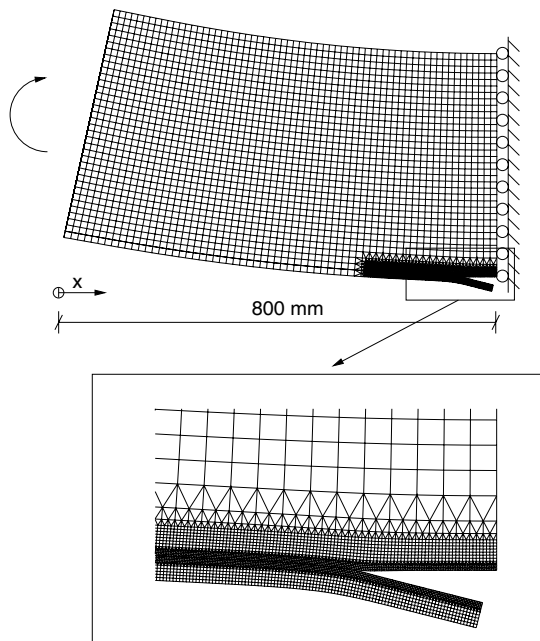


*Figure 7: The deformed beam at maximum load. The crack has extended 50–60 mm. The displacements are magnified by a factor of 30.*

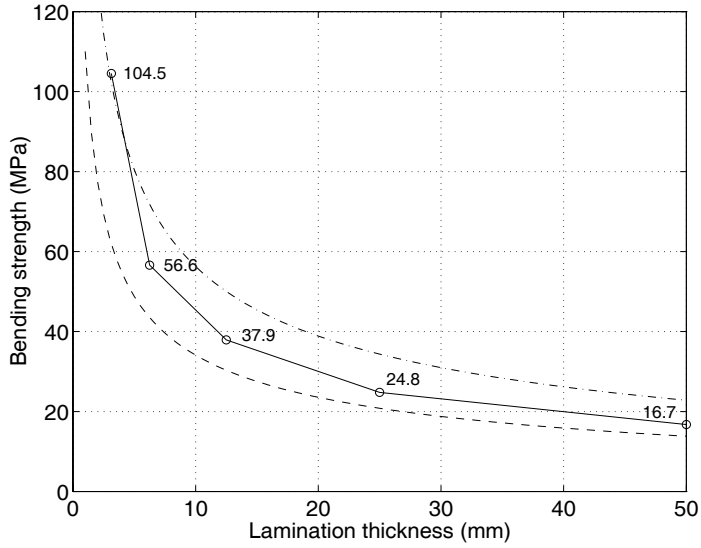


Figure 8: Formal bending strength,  $6M/(bh^2)$ , versus lamination thickness for a laminated beam 450 mm in height. The circles represent results of FE-simulations. The dashed lines represent results based on Equation (2) for  $G_c = G_{Ic}$  (dashed) and  $G_c = G_{IIc}$  (dashed-dotted).

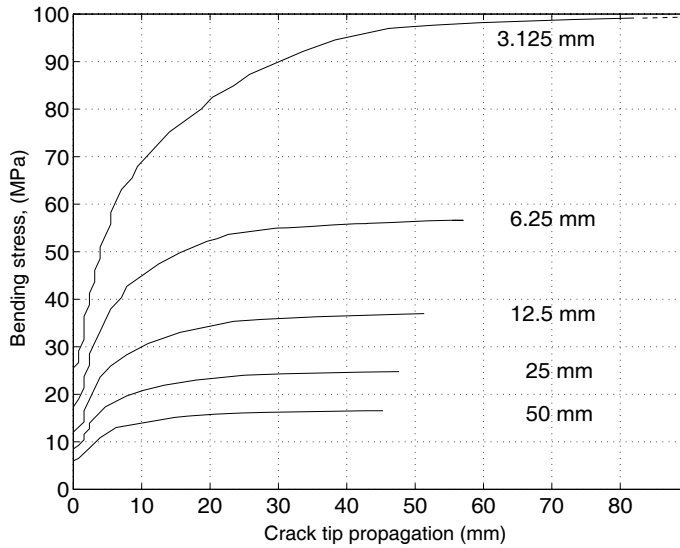


Figure 9: Formal bending stress,  $6M/(bh^2)$ , versus crack tip position for various lamination thicknesses.

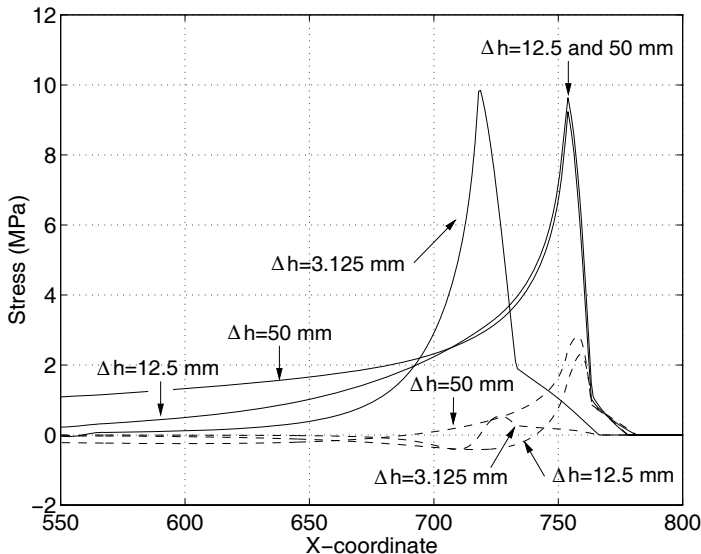


Figure 10: Stress distribution along the bond line of the outermost lamination at peak load. The solid lines correspond to shear stress and the dashed to normal stress.

zones differ for different lamination thicknesses. For a 3.125 mm lamination the fracture process zone is approximately 48 mm long, while for all the thicker laminations, it is approximately 25 mm long. This is due to the fact that for thicker laminations, the normal stress is much higher, which in turn leads to a mixed mode fracture which is associated with a lower fracture energy than the nearly pure mode II fracture taking place for thin laminations. For the 12.5 and 50 mm lamination the maximum normal stress is 2.3 and 2.8 MPa respectively, while it is only 0.5 MPa for the 3.125 mm lamination (cf. Figure 10). Since the size of the fracture process zone is associated with the fracture energy this results in a smaller fracture process zone for thicker laminations.

It turns out that the mixed mode state varies during crack propagation. The current mixed mode state is defined by:

$$\varphi = \arctan\left(\frac{\delta_s}{\delta_n}\right) \quad (3)$$

where  $\delta_s$  and  $\delta_n$  are the relative displacements between two points on either side of the bondline. Indices  $s$  and  $n$  denote shear and normal deformation respectively. A failure in pure opening mode (mode I) corresponds to  $\delta_s = 0 \Rightarrow \varphi = 0^\circ$  and a pure shear crack propagation corresponds to  $\delta_n = 0 \Rightarrow \varphi = 90^\circ$ . The curves of Figure 11 are given in terms of the mixed mode angle  $\varphi$ , as defined by (3) versus the crack tip position. The value of  $\varphi$  is calculated at the peak shear stress position. Clearly, as the lamination thickness decreases, the failure is more dominated by mode II (shearing along the lamination).

Finally, Figure 12 shows how the different contributions of mode I and mode II fracture depend on the lamination thickness. Again, it can be seen that a thin lamination yields almost pure mode II fracture.

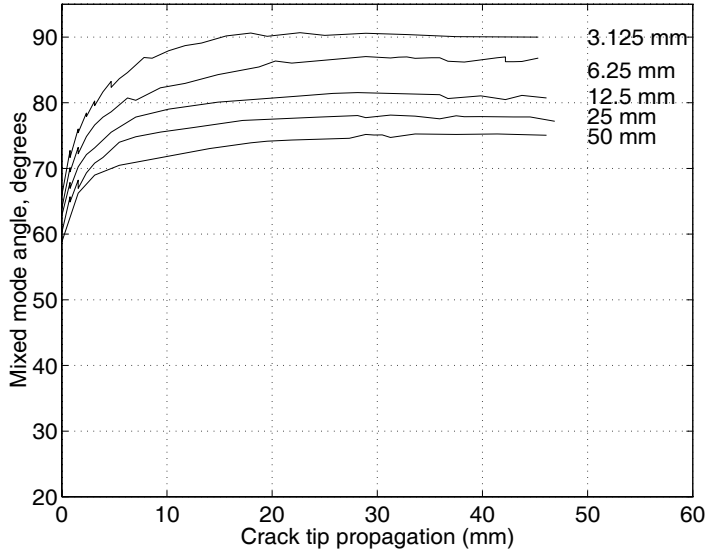


Figure 11: Mixed mode angle  $\varphi$  as defined in Equation (3) versus crack tip position for different lamination thicknesses.

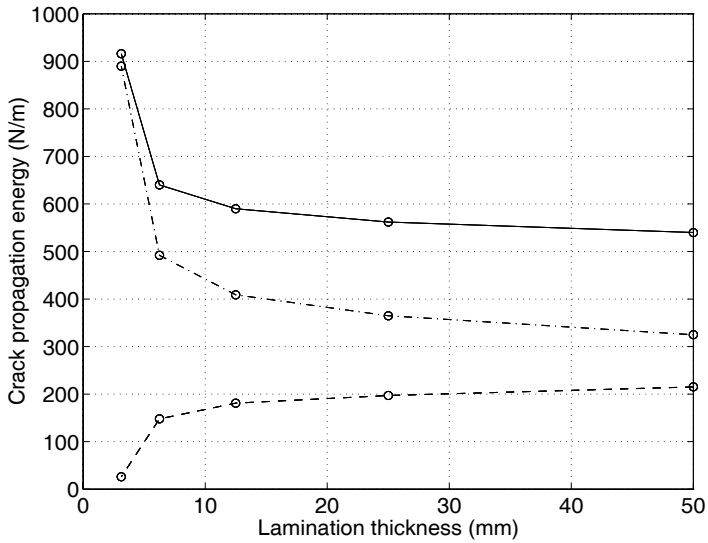


Figure 12: Energy consumption for different lamination thicknesses at the propagation of a fully developed fracture zone (solid line). The dashed lines represent the contributions of mode I (dashed) and mode II (dashed-dotted), respectively.

## 5 Conclusions

The following conclusions can be drawn from the work presented in this paper:

- For a laminated beam with a weak zone, of small dimensions in comparison to the dimensions of the beam and located in the outermost lamination, the stress redistribution around and in this weak zone is much less than predicted by conventional beam theory.
- The failure mode along the outermost bondline of an initially cracked laminated beam depends on the lamination thickness. Thinner laminations tend to lead to pure shear failure along the bondline while thicker laminations lead to failure taking place in mixed mode.

## Appendix I. References

Falk, R. H., and Colling, F. (1995). “Laminating effects in glued-laminated timber beams” *J. Struct. Engrg.*, ASCE, 121(12), 1857–1863.

Falk, R. H., Solli, K. H. and Aasheim, E. (1992) “The performance of glued laminated beams manufactured from machine stress graded norwegian spruce.” *Rep. no. 77*. Norwegian Institute of Wood Technology, Oslo, Norway.

Foschi, R. O., and Barrett, J. D. (1980). “Glued-Laminated Beam Strength: A Model.” *J. Struct. Div.*, ASCE, 106(8), 1735–1754.

Gustafsson, P. J. and Enquist, B. (1988) “Träbalks hållfasthet vid rätvinklig urtagning. [strength of wood beams with a sharp notch]” *Report TVSM-7042*, Lund Institute of Technology, Division of Structural Mechanics, Lund, Sweden (in Swedish).

Kollmann, F. F. P and Côté, W. A. (1968). “Principles of wood science and technology. Vol. 1.” Springer Verlag. Berlin. Germany.

Larsen, H. J. (1982). “Strength of glued laminated beams. Part 5.” *Report no. 8201*. Institute of Building Technology and Structural Engineering, Aalborg University, Aalborg, Denmark.

Peterson, H. (1994). “Fracture design criteria for wood in tension and shear.” *Proc., Pacific Timber Engrg. Conf.* Timber Research and Development Advisory Council, Queensland, Australia. Vol. 2, 232–239.

Serrano, E. (1997). “Finger-joints for Laminated Beams. Experimental and numerical studies of mechanical behaviour.” *Report TVSM-3021*, Lund University, Division of Structural Mechanics, Lund, Sweden.

Wernersson, H. (1994). “Fracture characterization of wood adhesive joints.” *Report TVSM-1006*, PhD thesis, Lund University, Division of Structural Mechanics, Lund, Sweden.

## Appendix II. Notation

The following symbols are used in this paper:

- $b$  = beam width;
- $E_x, E_y$  = moduli of elasticity in grain and across grain direction;
- $f_{m,beam}$  = beam bending strength;
- $f_{t,lam}$  = tensile strength of lamination;
- $G_c$  = fracture energy, critical energy release rate;
- $G_{xy}$  = shear modulus;
- $h$  = beam depth;
- $\Delta h$  = lamination thickness;
- $I$  = cross-sectional moment of inertia;
- $k_{lam}$  = laminating factor;
- $l$  = beam length;
- $M_c$  = critical bending moment;
- $\alpha$  = beam depth ratio;
- $\delta_n, \delta_s$  = relative displacements across bondline;
- $\nu$  = Poisson's ratio; and
- $\varphi$  = mixed mode angle at cracktip.



# *Paper II*

---

*Chapters 3 and 4 from*

*Finger-Joints for Laminated Beams*

*– Experimental and numerical studies  
of mechanical behaviour*

*by*

*Erik Serrano*





## 3. EXPERIMENTAL METHODS

In this chapter the experimental methods employed are presented. First certain general remarks are made concerning the most common ways of testing finger-joints, and thereafter the preparation of the samples is described. In the present test programme tests of two different types were performed. The small-specimen tests were performed to quantify the material parameters needed for modelling the adhesive bond, whereas the large-specimen tests were performed to verify the model. In the next two sections – one for each of the two types of tests, namely bond-line testing and finger-joint testing – the aims of the test programme are considered together with the methods used for evaluating the test results.

### 3.1 General remarks

#### 3.1.1 Testing of finger-joints

The most common way of evaluating the strength of finger-joints is probably through the flatwise bending of finger-jointed laminations. This method is often preferred in practice, since it is much easier to perform a bending test than a tensile test. In glulam manufacturing in Sweden, the 4-point bending test of laminations is the method most frequently employed. It is notable that the strain (or stress) distribution over the cross-section of the lamination which the most common way of testing finger-joints yields has no resemblance to the distribution found in a lamination within a glulam beam. Since in a glulam beam the beam height is much greater than the thickness of the separate laminations, the outer lamination is subjected to almost pure tension or pure compression, the strain distribution being almost uniform. In the present study, finger-jointed laminations were tested in tension.

#### 3.1.2 Testing for fracture mechanical properties

In order to obtain all the parameters needed in the bond model, stable test performance of the small specimens was called for. The parameters to be obtained are strength, fracture energy and the shapes of the stress-slip relations ( $\sigma$ - $\delta_n$  and  $\tau$ - $\delta_s$ -relation). For test performance to be stable, i.e. a test including the complete descending branch of the stress-slip relation, the test setup needs to fulfil certain requirements. When the strength of the material tested is reached, softening begins and a localized failure develops. In order for stability to be achieved, the relaxation of the material surrounding the fracture process zone must correspond to the deformation developing during cracking. Stable test performance of softening materials thus requires displacement control as well

as considerable stiffnesses outside the fracture process zone. The stiffness outside the fracture process zone includes the test specimen, its attachment to the testing machine, and the testing machine itself, including the load cells, grips, etc. Another way of expressing the stability requirement is to state that when the material softens, i.e. when the force applied by the testing machine decreases during the increase in deformation, the strain energy released outside the fracture process zone needs to be smaller than the energy required to extend the fracture zone.

## 3.2 Sample preparation

### 3.2.1 From tree to board

The wood used throughout this testing programme is spruce (*Picea abies*). The reason for its selection was that almost all the glulam manufactured in Europe today is made of spruce. The tree from which the specimens were taken was felled in southern Sweden. The tree was carefully marked, so that it would be possible to trace the original position of each of the specimens. The boards used in the manufacturing of finger-joints were taken from less than 10 m above ground level (the tree was approximately 25 m tall) in order to avoid knots insofar as possible and obtain homogeneous wood without the presence of juvenile wood. Each board was taken as far from the pith as possible to reduce the influence of the curvature of the annual rings. This simplifies the numerical simulations since it allows the wood to be treated as an orthotropic material in which the orthotropic directions within the board are constant. This in turn allows analyses to be made in two dimensions, plane stress or plane strain being assumed. The boards were approximately 3 m long and had a cross-section of  $120 \times 40 \text{ mm}^2$ . The dimensions refer to the cross-section after sawing and drying, but without planing. Figure 3.1 shows how the boards were taken from the log. In order to avoid boundary effects when the finger-joints were glued, the width of the boards was chosen so as to be much larger than the final width of the test specimens. The boards had been stored in a climate of  $20^\circ\text{C}$  and 65% RH for over a year prior to the finger-joints being milled. The moisture content of the finger-jointed laminations was 12.6% and the density of the wood at this moisture content was found to be  $526 \text{ kg/m}^3$  (mean values of 18 specimens, 2 from each lamination), the coefficients of variation being 0.02 and 0.05, respectively. The density was determined as “wet mass/wet volume”.

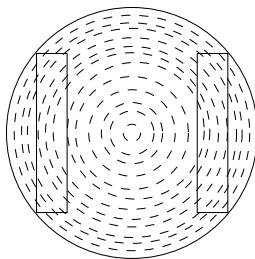


*Figure 3.1: The boards were taken from as far from the pith as possible so as to reduce the influence of the curvature of the annual rings and avoid juvenile wood.*

### 3.2.2 Finger-jointing

To produce finger-joints, each board was cut into 4 samples of approximately 0.75 m length. Each of these samples was cut into two halves, each half being given the desired finger profile (I-20) in a milling machine. The geometry of this profile is given, as shown in Figure 3.2, by the parameters  $l$ ,  $s$ ,  $p$  and  $b$ , which were 20 mm, 0.6 mm, 6.2 mm and 1.0 mm, respectively. The finger profile was visible on the *face* of the board.

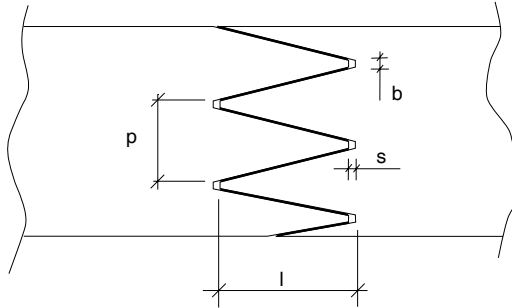


Figure 3.2: A finger-joint can be defined by 4 parameters:  $l$  is the length of the fingers,  $s$  is the gap between the tip and the root,  $p$  is the pitch and  $b$  is the width at the finger root/tip.

An adhesive commonly used in manufacturing finger-joints for glulam in Sweden is resorcinol-phenol (RP). This adhesive has the disadvantage, however, of being dark brown. Due to demands of the export market, a transparent adhesive, melamine-urea-formaldehyde (MUF), has been used the last few years. Recently, new one-component polyurethane adhesives have been developed as well. These are available in light “wood-alike” colours.

For the investigation it was decided that three different types of adhesives would be tested:

- 2-component resorcinol-phenol “RP” (Casco Nobel nr 1711+2620).
- 2-component polyurethane “PUR” (Casco Nobel nr 1899+1821).
- Polyvinylacetate “PVAc” (Casco Nobel nr 3326).

The decision to test PUR and PVAc was due to the RP-adhesive being very brittle. PVAc-adhesive is very ductile, the brittleness of the PUR-adhesive lying somewhere between that of RP and of PVAc. The three glues tested thus represent a large range in terms of brittleness.

Before the two halves of the board were glued together again, the one half was rotated  $180^\circ$  around its length axis. This made it possible to obtain an almost perfect match of the material in the vicinity of the finger-joint when the finger-jointed board, after curing, was cut lengthwise into two test samples. One sample could then be used for testing the entire lamination and the other for testing the bond line. Due to this matching procedure, the curvature of the annual rings of the two jointed board-halves do not match. In testing the laminations, however, the effect of this mismatch is small

if the curvature of the annual rings is likewise small. This mismatch of annual ring curvature is shown in Figure 3.3, but for purpose of clarity without the finger-joints.

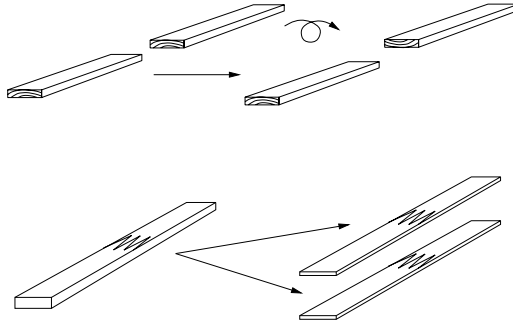


*Figure 3.3: One half of the sample was rotated 180° before being glued to the other half, so as to obtain a good match of the material in the vicinity of the finger-joint. For clarity, the finger-joints are not shown in the upper half of the figure. The finger-jointed sample is split lengthwise into two pieces after curing.*

The adhesive was applied using a piece of lumber in which the same finger profile was milled in one end. A pneumatic piston was used in glueing the samples together again. The force of the piston on the finger-jointed lamination was controlled by the air pressure. A normal force on the lamination corresponding to a mean compressive stress of about 0.5 MPa was employed. If a higher compressive stress is used, there is the risk of the wood splitting at the finger roots.

The samples were stored in a controlled climate (20°C, 65% RH) for approximately 6 months prior to the testing of the finger-jointed laminations (the bond lines were tested approximately 6–10 months after the laminations were tested). When the samples had cured, they were planed to a uniform thickness (35–40 mm) and then split lengthwise as shown in Figure 3.3.

## 3.3 Bond line testing

### 3.3.1 Purpose

The purpose of testing the bond line of the finger-joints was to quantify the bond line material parameters to be used in the numerical modelling of the joint. The parameters the model contains are the following:

- The tensile- and the shear strength of the bond line, denoted  $\sigma_{max}$  and  $\tau_{max}$ , respectively.
- The shape of the stress–displacement curves in normal- and shear-deformation loading (including the descending branch from maximum stress to complete failure).

These parameters determine the behaviour of the bond line in the model. The testing of the bond line is not pure material testing since several materials are involved: the

adhesive, the adherents and the interface between the adhesive and adherents. A model describing the behaviour of the bond line must take into account the coupling between normal (peel) stress and shear stress. If the model is assumed to correctly describe this coupling, it is only necessary to perform tests in pure mode I and in pure mode II. However, if the bond line model is to be calibrated for this coupling effect, one needs to perform several tests in mixed mode as well. The coupling effect assumed in the present numerical calculations is described in Chapter 5<sup>1</sup>.

### 3.3.2 Test setup

The test specimens were taken from boards that matched the specimens for lamination testing. This assured that the glueing of the bond line was done in the same way for the small specimens as for the large ones (complete finger-jointed laminations). One should note that the grain direction was not parallel to the bond line. For the finger profile tested the difference is about 6° (1:10.5). This may seem irrelevant at a first glance. However, since the adherents are strongly orthotropic, with a stiffness ratio of about 1:20 in the two directions in the plane of the specimen, the small grain-to-bond-line angle was of certain importance. The deviation in grain was not actually measured in the present study, the grain direction being assumed throughout the study to coincide with that of the board. The specimens used in the experiments were selected with care with regard to avoiding knots and deviations in the grain. A small deviation in the grain, say of less than 5°, is always possible, however.

The testing of the bond line behaviour was carried out in a bi-axial testing machine. The test setup is shown schematically in Figure 3.4.

The testing machine consists of two cross heads that can be controlled by stroke deformation or by force. A camera and a frame grabbing computer are also connected to the testing machine. Using the pictures taken of the specimen during the test, it is possible to measure by means of image processing the deformations that have taken place in the vicinity of the bond line. The specimen was attached to a bi-axial load cell measuring horizontal and vertical load. The test specimen had a glued area of 30 mm<sup>2</sup>. The bond line was 3 mm long in the direction considered (Figure 3.4). This short length of the bond line assures a relatively uniform stress distribution, which is crucial for simplicity in evaluating the test results. The stress distribution was verified by finite element simulations, see Chapter 5<sup>2</sup>. The specimens were attached to the testing machine by glueing them to the steel surfaces as indicated in Figure 3.4.

### 3.3.3 Methods of evaluation

The displacements and loads recorded were the relative shear and the normal displacements between the two steel parts to which the specimen was glued and the corresponding horizontal and vertical loads. This global load-displacement relation obtained was transformed to a stress–relative displacement curve for the bond line. This was done by subtracting the flexibility of the surrounding material and dividing the forces applied by the glued area, a uniform stress distribution over the bond line thus being assumed. The

---

<sup>1</sup>Chapter 5 is not included in this compilation of papers, see instead [2].

<sup>2</sup>See instead Paper III.

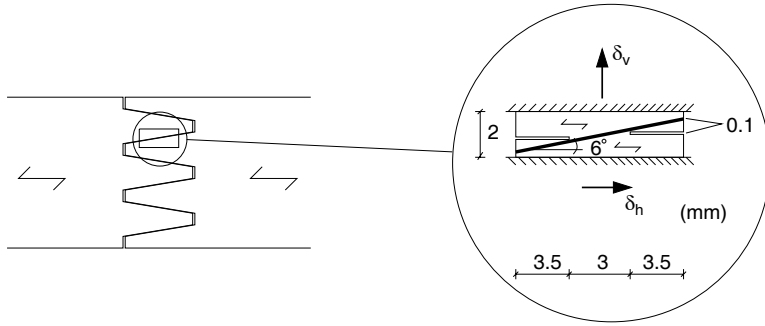


Figure 3.4: Specimen for bond line testing. The bond line direction in the specimen deviates by approximately  $6^\circ$  from the grain direction. The glued area is  $30 \text{ mm}^2$ . The specimen is  $10 \text{ mm}$  in depth.  $\delta_h$  and  $\delta_v$  indicate the horizontal and vertical relative displacements, respectively.

bond line tests were performed in a manner aimed at resembling the loading present in a finger-joint. The loading directions are thus expressed in relation to the wood fibres, rather than in relation to the bond line. The constitutive relation for the bond line, however, is expressed in terms of relative motion, parallel and perpendicular to the bond line. The stress–relative displacement curves are therefore transformed to the directions parallel to the bond line and perpendicular to it, respectively. The stress–relative displacement curves are then approximated by tri-linear relations for input in the model, see Chapter 5.

## 3.4 Finger-joint testing

### 3.4.1 Purpose

The purpose of testing the finger-jointed laminations was to verify the numerical model described in Chapter 5. Through use of three types of adhesive differing markedly in their mechanical properties, the model could be verified for a wide range of bond properties. To be able to describe the behaviour of a tension lamination in a glulam beam it is necessary to test under “beam alike” conditions. As mentioned earlier, one explanation for the laminating effect is that it is an effect of the test results evaluation, arising from the simultaneous bending of the specimen. In testing a lamination it is essential, therefore, to either assure pure centric tension of the specimen *or* measure the bending moment that would occur if uniform tensile deformation was enforced. One way of preventing the specimen from developing curvature is to use a short specimen which is clamped to the testing machine.

### 3.4.2 Test setups

Half of the finger-jointed board was used for the testing of complete finger-joints. The board was cut to a final width of  $70 \text{ mm}$  and was planed to a thickness of  $10 \text{ mm}$ . The total length of the specimens was approximately  $420 \text{ mm}$ . Specimens were equipped

with ten strain gauges each, four on each wide face side 20 mm from the finger root, and two on the edges. An LVDT-transducer measuring along a length of 150 mm was mounted on each face of the specimen. Measuring deformation using the LVDTs yielded mean values for strain over a large part of the specimen. The placing of strain gauges and transducers is shown in Figure 3.5.

In performing a test under clamped conditions, so that the conditions will resemble those of a lamination in a glulam beam, it is useful to measure the bending moments that can occur. The strain gauges mounted on the specimens provide this information. If tests are only performed under clamped conditions, a problem arises. If it is *assumed* that ordinary beam theory applies (i.e. that plane sections remain plane during deformation) and that the modulus of elasticity is constant over the cross-section it is a straightforward task to determine the bending moments. Because of variations in the modulus of elasticity, as well as knots and other anomalies, however, it is not obvious that this can be done. In order to avoid such uncertainties in evaluation of the test results, it was decided to conduct two introductory tests in the elastic region so as to calibrate the strain gauges for section forces occurring when testing to failure. A four-point bending test in flatwise bending followed by a centric tensile test without clamping or bending, was carried out. For sake of simplicity, it was decided to not perform any edgewise bending tests in the elastic region, since the test specimens were very thin in relation to their width, making it difficult to perform a four-point bending test. The two introductory tests just referred to were performed with estimated maximum stresses of approximately 7.5 and 15 MPa for the bending test and tensile test respectively. Following these tests, each specimen was tested to failure in tension under clamped conditions. The three test setups are shown schematically in Figure 3.6.

Steel plates were glued to the ends of the specimens, Figure 3.7, to prevent the wood from being crushed in the test under clamped conditions. A 10 mm hole through which a dowel was placed was drilled in each of the steel plates. The tensile test in the elastic region was performed by connecting a steel wire to the dowel placed in each end of the specimen. This assured that no bending due to eccentric loading would occur. A detail of the test specimen with the dowel, the steel plates and the steel wire is shown in Figure 3.7.

### 3.4.3 Methods of evaluation

For each of the two introductory tests performed on each specimen, the strain gauges gave constants representing strain values  $[\mu\text{str}]$  per section force  $[\text{N or Nm}]$ . Eight such constants, one for each strain gauge on the face of the specimen, were determined for each section force. The strain gauges on the edges of the specimens were not included in the evaluation, since these strain gauges were placed on the bond line of the finger-joint, yielding large deformations during the tests. The flatwise bending tests were used to calibrate the strain gauges for the flatwise bending moment, whereas the tensile tests were used to calibrate with respect to normal force *and* to edgewise bending. The calibration for edgewise bending was performed by assuming ordinary beam theory to be applicable, the strain gauge constant, determined by the tension test, being multiplied by the area of the cross-section and then divided by  $(I/c)$ , where  $I$  is the moment of inertia of the cross section for edgewise bending and  $c$  is the distance from the neutral axis to the strain gauge. From the information provided by the 8 strain gauges, it was



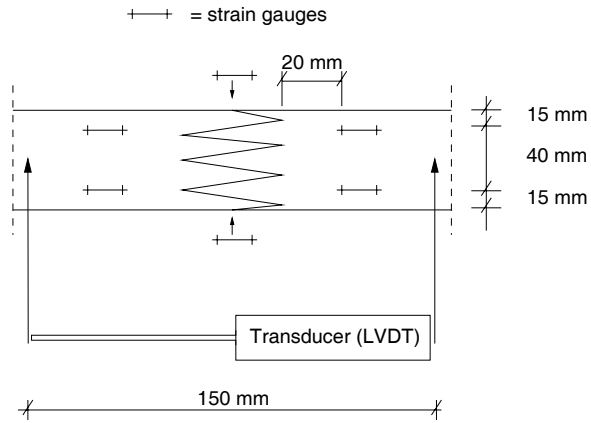


Figure 3.5: The specimens were equipped with 10 strain gauges and 2 transducers (LVDT).

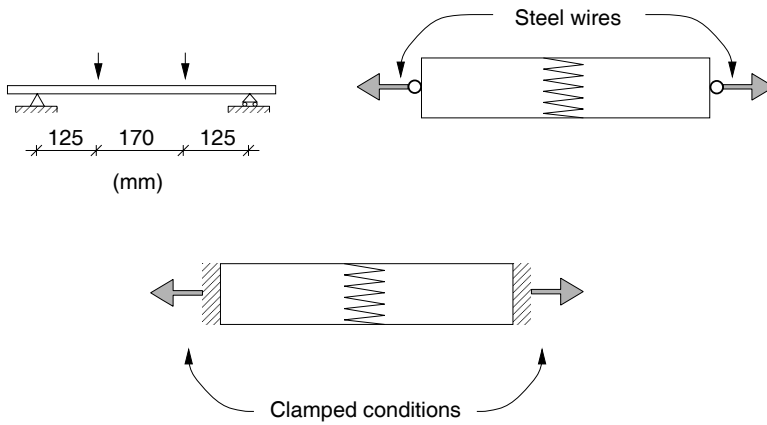


Figure 3.6: Three different tests were performed on each specimen.

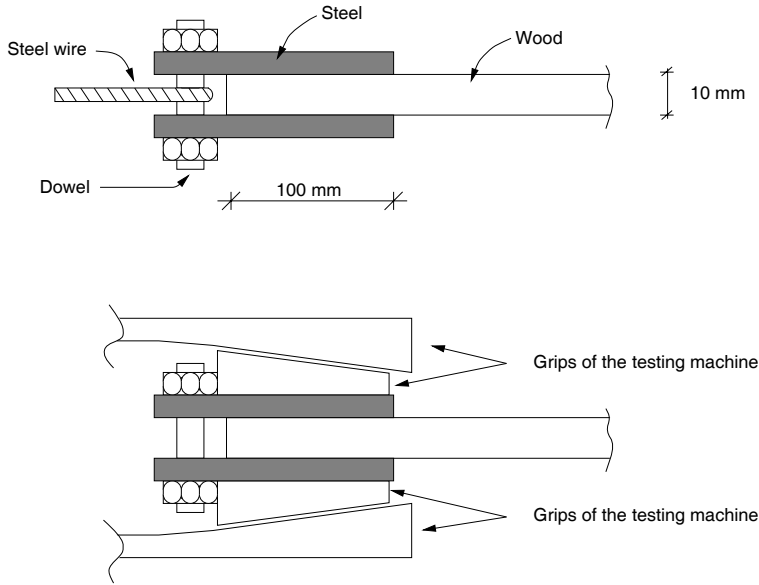


Figure 3.7: Detail of the specimen in finger-joint testing. A steel wire was attached to the dowel for the introductory pure centric tension test (upper half). The testing machine used for the tests under clamped conditions had wedge-shaped grips (lower half).

possible to determine the section forces of interest (normal force, two shear forces and two bending moments) in the way described above. The shear forces could be determined by evaluating the bending moments at two different locations on the specimen since, due to equilibrium requirements, the bending moments must be constant or vary linearly. The shear forces, or more specifically the variations in the bending moments in the specimens, were found to be very small, however. This implies the bending moments to be nearly constant. Therefore all 8 strain gauges were used to determine only one set of section forces, these representing the section forces at the mid-section of the lamination, where the finger-joint is located.

For each specimen, a set of constants can be arranged in a matrix,  $\mathbf{A}$ , of dimensions  $8 \times 3$ , each row representing the influence of the three section forces (one normal force and two bending moments) on a gauge reading, these section forces being representative for the mid-section of the lamination. Thus

$$\mathbf{A}\mathbf{q}_0 = \mathbf{e}_0 \quad (3.1)$$

where  $\mathbf{q}_0 = [N \ M_{flat} \ M_{edge}]^T$  is a  $3 \times 1$  vector containing the section forces and  $\mathbf{e}_0$  is a  $8 \times 1$  vector containing the gauge readings. Each row in this system of equations thus represents the reading for a certain strain gauge for a load case involving normal force, flatwise bending and edgewise bending, respectively.

In performing the tensile test under clamped conditions the measured gauge readings,  $\mathbf{e} = [e_1 \ e_2 \ \dots \ e_8]^T$ , are used in Equation (3.1), yielding:

$$\mathbf{A}\mathbf{q} = \mathbf{e} \quad (3.2)$$

which is an over-determined system of equations. If a trial solution  $\mathbf{q}^*$  to Equation (3.2) is introduced, the residual  $\mathbf{r}$  can be expressed as

$$\mathbf{r} = \mathbf{A}\mathbf{q}^* - \mathbf{e} \quad (3.3)$$

The solution sought should minimize the residual in some vector norm. One suitable norm is the  $L_2$ -norm of the residual, which is equal to the sum of squares of the components in  $\mathbf{r}$ , i.e.

$$\Phi = \mathbf{r}^T \mathbf{r} = (\mathbf{A}\mathbf{q}^* - \mathbf{e})^T (\mathbf{A}\mathbf{q}^* - \mathbf{e}) \quad (3.4)$$

Thus the solution sought is equivalent to minimizing  $\Phi$ , yielding

$$\frac{\partial \Phi}{\partial q_i^*} = 0, \quad i = 1, 2, 3 \quad (3.5)$$

In index notation this yields

$$\frac{\partial \Phi}{\partial q_i^*} = \frac{\partial (r_j r_j)}{\partial q_i^*} = 2r_j \frac{\partial r_j}{\partial q_i^*}, \quad j = 1, 2, 3, \dots, 8 \quad (3.6)$$

with

$$\frac{\partial r_j}{\partial q_i^*} = \frac{\partial}{\partial q_i^*} (A_{jk} q_k^* - e_j) = A_{jk} \delta_{ki} = A_{ji} \quad (3.7)$$

which is valid for constant  $\mathbf{A}$ . Making use of Equations (3.7) and (3.6) in Equation (3.5) then yields

$$(A_{jk} q_k^* - e_j) A_{ji} = 0 \quad \Leftrightarrow \quad A_{ji} A_{jk} q_k^* = A_{ji} e_j \quad (3.8)$$

In matrix form, this equation is written as

$$\mathbf{A}^T \mathbf{A} \mathbf{q}^* = \mathbf{A}^T \mathbf{e} \quad (3.9)$$

This system of equations is an ordinary one in which the number of unknown variables is the same as the number of equations. Accordingly, a possible solution is given by

$$\mathbf{q}^* = (\mathbf{A}^T \mathbf{A})^{-1} \mathbf{A}^T \mathbf{e} \quad (3.10)$$

This solution is equivalent to the least square fit of the test data to the calibrated constants of the strain gauges. The solution (Equation (3.10)) is calculated for every sample in time during the test to failure under clamped conditions. It thus gives the sectional forces as a function of time. During calibration of the strain gauges, it was assumed that the relations between sectional forces and measured strains were linear. Furthermore, it was assumed that this linear relation is independent of the section forces. It is not required, however, that the stiffness in different parts of the specimen be equal. In addition, for the evaluation of the flatwise bending and tension, it is not required that ordinary beam theory be valid.

## 4. EXPERIMENTAL RESULTS

### 4.1 Bond line tests

#### 4.1.1 General remarks

The results for the small-specimen tests are presented in this section. The tests were performed in order to obtain input data to the material model of the bond line. Therefore, the diagrams showing stress–relative displacement curves refer to the main directions relative to the bond line (i.e. parallel and perpendicular to it) since these are the directions used in the constitutive relations. The corresponding stresses are the shear stress and the normal stress in the bond line. The forces and displacements recorded during the tests were however related to the directions parallel and perpendicular to the grain. Figure 4.1 shows the definition of positive normal stress,  $\sigma$ , and positive shear stress,  $\tau$ , and the corresponding relative displacements,  $\delta_n$  and  $\delta_s$ , respectively together with the relative displacements that were recorded,  $\delta_h$  and  $\delta_v$ .

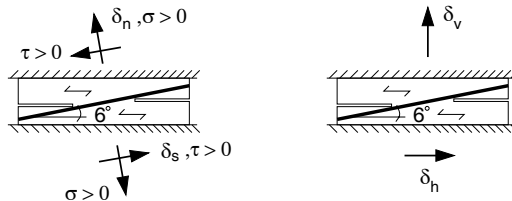


Figure 4.1: Left: Definition of positive normal stress,  $\sigma$ , and positive shear stress,  $\tau$  and corresponding relative displacements,  $\delta_n$  and  $\delta_s$ , respectively. Right: The forces and displacements recorded during testing related to the directions denoted  $\delta_h$  and  $\delta_v$ .

Three small specimens per lamination were cut out from 9 finger-jointed laminations altogether (three for every type of adhesive), matching the 9 laminations from the large specimen tests. The three small specimens originating from the same lamination were then tested in three different deformation modes. If a lamination glued with a certain type of adhesive is considered to be independent of the other two laminations bonded with the same adhesive, in total 27 *different* tests were performed (3 directions, 3 laminations/adhesive, 3 adhesives). If each adhesive is considered to belong to the same group, however, 3 repetitions were performed for three loading directions and three types of adhesive. By treating the tests as being 27 different ones, it was possible to examine whether any correlation between bond line strength/fracture energy and finger joint strength existed. Since no such correlation was found, the bond line tests were treated as being performed on three different adhesives with 3 repetitions for each.

The three loading paths used in the tests were related to the grain direction of the specimen. The displacements  $\delta_h$  and  $\delta_v$  of the bi-axial testing machine were set to be parallel to the grain, perpendicular to the grain and 2:1 to it (parallel:perpendicular), respectively. Since the bond line direction is somewhat different from the grain direction this results in slightly different paths with respect to bond line directions (approximately 9.5:1, 0.105:1 and 1.57:1  $\delta_s:\delta_n$ ). These three modes of testing are henceforth denoted as the shear-deformation test, the normal-deformation test and the mixed-mode test, respectively. In order to describe the constitutive relations of the bond lines, *uniaxial* strengths are needed. The uniaxial strengths  $\sigma_{max}$  and  $\tau_{max}$  were estimated from the test results, using an interaction formula of the type

$$\left(\frac{\sigma}{\sigma_{max}}\right)^m + \left(\frac{\tau}{\tau_{max}}\right)^m = 1 \quad (4.11)$$

where  $\sigma_{max}$  and  $\tau_{max}$  were determined using a least square fit of the test results. In Equation (4.11),  $\sigma$  and  $\tau$  denote the normal and shear strength of the bond line for the current mode of loading. The strength of the bond line is defined as the point at which either  $\sigma$  or  $\tau$  starts to decrease.

The power  $m$  was set to 2.0, 1.0 and 1.5 for the RP, PUR and PVAc adhesives, respectively. For all the small-specimen tests, the stroke rate of the testing machine was chosen to give approximately the same time to failure as for the lamination test, i.e. a few minutes. This resulted in stroke rates of 0.001–0.0002 mm/s for the different adhesives. In the tests performed, the stroke rates were constant for each type of adhesive. The stroke rates chosen for the PVAc-adhesive were determined, however, by a trial and error approach before the main series was tested. In a single test of the PVAc at a stroke rate equal to 1/10 of that adopted for the main series, the strength of the bond line was reduced by approximately 40%. Such reduction, although smaller in magnitude, accords with the results for PVAc reported in [3].

The fracture energies were calculated as the total work done during the course of loading. This work can be expressed as:

$$G_f = \int_{\Gamma} \sigma d\delta_n + \int_{\Gamma} \tau d\delta_s \quad (4.12)$$

$\Gamma$  being the deformation path leading to complete separation of the bond line. The normal stress  $\sigma$  and the shear stress  $\tau$  were calculated assuming a uniform stress distribution over the fracture area. The deformations  $\delta_n$  and  $\delta_s$  were calculated by transforming the deformations measured by LVDTs in the vicinity of the specimen to a coordinate system coinciding with the bond line directions.

#### 4.1.2 RP-adhesive

Since the resorcinol-adhesive was found to be very brittle, certain difficulties concerning the stability of the test arose. A total of 16 tests needed to be performed in order to achieve the 9 stable tests presented. The stress-displacement curves for the RP-adhesive tests are shown in Figures 4.2–4.4. For the shear-deformation test, normal tensile stresses perpendicular to the bond line developed due to the slope of bond line relative the grain orientation. It is noteworthy that after maximum shear stress had been reached in the shear-deformation tests, compressive stresses perpendicular to the bond

line developed. This can be explained by the constraint on the deformation of zero displacement in the normal direction for shear-deformation testing. It is remarkable, however, that for normal-deformation testing, maximum shear stress developed long after the maximum normal stress was reached. Although the results for the shear-deformation tests appear almost unstable, the descending part of the stress-displacement curves was in fact recorded during 10-20 seconds, using several samples ranging from maximum load to approximately 3 MPa. The strengths for the small RP-specimens, together with a quadratic ( $m = 2$  in Equation (4.11)) interaction used to estimate the uniaxial strengths, are given in Figure 4.5. The quadratic interaction yields a *uniaxial* shear strength of 19.3 MPa and a *uniaxial* normal strength of 6.5 MPa. The fracture energies for the three deformation modes tested were found to be 1250, 560 and 440 J/m<sup>2</sup> for the shear, mixed and normal deformation mode, respectively.

### 4.1.3 PUR-adhesive

The polyurethane adhesive was much more ductile than the resorcinol adhesive, and the response obtained with it showed certain tendencies of nonlinear deformations prior to peak stress. The stress-displacement curves for the three modes of loading are shown in Figures 4.6–4.8. As can be seen in Figure 4.9, for  $m = 1$ , the fit for strength was fairly good, implying the interaction to be linear. The fracture energies for the three deformation modes tested were found to be 740, 420 and 470 J/m<sup>2</sup> for the shear-, mixed- and normal-deformation modes, respectively.

### 4.1.4 PVAc-adhesive

The PVAc-adhesive was much more ductile than the RP-adhesive and there were no tendencies to instability when the tests were performed. Prior to peak stress, a tendency of a nonlinear plastic hardening deformation was evident. The stress–relative displacements obtained for the 9 tests are shown in Figures 4.10–4.12. The strength of the bond line for the three different loading combinations was fitted in terms of Equation (4.11) to an interaction in which  $m = 1.5$ , resulting in a better fit than with the quadratic interaction employed for RP-adhesive. The strengths obtained in the nine different tests, together with the fit to the interaction formula, are shown in Figure 4.13. The fracture energies for the three deformation modes that were tested, as given by Equation (4.12), were found to be 2080, 1280 and 1380 J/m<sup>2</sup> for the shear, mixed and normal deformation mode, respectively. One should note that, since the PVAc-adhesive showed considerable plastic or nonlinear behaviour prior to peak stress, the fracture energy values reported, as defined by Equation (4.12), include the pre-peak-stress work-of-fracture.

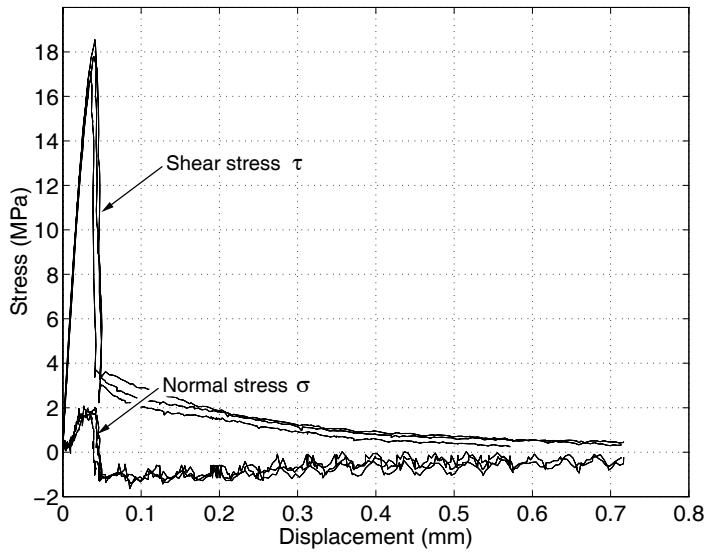


Figure 4.2: Shear and normal stress versus shear displacement  $\delta_s$  for RP-adhesive in shear-deformation testing.

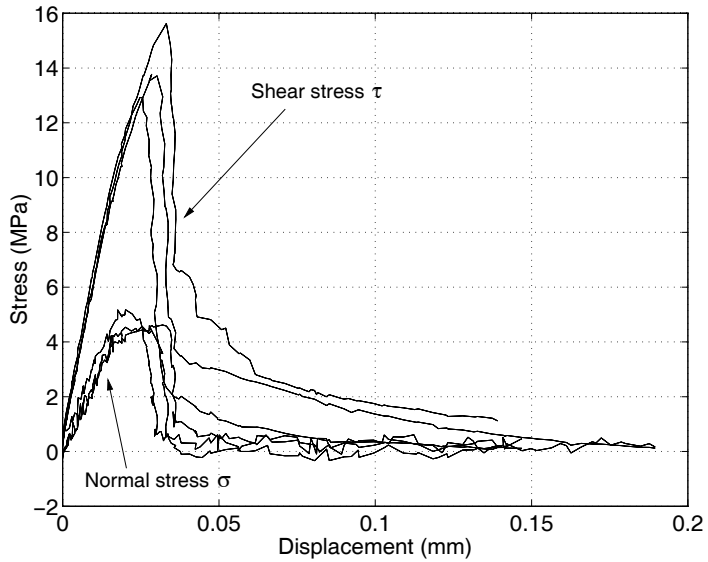


Figure 4.3: Shear and normal stress versus shear displacement  $\delta_s$  for RP-adhesive in mixed mode testing.

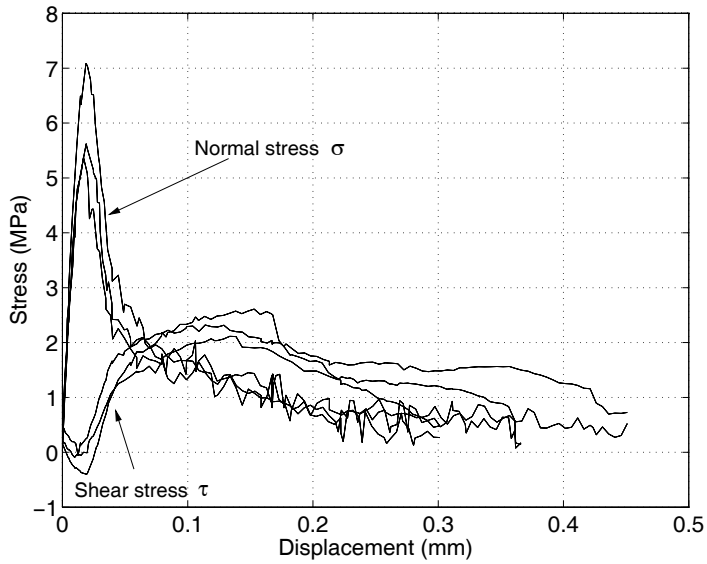


Figure 4.4: Normal and shear stress versus normal displacement  $\delta_n$  for RP-adhesive in normal-deformation testing.

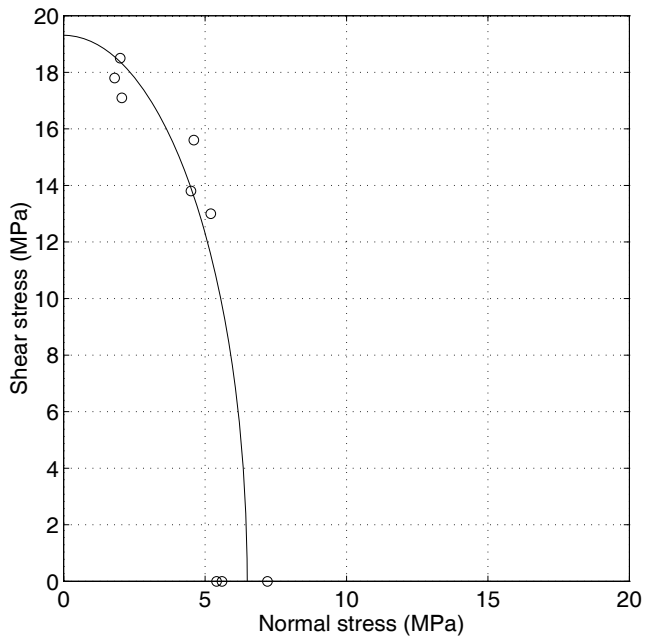


Figure 4.5: Fit of test data (circles) to a quadratic interaction formula corresponding to Equation (4.11) with  $m = 2.0$  (solid line). RP-adhesive.



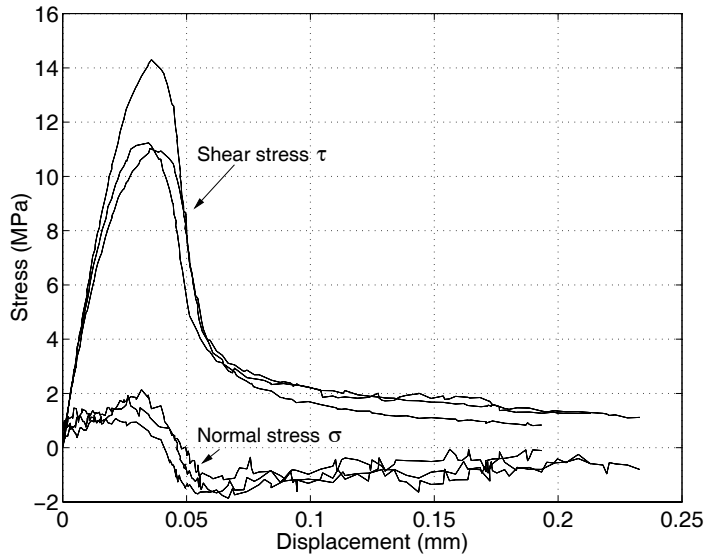


Figure 4.6: Shear and normal stress versus shear displacement  $\delta_s$  for PUR-adhesive in shear-deformation testing.

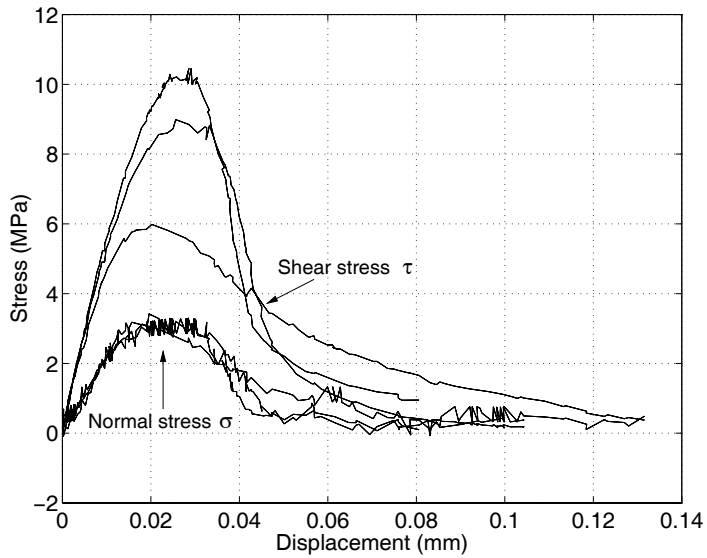


Figure 4.7: Shear and normal stress versus shear displacement  $\delta_s$  for PUR-adhesive in mixed mode testing.

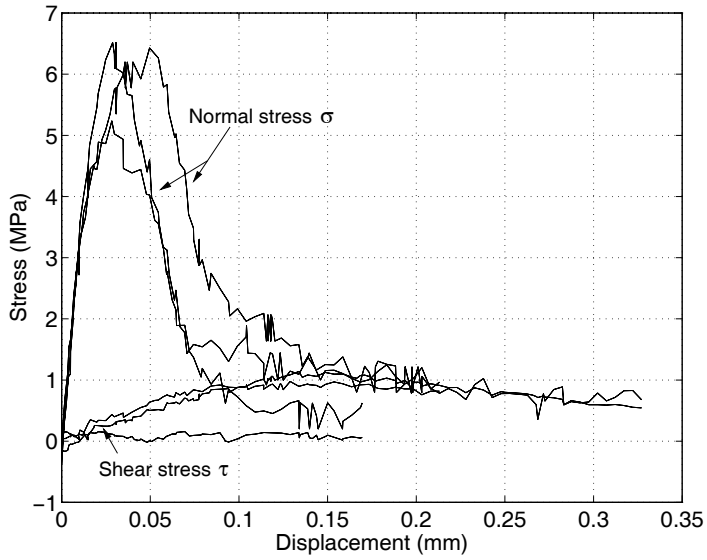


Figure 4.8: Normal and shear stress versus normal displacement  $\delta_n$  for PUR-adhesive in normal-deformation testing.

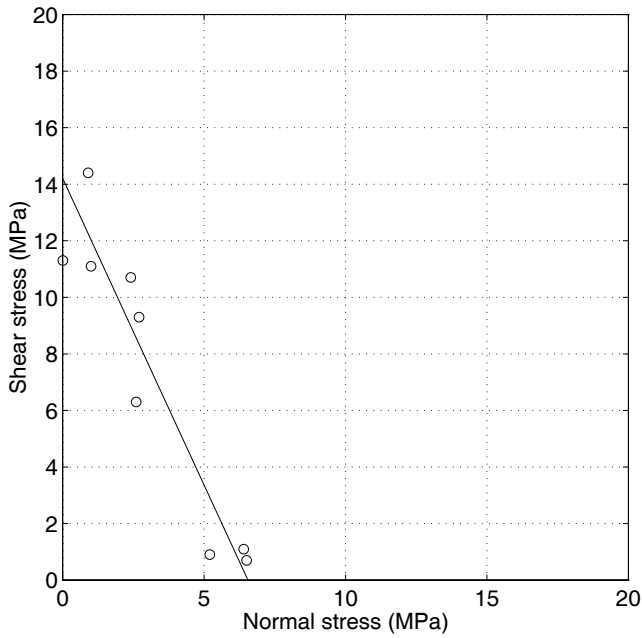


Figure 4.9: Fit of test data (circles) to a linear interaction formula corresponding to Equation (4.11) with  $m = 1.0$  (solid line). PUR-adhesive.

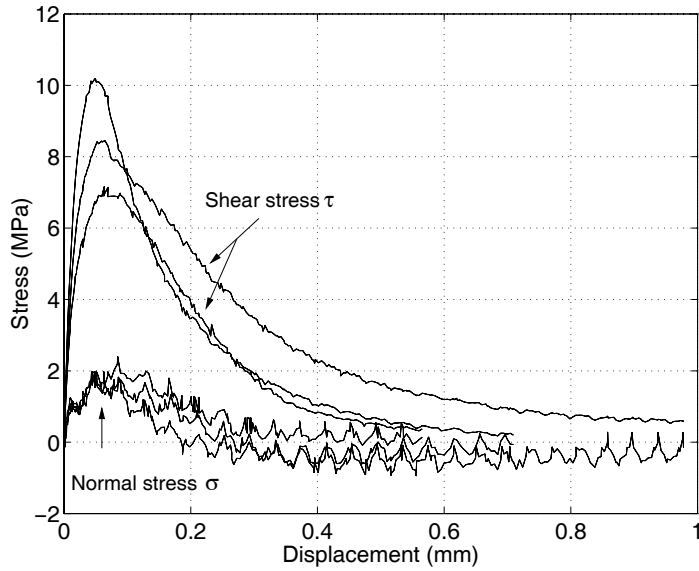


Figure 4.10: Shear and normal stress versus shear displacement  $\delta_s$  for PVAc-adhesive in shear-deformation testing.

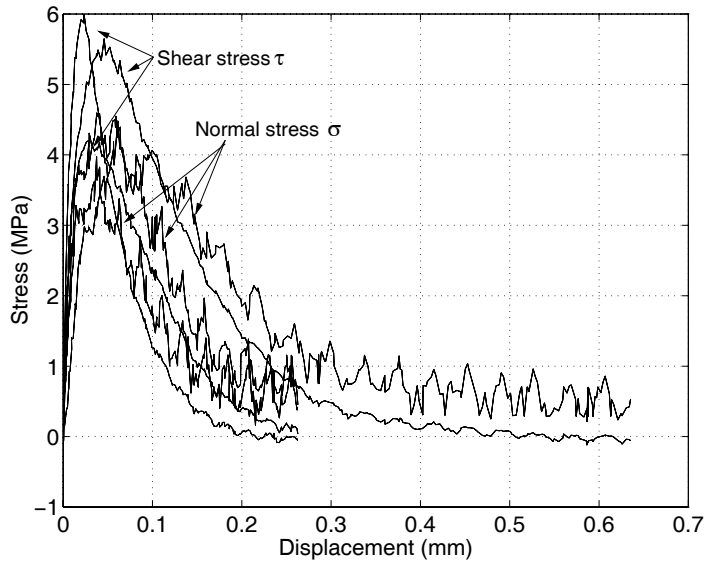


Figure 4.11: Shear and normal stress versus shear displacement  $\delta_s$  for PVAc-adhesive in mixed-mode testing.

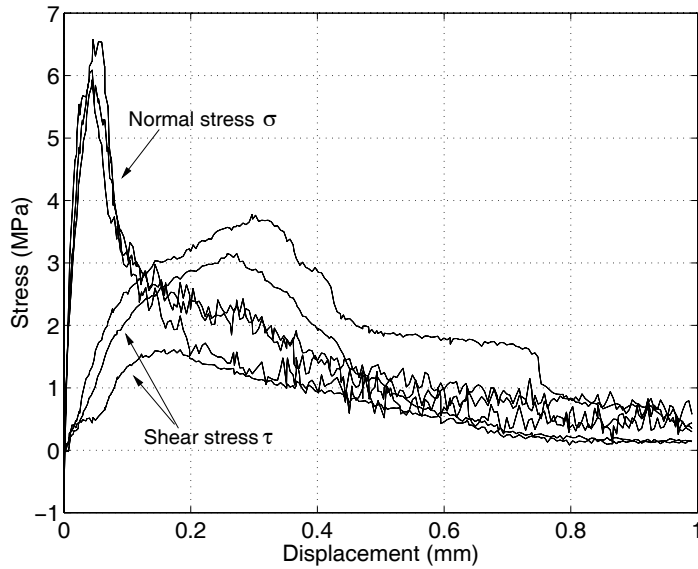


Figure 4.12: Normal and shear stress versus normal displacement  $\delta_n$  for PVAc-adhesive in normal-deformation testing.

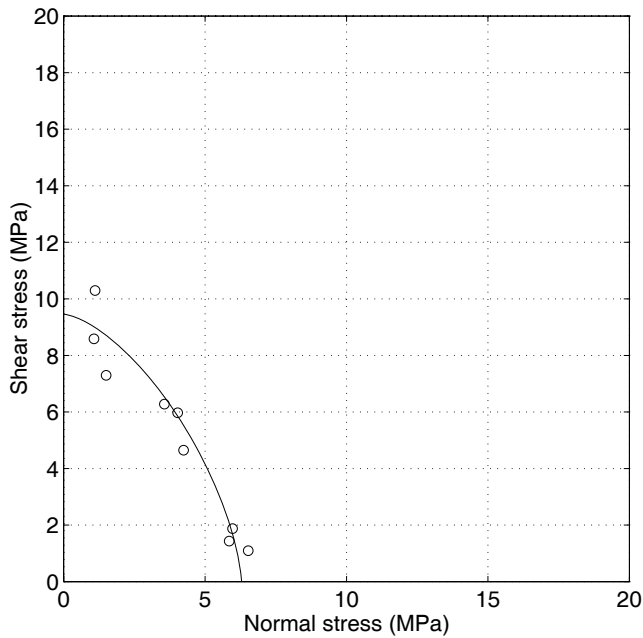


Figure 4.13: Fit of test data (circles) to interaction formula corresponding to Equation (4.11) with  $m = 1.5$  (solid line). PVAc-adhesive.

## 4.2 Tensile strength of laminations with finger-joints

### 4.2.1 General remarks

Results of testing the finger-jointed laminations are presented in the following. The tests were performed using the test setups described in Chapter 3. As indicated earlier, three types of adhesive were tested: RP, PUR and PVAc.

The results are given in diagram form as the estimated stress at certain points in the cross-section versus the measured mean stress, i.e. (measured normal force)/(cross-section area). The estimate is obtained by first evaluating the normal force and bending moments according to the method described in the previous chapter, expressing the section forces according to conventional beam theory then as stresses. It is illustrative to express the loading in terms of stresses in this way, despite this not being necessary, the use of beam theory indeed involving an approximation. The corner points of the cross-section of the specimen were chosen as the points for evaluating the stresses. According to beam theory, the maximum normal stress due to bending and to tension occurs at one of these points provided that, as assumed here, the modulus of elasticity is constant over the cross-section. The corners are enumerated from 1 to 4, see Figure 4.14.

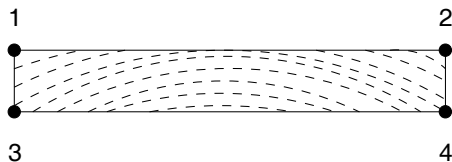


Figure 4.14: The corner points 1–4 of the cross-section.

The curves 1–4 in the diagrams correspond to these corner points. The curve without any label represents to the mean value of curves 1–4. This mean value of the estimated stresses should be the same as the measured mean stress. As can be seen in the diagrams this is also the case, indicating the method of evaluating the strains by calibrating the strain gauges for two other load cases and then combining these, being successful.

The specimens are denoted according to their original position in the log, such as:  $Gxyz$ , where  $G$  is a code for the species in question (*Picea abies*),  $x$  is the code for the level at which the log was cut from the tree,  $y$  is the code for the distance from the pith, and  $z$  is the code for the distance from the root-end within the log in question.

The modulus of elasticity can be evaluated in a number of ways, on the basis of the introductory bending and tensile tests using either strain gauge or transducer readings, or on the basis of the test to failure under clamped conditions. In the following, the moduli of elasticity of the specimens as measured by the strain gauges during the flatwise bending tests are given. In Appendix A, a more comprehensive compilation of the measured moduli of elasticity, including the moduli of elasticity for separate halves of the specimens is provided.

Besides using measurement of strain, the modulus of elasticity can be estimated in an approximate manner on the basis of density using a regression formula. One such formula is that given by Johansson in [1]:

$$E = \rho^{1.577} \quad (4.13)$$

where the density  $\rho$  is the oven-dry density (dry weight/volume at 12% moisture content,  $\text{kg/m}^3$ ) of the material and  $E$  is the modulus of elasticity in MPa. According to Johansson, [1], this regression formula yields a good fit for Swedish spruce (*Picea abies*). The densities measured for the different specimens are listed in Appendix A.

#### 4.2.2 RP-glued finger-joints

The three laminations glued using resorcinol-phenol all failed completely along the fingers. The failure was mainly in the wood in the vicinity of the bond line, there being a large amount of wood fibres at the fracture surfaces. The measured strengths (normal force/area) were 46.8, 56.3 and 50.3 MPa for specimens G15a, G15b and G15c, respectively. The moduli of elasticity for the specimens were calculated on the basis of the introductory flatwise bending tests, yielding stiffnesses of 16500, 16500 and 17700 MPa, respectively, for the three specimens. Figure 4.15 shows specimen G15a after failure. The results of the tests to failure are shown in Figures 4.16–4.18.

#### 4.2.3 PUR-glued finger-joints

Two of the three laminations glued with polyurethane failed completely along the fingers. The failure in these cases was mainly in the wood in the vicinity of the bond line, there being a large amount of wood fibres at the fracture surfaces. The third specimen, G33c, failed along 9 of 11 fingers and along a crack from the fingers to the support. This specimen is shown in Figure 4.19. The measured strengths (normal force/area) were 40.0, 41.6 and 44.7 MPa for specimens G33a, G33b and G33c, respectively. The corresponding moduli of elasticity of the specimens were calculated on the basis of the introductory flatwise bending tests, yielding stiffnesses of 16600, 17200 and 18000 MPa, respectively, for the three specimens. The results of the tests to failure are shown in Figures 4.20–4.22.

#### 4.2.4 PVAc-glued finger-joints

Two of the three specimens of finger-joints glued with PVAc failed completely along the bond line of the fingers (G13c and G13d) while the third specimen (G14a) failed partially along the fingers and partially in the solid wood. Figure 4.23 shows the partial finger failure of the specimen denoted as G14a. The measured strengths (normal force/area) were 32.0, 33.6 and 35.0 MPa for specimens G13c, G13d and G14a, respectively. The corresponding moduli of elasticity were calculated on the basis of the introductory flatwise bending tests, yielding stiffnesses of 17600, 17700 and 13600 MPa, respectively, for the three specimens. It is notable that the specimen G14a, taken from a different position in the log, showed considerably less stiffness. As mentioned above, the failure of this specimen also differed from that of the other two specimens. The results of the tests to failure are shown in Figures 4.24–4.26.

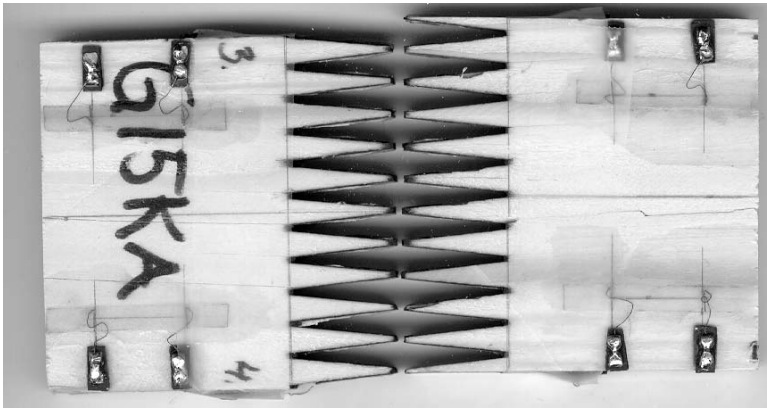


Figure 4.15: Failure of specimen G15a, RP-adhesive.

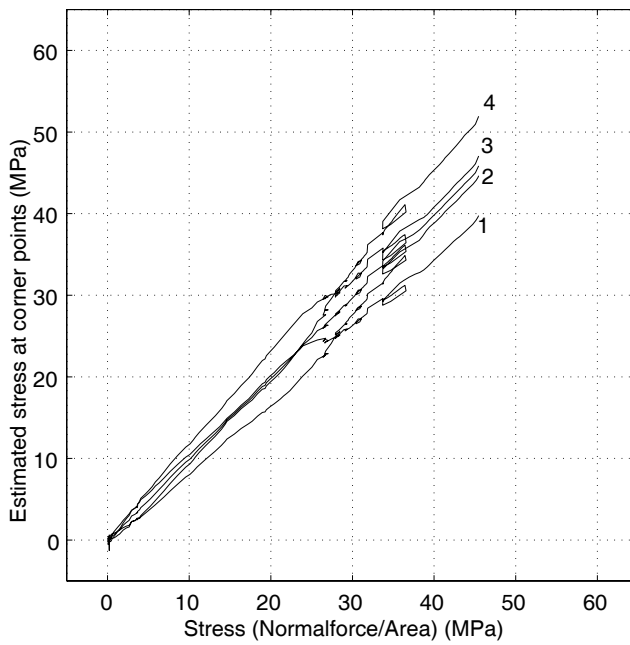


Figure 4.16: Results for sample G15a, RP-adhesive.

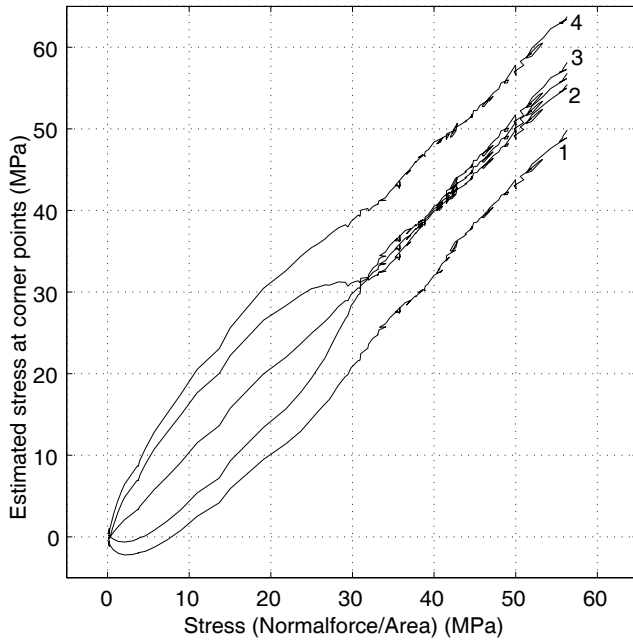


Figure 4.17: Results for sample G15b, RP-adhesive.

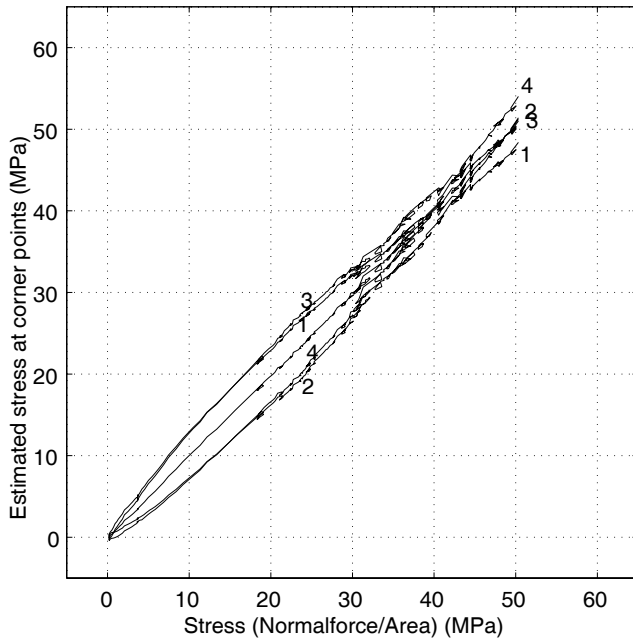


Figure 4.18: Results for sample G15c, RP-adhesive.



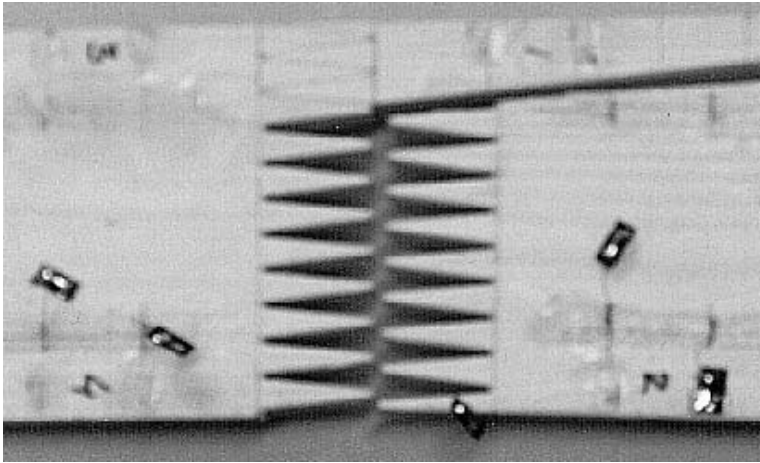


Figure 4.19: Failure of specimen G33c, PUR-adhesive.

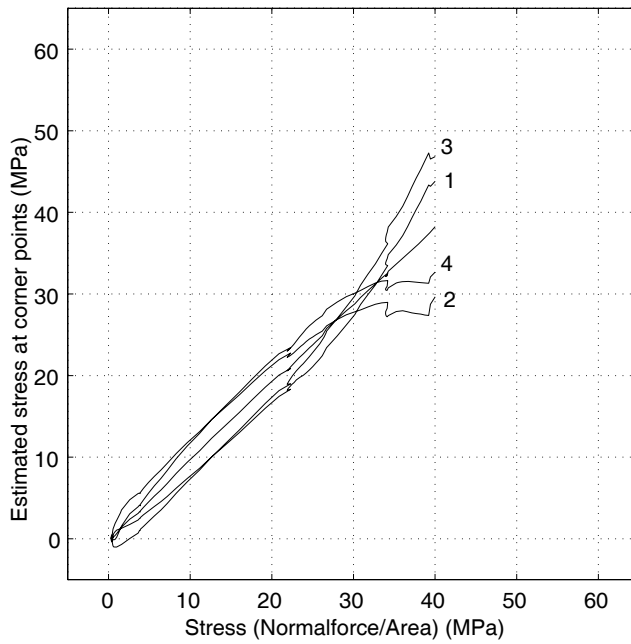


Figure 4.20: Results for sample G33a, PUR-adhesive.

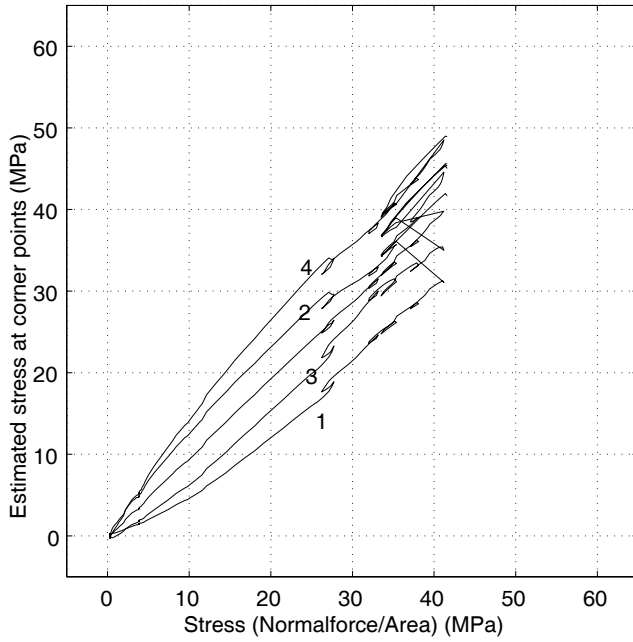


Figure 4.21: Results for sample G33b, PUR-adhesive.

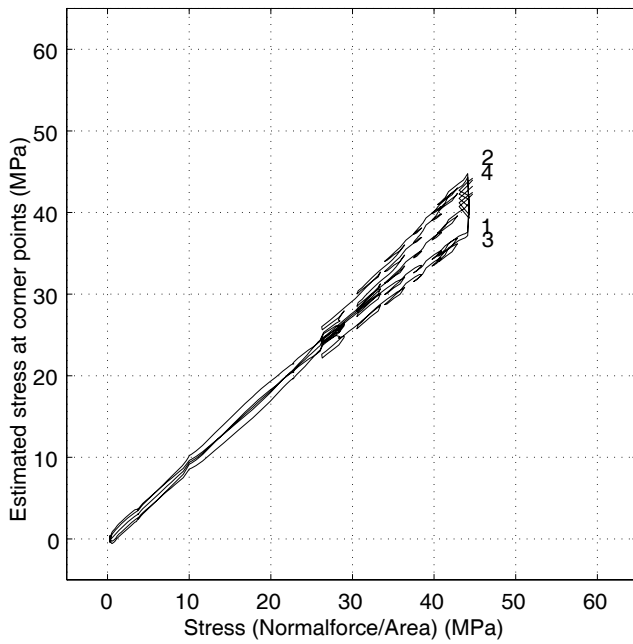


Figure 4.22: Results for sample G33c, PUR-adhesive.

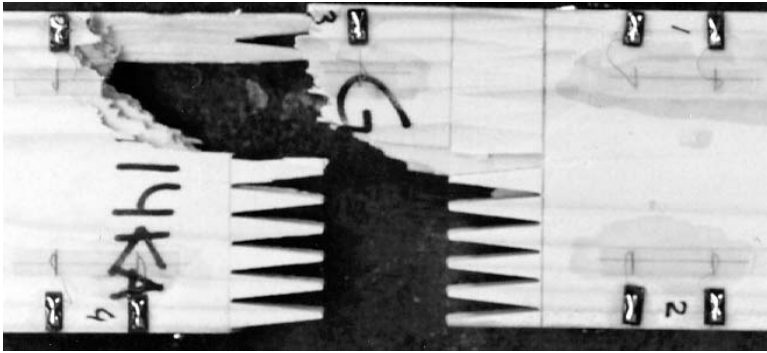


Figure 4.23: Failure of specimen G14a. PVAc-adhesive.

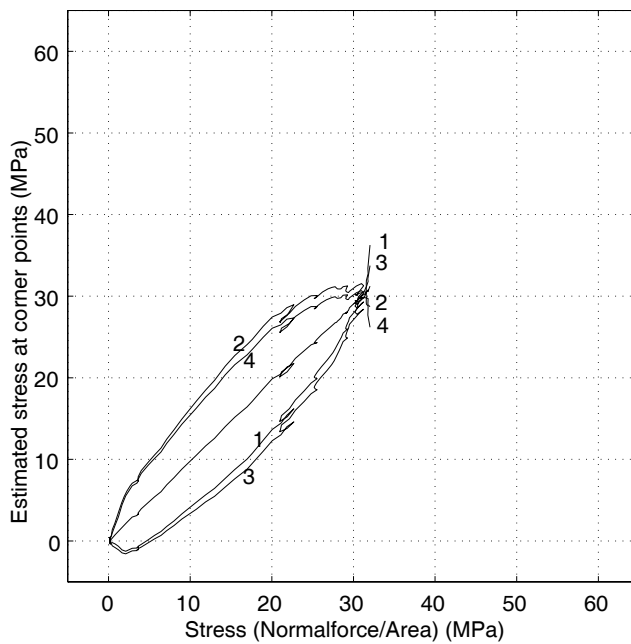


Figure 4.24: Results for sample G13c, PVAc-adhesive.

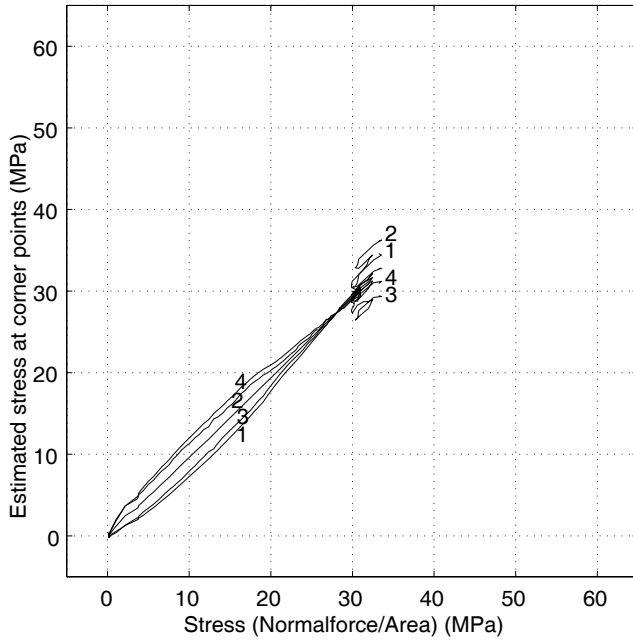


Figure 4.25: Results for sample G13d, PVAc-adhesive.

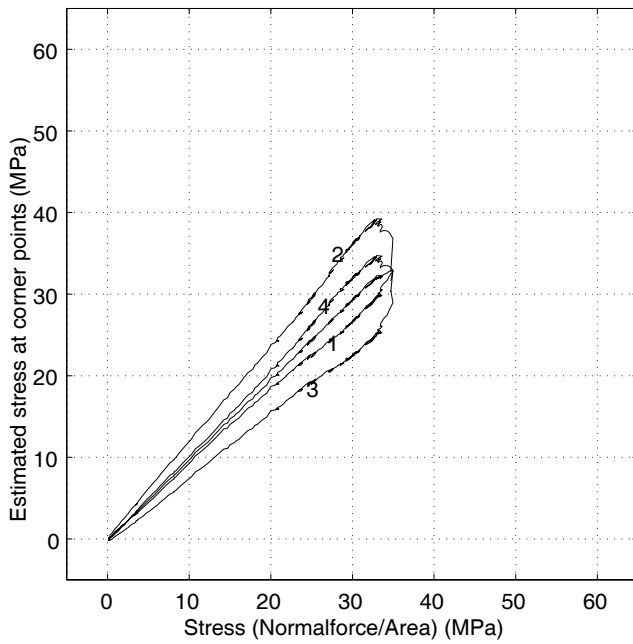


Figure 4.26: Results for sample G14a, PVAc-adhesive.

### 4.3 Compilation of test results

A summary of the test results, indicating the strengths and fracture energies of the adhesives as obtained in the small-specimen tests, together with the measured and estimated strengths of the finger-jointed laminations is presented in Table 4.1. The uniaxial strengths of the bond lines are estimated using the interaction formula in Equation (4.11). This equation is also shown as a solid line in Figures 4.5, 4.9 and 4.13, respectively.

The specimens used in finger-joint testing were selected with great care and were subjected to thorough documentation in terms of strain measurement during the testing. Three different types of adhesive were used so that distinct differences in mechanical behaviour would be present. The test results showed very little scatter, each type of adhesive yielding strengths of the finger-joints within a distinct (unique) interval. From the introductory bending tests performed on each of the large specimens, the mean value of the longitudinal modulus of elasticity as estimated from strain gauge measurements was found to be 16800 MPa. The density of the wood, in turn, was found to be 526 kg/m<sup>3</sup> at 12.6% moisture content, as reported in the previous chapter. This corresponds to an oven dry density of approximately (“dry mass/wet volume”) 467 kg/m<sup>3</sup>, corresponding to a modulus of elasticity of  $E = 467^{1.577} = 16200$  MPa in terms of Equation (4.13). This deviates by about 4% from the mean value as estimated from the strain gauge measurements.

Table 4.1: Uniaxial strengths of the bond lines ( $\tau_{max}$  and  $\sigma_{max}$ ) according to Equation (4.11). The fracture energies ( $G_{f,I,II,mixed}$ ) are evaluated using Equation (4.12). For the finger-joint strengths ( $f_t$ ), the index *est.* refers to estimated maximum stress according to beam theory. The moduli of elasticity,  $E$ , are based on the strain gauge measurements made during the flatwise bending tests (mean of three specimens). Units are MPa and J/m<sup>2</sup>.

	RP-adhesive	PUR-adhesive	PVAc adhesive
$\tau_{max}$	19.3	14.2	9.46
$\sigma_{max}$	6.50	6.55	6.29
$G_{f,I}$	440	470	1380
$G_{f,II}$	1250	740	2080
$G_{f,mixed}$	560	420	1280
$f_t$	51.2	42.1	33.5
$f_{t,est.}$	56.6	46.7	37.2
$E$	16900	17200	16300

An important outcome of the tests performed is visualized in Figure 4.27. The figure shows the finger-joint strength in relation to the shear strength of the bond line. In addition to the individual strength of the 9 laminations tested, the mean value for

each type of adhesive is also indicated (+). The dashed curve represents a least square fit of the mean values to an expression of the type  $y = kx^\alpha$ .

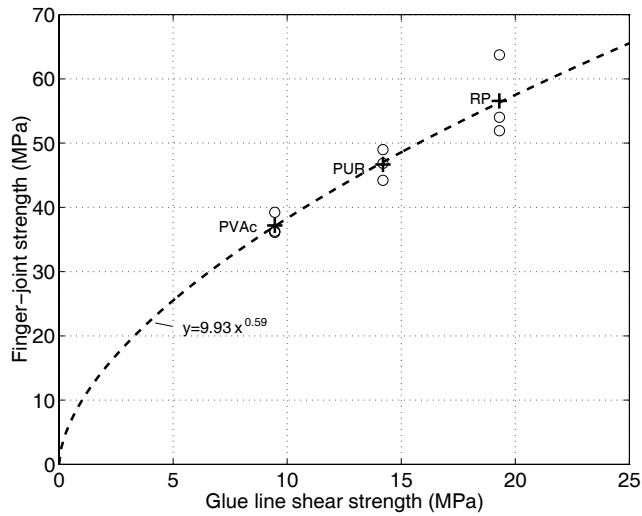


Figure 4.27: Finger-joint strength versus shear strength of adhesive. The mean value for each adhesive is indicated by '+'. The dashed line is a least square fit of  $y = kx^\alpha$  to the mean values.

To clarify the differences in material response, “hand-drawn” mean curves of the stress-displacement relations for the shear-deformation and normal-deformation tests are shown in Figures 4.28 and 4.29.

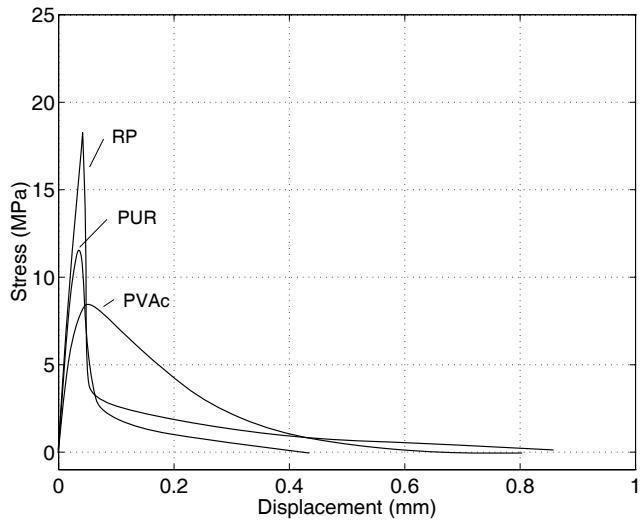


Figure 4.28: Shear stress versus shear displacement. Mean curves for different adhesives in shear deformation testing.

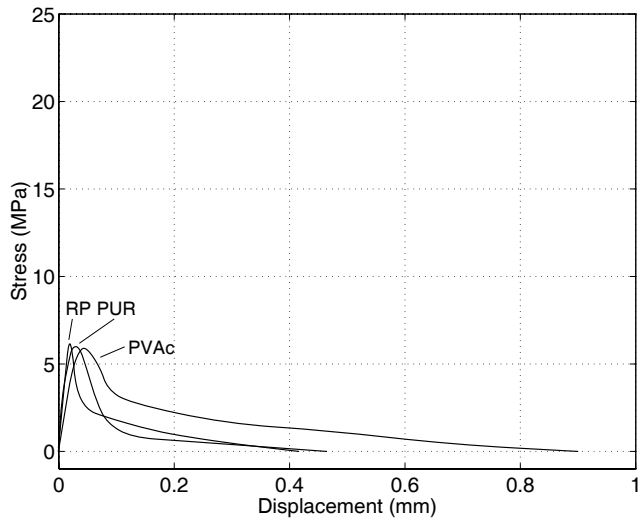


Figure 4.29: Normal stress versus normal displacement. Mean curves for different adhesives in normal deformation testing.

# References

- [1] Johansson, C-J. *Strength and stiffness of glulam with lamellas of machine stress graded timber*. SP RAPPORT 1990:22. Statens provningsanstalt. Borås 1990. (In Swedish).
- [2] Serrano, E., *Finger-joints for laminated beams. Experimental and numerical studies of mechanical behaviour*. Report TVSM-3021, Lund University, Division of Structural Mechanics 1997.
- [3] Wernersson, H. *Fracture characterization of wood adhesive joints*. Report TVSM-1006, Lund University, Division of Structural Mechanics 1994.





## *Paper III*

---

*Influence of Bondline Brittleness and Defects on the  
Strength of Timber Finger-joints*

*by*

*Erik Serrano and Per Johan Gustafsson*

*International Journal of Adhesion and Adhesives 19(1) 9–17, 1999*



# Influence of Bondline Brittleness and Defects on the Strength of Timber Finger-joints

Erik Serrano and Per Johan Gustafsson

*International Journal of Adhesion and Adhesives 19(1) 9–17, 1999*

## Abstract

Numerical finite element results on the mechanical behaviour of finger-joints for laminated timber products are presented. Simulations are based on a non-linear fracture mechanics description of the bondlines in the finger-joints. It is shown that, for a commonly used resorcinol-phenol adhesive, there is potential of increasing substantially the finger-joint strength by increasing the fracture energy of the bond. However, even a single, small glue-line void can have a considerable influence on reducing the joint strength.

**Keywords:** wood, fracture mechanics, finite element analysis, finger-joint

## 1 Introduction

### 1.1 Purpose

The present study is a part of a research project dealing with the mechanical behaviour of wooden finger-joints and laminated wood products such as glued-laminated timber (glulam). The finger-joints are often the weak links in glulam: a summary of 1767 beam bending tests by Colling [1] showed that 220 out of 277 beams having finger-joints in the zone with maximum bending moment showed failure modes related to the finger-joints. The purpose of the presented work is to obtain knowledge about the mechanical behaviour of finger-joints and especially their sensitivity in strength to material properties of the bondline and the wood and to defects in the bondline.

### 1.2 Strategy

The strategy of the present study was to use the experimental and computational methods for the analysis of wood adhesive joints inherent in the work of Wernersson [2], based on nonlinear fracture mechanics theory. The study involved fracture mechanics tests of bondlines cut from finger-joints, providing the necessary information for quantification of parameters in the bondline material model. This model was implemented in a finite element (FE) computer code. An FE-model of a finger-jointed lamination was then developed and used to perform parameter studies of various factors affecting the load-bearing capacity of a finger-jointed lamination. In this paper emphasis is placed on the numerical sensitivity analysis. A few of the test results are, however, reported for the purpose of illustration. For full details on the study the reader should consult the

thesis by the first author [3]. Numerical simulations on finger-joints have been reported by e.g. Aicher & Klöck [4] and Wernersson [2]. In both cases symmetry was assumed in order to simplify the calculations, making it possible to analyse only a single finger in the middle of an infinitely wide lamination. In the present study numerical results from simulating a complete finger-jointed lamination are presented.

## 2 Experimental Methods

### 2.1 Sample Preparation

The wood used throughout the testing programme is spruce (*Picea abies*). Each of the boards used to produce test samples was cut into two halves, each being given the desired finger profile (I-20) in a milling machine. This finger profile has a length of 20 mm, a finger-tip gap of 0.6 mm, a pitch of 6.2 mm and a finger-tip width of 1.0 mm. The finger profile was visible on the wide face of the board. Before the two halves of the sample were joined together again, one section was rotated 180° about its length axis, as shown in the top of Figure 1. This ensures a good matching of the material in the vicinity of the finger-joint when the sample, after curing, is split lengthwise in two. Of these two halves, one can be used for testing the entire finger-joint, while the other can be used to cut out small specimens to test the bondline. A schematic of how the specimens were cut out from the finger-joint and the finger-joint dimensions are shown in Figure 2. The adhesive used was a 2-component resorcinol-phenol (RP) adhesive, the most commonly used timber adhesive in Sweden for structural purposes.

The boards had been stored in standard climate 20°C, 65% RH, for more than six months prior to the sample preparation. The moisture content of the specimens was found to be 12.6% and the density at this moisture content was found to be 526 kg/m<sup>3</sup> (mean value of 18 samples).

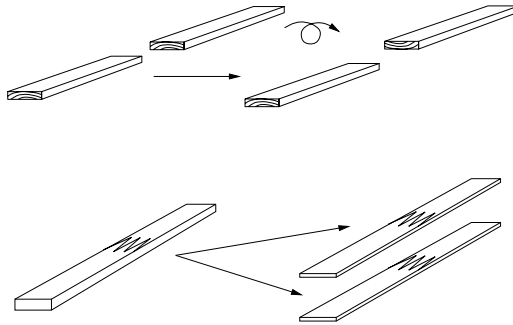


Figure 1: Before the two halves of the sample were joined together again, the one half was rotated 180° about its length axis.

### 2.2 Test Setup and Evaluation

The small specimens cut out from the finger-joints were tested in a bi-axial testing machine in the manner illustrated in Figure 2.

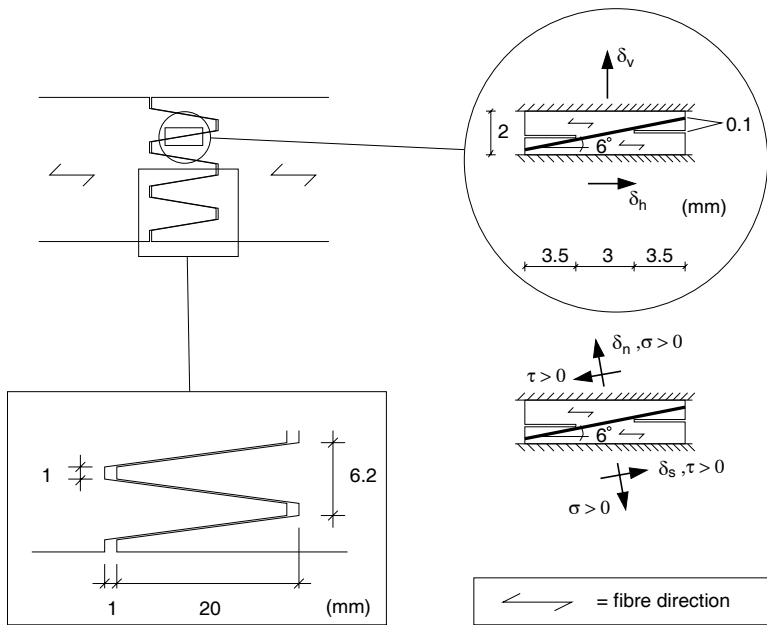


Figure 2: Upper: Specimen for bondline testing with schematic test setup. Lower: Definition of positive quantities used in the constitutive relations.

The testing machine consists of two cross heads that can be controlled by stroke deformation or by force. A bi-axial load cell measuring horizontal and vertical forces was used. The test specimens were attached to the testing machine by glueing them. The testing of small specimens was carried out using displacement control. Vertical relative displacement,  $\delta_v$ , and horizontal relative displacement,  $\delta_h$ , were applied to the specimens. The normal and shear stresses,  $\sigma$  and  $\tau$ , and the corresponding relative displacement across the bondline,  $\delta_n$  and  $\delta_s$ , were recorded. The material data to be evaluated from the tests are strength, fracture energy and the shape of the stress-slip relations  $\sigma - \delta_n$  and  $\tau - \delta_s$ . To enable the recording of the complete stress-slip relations, including their respective descending fracture softening part, the test performance has to be stable in the sense that sudden collapse with an instantaneous decrease of the load must be avoided. When the stress reaches its maximum value, i.e. the strength of the material, fracture softening starts and a localized failure develops. To avoid instability at this instant, the relaxation of the material outside the failure zone must correspond to a deformation smaller than the increasing deformation in the failure zone. This requires large stiffness of the loading equipment and a small size of the specimen.

Three loading paths were tested. These were related to the grain direction of the specimen rather than the bondline direction. The displacements  $\delta_h$  and  $\delta_v$  of the bi-axial testing machine (cf. Figure 2) were set to be parallel to the grain ( $\delta_v = 0$ ), perpendicular to the grain ( $\delta_h = 0$ ) and 2:1 to it (parallel:perpendicular), respectively. Since the bondline direction is somewhat different from the grain direction this results in slightly different paths with respect to bondline directions (approximately 9.5:1, 0.105:1 and 1.57:1). These three modes of testing are henceforth denoted as the shear-deformation

test, the normal-deformation test and the mixed-mode test, respectively. In order to describe the constitutive relations of the bondlines, *uniaxial* strengths are needed. The bondline model, see [2], used in the numerical simulations is based on an interaction formula of the type:

$$\left(\frac{\sigma}{\sigma_{\max}}\right)^m + \left(\frac{\tau}{\tau_{\max}}\right)^n = 1 \quad (1)$$

where  $\sigma_{\max}$  and  $\tau_{\max}$  denote the uniaxial strengths and  $\sigma$  and  $\tau$  denote the normal and shear strength of the bondline for the current mode of loading. The strength of the bondline is defined as the point at which either  $\sigma$  or  $\tau$  starts to decrease. The evaluation of  $\sigma_{\max}$  and  $\tau_{\max}$  from the test results was made by using the interaction formula and a least square fit of the test results. The powers  $m$  and  $n$  were both set to 2.0 which for RP-adhesive have been found to give a good fit to the test results obtained in the present and a previous study [2]. With  $m = n = 2$  Equation (1) coincides with the commonly used Norris failure criterion.

The stroke rate of the testing machine was chosen to be 0.0002 mm/s for the shear and normal-deformation modes and  $(\delta_h, \delta_v) = (0.0001, 0.00005)$  mm/s for the mixed mode tests. This gave approximately the same time to failure for the different tests, a few minutes.

The bondline fracture energy  $G_f$  was calculated as the total work done during the course of loading. This work can be expressed as:

$$G_f = \int_{\Gamma} \sigma d\delta_n + \int_{\Gamma} \tau d\delta_s \quad (2)$$

$\Gamma$  being the deformation path leading to complete separation of the bondline. The deformations  $\delta_n$  and  $\delta_s$  were calculated by transforming the deformations measured by LVDTs in the vicinity of the specimen to a coordinate system coinciding with the bondline directions. The normal stress  $\sigma$  and the shear stress  $\tau$  were calculated from the recorded vertical and horizontal loads. In this calculation uniform stress distribution over the fracture area was first assumed. In the elastic region this assumption is of course not fulfilled, due to the geometric discontinuities. At peak load, however, the stress distribution is more uniform, due to softening taking place along almost the entire bondline. The fairly good uniformity of the stress distribution during softening is due to the small bondline length, 3mm. FE-simulations were performed, so as to verify the assumptions made in the evaluation of the test results. In Figure 3 the stress distribution at peak load for the shear deformation test as calculated with finite elements is shown. The shear stress is not completely uniform, the mean shear stress being approximately 10% off the maximum stress. The evaluation of the test results was therefore performed as an iterative process using FE results like the ones shown in Figure 3 and varying the input data to the bondline model (the strength) until a good fit of the test results was achieved.

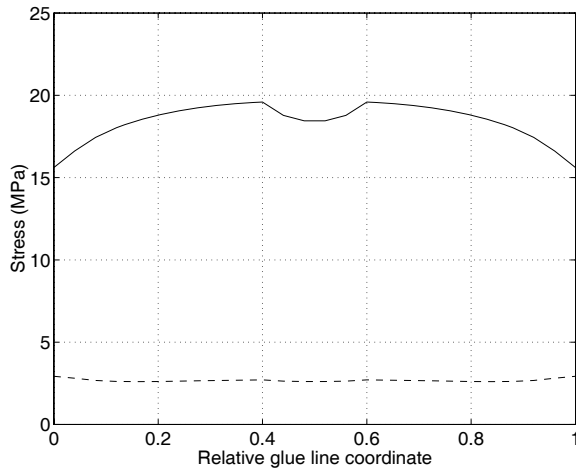


Figure 3: Stress distribution at peak load for a small test specimen. The solid line represents shear stress  $\tau$  and the dashed line normal stress  $\sigma$ .

### 3 Numerical Methods

The numerical study deals with the simulation of finger-joints using the FE method with a nonlinear mixed mode fracture mechanics description of the bondline. The bondline model is based on the concept of gradual fracture softening and was developed by Wernersson [2]. A brief description of the model is given here, for further details reference is made to Wernersson [2].

#### 3.1 A Nonlinear Fracture Mechanical Model for Adhesive Joints

The model uses an expansion of the uniaxial stress against relative displacement properties in pure shear, and in pure normal deformation of a bondline. The uniaxial behaviour is modelled using piecewise linear functions approximating the stress-displacement responses.

An essential feature of the model is the consideration of the gradual fracture softening during increase in deformation beyond the point of peak stress. In other words the model accounts for gradual damage of the material and progressive crack growth. In order to define the constitutive relations for mixed mode loading, the uniaxial properties for pure normal and shear stress are expanded in the  $\delta_n$ - $\delta_s$ -plane (cf. Figure 2). The state of deformation is given by the components  $\delta_n$  and  $\delta_s$  or alternatively, in polar coordinates, by the radial displacement  $\delta$  and the mixed mode angle  $\varphi$ , defined as:

$$\delta = \sqrt{\delta_n^2 + \delta_s^2} \quad (3)$$

$$\varphi = \arctan\left(\frac{\delta_s}{\delta_n}\right) \quad (4)$$



The stress–displacement relation is assumed to retain its piecewise linear shape for radial paths, but vary smoothly with the mixed mode angle  $\varphi$ .

The radial distances  $\delta_k$ , which define the transition from one linear part,  $k$ , to the next,  $k+1$ , are defined by a relation of the type

$$\left(\frac{\delta_{n,k}}{\delta_{n_0,k}}\right)^m + \left(\frac{\delta_{s,k}}{\delta_{s_0,k}}\right)^n = 1 \quad (5)$$

where the indices  $(n_0, k)$  and  $(s_0, k)$  relate to the uniaxial response for normal and shear stress, respectively. In the present study the powers  $m$  and  $n$  in (5) are set to  $m = n = 2$  yielding a quadratic interaction. For each linear part,  $k$ , of the constitutive relation, it is necessary to define the stresses  $\sigma_k, \sigma_{k+1}, \tau_k$  and  $\tau_{k+1}$  at the beginning and the end of the interval. These stresses are related to the corresponding uniaxial stress by the relation

$$\sigma_k = \sigma_{0,k} \frac{\delta_1 \cos \varphi}{\delta_{n_0,1}} \quad (6)$$

$$\tau_k = \tau_{0,k} \frac{\delta_1 \sin \varphi}{\delta_{s_0,1}} \quad (7)$$

The relations describing the constitutive behaviour of the bond line involve coupling effects, normal stress thus depending not only on the opening deformation but also on the shear deformation. This is realistic for the softening region. In the elastic region, defined by

$$\delta \leq \left[ \left(\frac{\cos \varphi}{\delta_{n_0,1}}\right)^m + \left(\frac{\sin \varphi}{\delta_{s_0,1}}\right)^m \right]^{(-1/m)} \quad (8)$$

the constitutive relations are uncoupled. Equation (8) is derived from Equation (5) by replacing  $\delta_{n,k}$  and  $\delta_{s,k}$  by  $\delta_n (= \delta \cos \varphi)$  and  $\delta_s (= \delta \sin \varphi)$ , respectively.

The definition of the non-softening region given in Equation (8) corresponds, for the case of  $m = n = 2$ , to the stress-based failure criterion

$$\left(\frac{\sigma}{\sigma_{max}}\right)^2 + \left(\frac{\tau}{\tau_{max}}\right)^2 = 1 \quad (9)$$

Equation (5) is analogous to Equation (9) and for the elastic region identical (for the case of  $m = n = 2$ ), since the normal and shear stresses are proportional to the deformations  $\delta_n$  and  $\delta_s$ , respectively.

The bondline model is assumed to account for the mechanical behaviour of the adhesive, the adherend material and the adherend/adhesive interface. It is assumed that the bondline thickness is finite although the influence of bondline thickness is neglected in the equilibrium equations, in that no account is taken of normal stresses along the bondline.

The model was implemented in ABAQUS, a commercial, general purpose, finite element code, (Hibbitt *et al.* [5]), as a nonlinear finite element. The element defines the stress-slip relation for two nodes on each side of the bondline.

### 3.2 Finite Element Model of Finger-joint

The wood was assumed to be an orthotropic, linear elastic material having the following engineering constants (x denoting fibre direction):  $E_x = 16.8$  GPa,  $E_y = E_x/30 = 0.56$  GPa,  $G_{xy} = E_x/16 = 1.05$  GPa,  $\nu_{xy} = 0.45$ . The value of  $E_x$  stems from flatwise bending tests and the stiffness relations are taken from Blaß *et al.* [6]. The input data for the bondlines were determined in tests with small specimens according to the description above. The FE-model, shown in Figure 4, consists of about 10500 elements, of which 836 are bondline elements. Each bondline element is 0.5 mm long and 0.1 mm thick. There are about 10900 nodes altogether. Use was made of 4-node isoparametric plane stress elements for the material outside the bondline. A finger-jointed lamination of 421 mm length, 68.2 mm width and 10 mm thickness was simulated. At the ends of the lamination plane cross sections were assumed to remain plane during deformation. This resulted in only three degrees of freedom at each end, of which only the horizontal deformation was prescribed (cf. Figure 4).

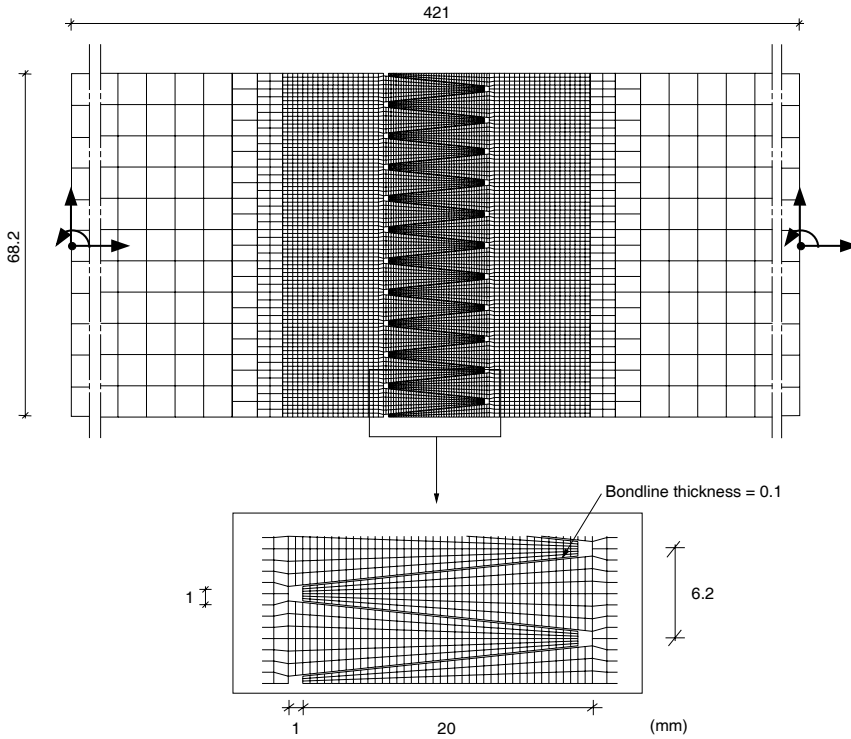


Figure 4: FE-model used in the simulations of finger-joint behaviour.

## 4 Results and Discussion

### 4.1 Bondline Test Results

The RP-adhesive was found to be very brittle, and a total of 16 tests were needed to achieve a total of nine stable tests, three tests for each of the three loading paths. The remaining seven tests were rejected due to unstable test performance. The stress-displacement curves recorded for the RP-adhesive tested in shear-deformation are shown in Figure 5.

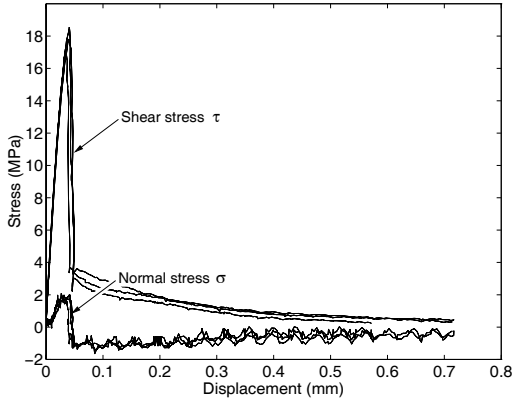


Figure 5: Shear and normal stress versus shear displacement  $\delta_s$  for RP-adhesive in shear-deformation testing.

For the shear-deformation test, normal tensile stress perpendicular to the bondline developed due to the slope of bondline relative the grain orientation. It is noteworthy that after maximum shear stress had been reached in the shear-deformation tests, compressive stress perpendicular to the bondline developed. Although the results for the shear-deformation tests appear almost unstable, the descending part of the stress-displacement curves was in fact recorded during 10-20 seconds, using several samples ranging from maximum load to approximately 3 MPa. The strengths for the small RP-specimens were found to be 21.2 MPa in pure shear and 7.1 MPa in pure normal deformation. These strengths were estimated using Equation (1) with  $m = n = 2$ . The fracture energies were evaluated according to Equation (2) and were found to be 1250, 560 and 440 J/m<sup>2</sup> for the shear, mixed and normal deformation mode, respectively.

### 4.2 Simulation of Finger-joint Behaviour

Using the test results reported above as input for the bondline model, the failure load of the finger-jointed lamination predicted by the finite element calculation corresponds to a maximum tensile stress according to beam theory of 79.9 MPa.

The FE simulations using the above discussed model makes it possible to follow the gradual damage and progressive cracking of the bondlines and predict the failure load of the finger-jointed lamination. It was found that the mostly stressed bondline

element reaches maximum stress and starts to fracture already when the global load is only approximately 25% of its maximum. This load level corresponds to the load bearing capacity predicted by a conventional failure criterion based on a single point maximum stress, i.e. a failure criterion based on the assumption of zero fracture energy. Such a criterion is obviously not appropriate, due to the geometric discontinuities in the finger-joint, leading to high stress concentrations. The lamination strength predicted at the assumption of zero fracture energy would be 20 MPa.

Another extreme is to use a failure criterion corresponding to the failure taking place at completely uniform stress distribution along the bondlines, and the ratio of normal stress to shear stress being equal to the slope of the finger-joint (0.105). This corresponds to the bondline being elastic - perfectly plastic. Such assumptions make it easy to perform hand calculations, but since the fracture energy then is assumed to be infinite the load bearing capacity is overestimated. For the present case the lamination strength predicted using these assumptions is found to be 125 MPa. The strength calculated in this manner closely corresponds to the strength predicted by a fully nonlinear analysis using the present bondline model and assuming the fracture energy to be infinitely large.

A model based on nonlinear softening theory, such as the one employed in this study, can be regarded as a unifying theory that includes the two extremes mentioned above, the brittle failure at zero fracture energy and the perfect plastic failure, as special cases. This model will, correctly calibrated, yield more accurate results for a wider range of bondline brittleness values than the results obtained by using a brittle or a perfectly plastic material model.

The highly nonlinear response of the bondline is shown in Figure 6. This figure shows stress distributions in the outermost bondline of the finger joint at two different instants. To the left an elastic state and to the right for the instant when maximum global load is reached. The elastic state corresponds to all elements in the model behaving linear elastic. As mentioned above this was true for loads < 25% of the maximum load. At maximum global load the bondline is partly damaged and approximately 1/3 of the bondline has started to soften. Despite the strongly nonlinear performance of the bondline, the global loading response of the finger-jointed lamination is very close to linear and from the global perspective the failure appears to be very sudden and brittle.

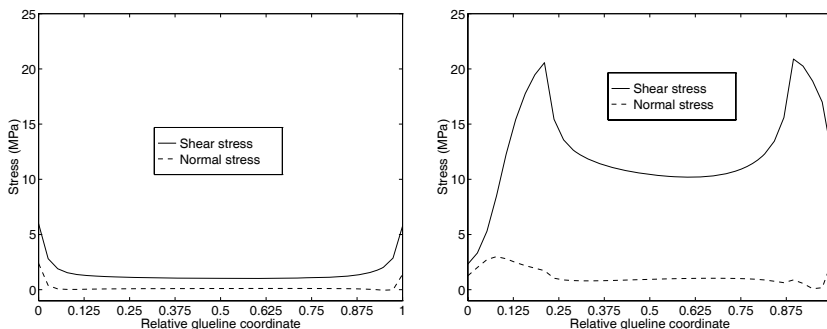


Figure 6: Stress distributions for an elastic state (left) and for the maximum global load state (right) in the outermost bondline of Figure 4.

## 5 Parameter Studies

Parameter studies of factors affecting the load-bearing capacity of finger-joints were carried out. In these studies the FE-model shown in Figure 4 was employed and with the result reported above as a reference case. All FE-simulations were performed using the fracture softening model described above.

### 5.1 Brittleness

The above FE results show that the maximum local elastic stress in the bondline is already very high at a low external loading of the lamination. This means that the fracture softening behaviour of the bondline after peak stress is crucial for the load-bearing capacity of the lamination. The fracture softening can develop in a stable manner only as long as the elastic energy released can dissipate into the fracture process zone(s). The most obvious parameter to vary is thus that of the fracture energy. The strength of the bondline and the stiffness of the wood are other parameters of interest. In performing a parameter study of say the fracture energy, one can proceed in a number of ways. In the present study, the stress-deformation curves of the bondlines are normalized with respect to the strength and the fracture energy of the bondline. The normalized curve, i.e. the shape-function of the curve, is kept constant when the strength or the fracture energy is varied.

From nonlinear fracture mechanics it is a well established fact that the normalized strength of a structure,  $F_{\text{ult}}/(d^2 f_f)$ , is a function of two parameters only, the so-called brittleness number  $\omega$  and a parameter  $\gamma$  that describes the shape of the stress-deformation curve (Gustafsson, [7]). Thus:

$$\frac{F_{\text{ult}}}{(d^2 f_f)} = \mathcal{F}(\omega, \gamma) \quad (10)$$

where  $F_{\text{ult}}$  is the ultimate load-bearing capacity of the structure,  $d$  is a measure of its absolute size and  $f_f$  is a measure of the strength of the material. The brittleness number  $\omega$  is the ratio of the size of the structure to a characteristic length,  $l_{\text{ch}}$ , of the material:

$$\omega = d/l_{\text{ch}} = \frac{d f_f^2}{E G_f} \quad (11)$$

where  $E$  is a general measure of the stiffness of the material, for example the Young's modulus, and  $G_f$  is its fracture energy.

A large brittleness number indicates that a linear elastic fracture mechanics approach is appropriate, whereas a small brittleness number indicates that an approach based on the assumption of a perfectly plastic material is useful. The influence of the brittleness on the load bearing capacity can be studied by nonlinear fracture mechanics using for example the fictitious crack model. A comprehensive study of this sort can be found in the work of Gustafsson [7].

For the present study the different values of  $\omega$  were obtained by changing the fracture energy of the material and maintaining the dimensions of the finger-joint as in Figure 2. For the present study,  $\omega$  is defined as  $(d\tau_{\text{max}}^2)/(EG_{f,II})$ , with  $d = 68.2$  mm and with  $\tau_{\text{max}} = 21.2$  MPa and  $E = 16.8$  GPa according to the above test results.  $G_{f,II}$  is the

mode II fracture energy. Here the shear strength was chosen as the strength measure since the bondlines are in a state of nearly pure shear.

The results obtained at very large brittleness numbers  $\omega$  are somewhat uncertain. This is due to the fracture process zone being smaller for larger values of  $\omega$ , resulting in too coarse an FE-mesh with too few elements in the fracture process zone. The results of this parameter study are shown in Figure 7, where the dashed line indicates the somewhat uncertain values at high brittleness numbers.  $f_t$  indicates the lamination strength, i.e. the maximum tensile stress in the lamination, according to beam theory, at failure of the finger-joint.

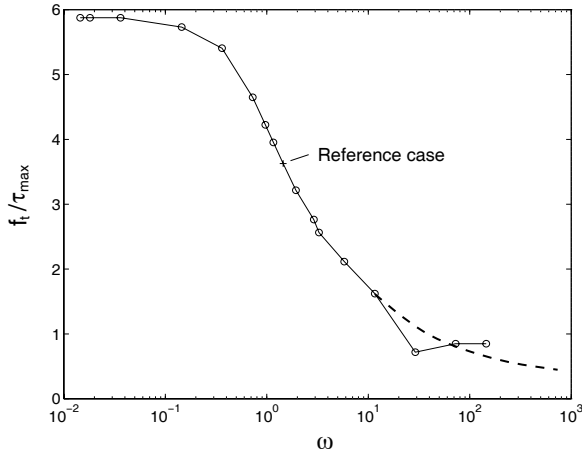


Figure 7: Normalized strength ( $f_t / \tau_{\max}$ ) versus brittleness number ( $\omega$ ).  $f_t$  is the maximum stress in the lamination according to beam theory.

The results indicate that there is a large potential for increasing the strength of finger-joints made with brittle adhesives by increasing the fracture energy of the bondline. From Equation (11) it is apparent that the effect on strength of a change in stiffness of the material surrounding the fracture region is equivalent to that of a change in the fracture energy of the bondline.

## 5.2 Defects

Since finger-joints often are regarded as weak links and the failure of a finger joint is brittle from a global perspective it is of great interest to investigate the influence of defects in the bondline. Therefore several simulations involving defects have been performed. Here a defect is equivalent to a void, which is simulated by simply removing a number of bondline elements.

First a study of the influence of having a single defect in the outermost bondline, placed at different locations, was performed. The results from this study are shown in Figure 8. It is found that a single small (1 mm) defect in the outermost bondline can cause an approximately 12% reduction of the lamination strength. This strong influence of a defect which represents less than 0.25 % of the total bond length in the joint is due to the brittleness of the adhesive. Use of a more ductile adhesive would reduce

the influence of such defects. Since the finger-joint contains geometric discontinuities already without the defect, the influence of the defect is surprisingly large.

The second type of investigation regarding defects is presented in Figure 9. Here each curve represents a series of simulations for which a single defect of varying size has been assumed at a certain finger-tip. Four different positions of a single defect were investigated (A-D). It is seen that for the small defect size studied position A causes the highest strength reduction.

The outermost finger of the lamination is the one that is most sensitive to defects. This can be shown by simulating a small defect at *every* finger-tip of the lamination. Table 1 shows the results of such simulations. The difference between having a single small defect at the outermost finger-tip and having defects at every finger-tip is negligible.

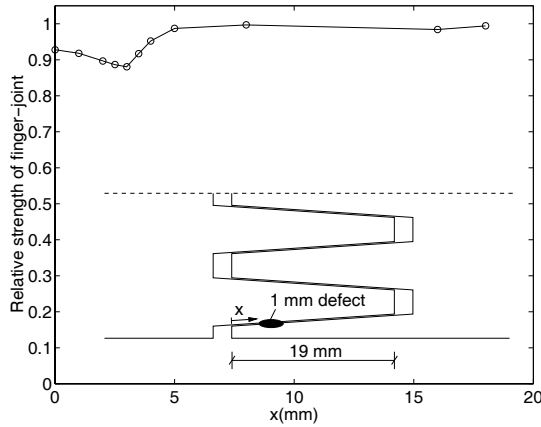


Figure 8: Relative strength of a finger joint with a single defect at different distances from finger-tip.

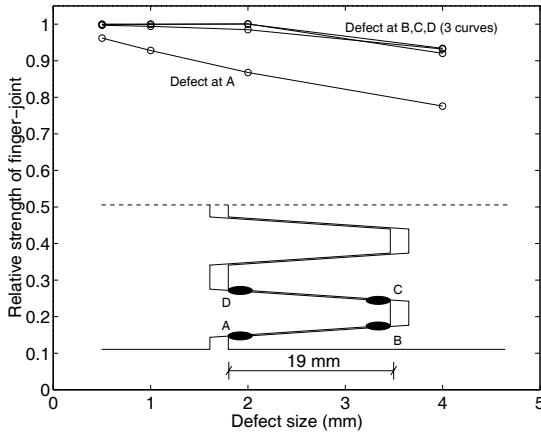


Figure 9: Relative strength of a finger joint with a single defect of different size. 4 different positions of the defect (A-D).

Table 1: Influence of defects in the bond line(s) on the strength of a finger-joint. Numerical predictions by FEM. The strengths,  $f_t$ , are given in relation to the strength in the reference case,  $f_{t,0}$ .

Size of defect (mm)	1 defect $f_t/f_{t,0}$	Defects at every finger $f_t/f_{t,0}$
0.50	0.960	0.956
1.00	0.923	0.913
2.01	0.860	0.830
4.02	0.767	

### 5.3 Finger-joints with Adherends of Dissimilar Stiffness

Since wood is a material showing large variability in its material properties, it is very likely that the two halves of a finger-joint are dissimilar in stiffness. Therefore analyses were performed in which the Young's modulus of one half of the finger-jointed lamination was varied. Since the reference value for the Young's modulus is rather high,  $E_x = 16.8$  GPa, this study was performed by letting one half of the finger-jointed lamination consist of a material with lower Young's modulus. The ratios between the orthotropic stiffness parameters were kept unchanged so that:  $E_x/E_y = 30$ ,  $E_x/G_{xy} = 16$ ,  $\nu_{xy} = 0.45$ .

A series of analyses involving reduced  $E_x$  in the left and in the right half of the model, respectively, were performed using the FE-model shown in Figure 4. The reduction in the elastic constants was 20, 40 and 60%, respectively, corresponding to a modulus of elasticity in the fibre direction of 13.44, 10.08 and 6.72 GPa. The stress distribution in the outermost bondline is not exactly symmetric and the case of the left side having a lesser stiffness is more strength reducing. This can be explained by looking at the right side of Figure 6: the left half of the bondline is more severely stressed than the right half. Now if the stiffness of the left half of the lamination is lower than that of the right half, the stresses transferred by the bondline are concentrated to the left half even more, resulting in the load-bearing capacity of the finger-joint being lowered. It should be noted that the simulations were made assuming the failure of the finger-joints to take place in the bondline and not in the wood itself. Since the strength of wood can be assumed to be correlated to its stiffness, it is possible, that large stiffness variations tend to lead to wood failure. The results of the parameter study are summarized in Table 2. The results show that the strength of a finger-joint can be just as much influenced by only one of the pieces being of low stiffness as if the mean value of the stiffnesses is low.



Table 2: Influence on the strength,  $f_t$ , of finger-jointing pieces of dissimilar stiffness. Numerical predictions by FEM. Reference value of Young's modulus is  $E_0 = 16.8$  GPa.

$E_{\text{left}}/E_0$	$E_{\text{right}}/E_0$	$f_t$ [MPa]	$\Delta f_t$ [%]
1.0	1.0	79.9	0
0.8	1.0	69.3	-13
0.6	1.0	57.5	-28
0.4	1.0	46.7	-42
1.0	0.8	75.4	-6
1.0	0.6	61.9	-23
1.0	0.4	47.2	-41
0.8	0.8	73.4	-8
0.6	0.6	65.3	-18
0.4	0.4	54.6	-32

## 6 Conclusions

The following conclusions can be drawn from the present study.

- The strain softening behaviour of a resorcinol-phenol (RP) adhesive bondline cut out from a finger joint was recorded in stable tests for different modes of loading.
- A nonlinear fracture softening model was implemented in a finite element software and used to predict the behaviour of a wooden finger-joint.
- The strength of the finger-joint showed to be strongly influenced by the behaviour of the bondline after peak stress.
- For the examined RP-adhesive there is a large potential of increasing the finger-joint strength by increasing the bondline fracture energy.
- Parameter studies performed showed the finger-joint strength to be strongly dependent on the presence and location of small defects (voids) in the bondline, especially in the outermost bondline.
- Parameter studies showed the finger-joint strength to be strongly influenced by the stiffness of the lamination and by difference in stiffness of the two finger-joint halves.

## References

- [1] Colling, F., Tragfähigkeit von Biegeträgern aus Brettschichtholz in Abhängigkeit von den festigkeitsrelevanten Einflußgrößen. Berichte der Versuchsanstalt für Stahl, Holz und Steine der Universität Fridericiana, Karlsruhe, Germany, 1990.
- [2] Wernersson, H., Fracture Characterization of Wood Adhesive Joints. Report TVSM-1006, Lund University, Division of Structural Mechanics, Lund, Sweden, 1994.
- [3] Serrano, E., Finger-joints for Laminated Beams. Experimental and numerical studies of mechanical behaviour. Report TVSM-3021, Lund University, Division of Structural Mechanics, Lund, Sweden, 1997.
- [4] Aicher, S., Klöck, W., Spannungsberechnungen zur Optimierung von Keilzinkenprofilen für Brettschichtholz-Lamellen. Bauen mit Holz. Vol. 92(5), pp. 356-362, 1990.
- [5] Hibbitt, Karlsson & Sorensen, ABAQUS Users' manual, Version 5.5. Pawtucket, RI, USA, 1995.
- [6] Blaß, H. J. *et al.* (ed.), Timber Engineering STEP 1. Basis of design, material properties, structural components and joints. First edition, Centrum Hout, The Netherlands, 1995.
- [7] Gustafsson, P. J., Fracture Mechanics Studies of Non-yielding Materials Like Concrete: Modelling of Tensile Fracture and Applied Strength Analyses. Report TVBM-1007, Lund Institute of Technology, Division of Building Materials, Lund, Sweden, 1985.



# *Paper IV*

---

*Modeling of Finger-joint Failure in  
Glued-laminated Timber Beams*

*by*

*Erik Serrano, Per J. Gustafsson and Hans J. Larsen*

*Submitted for publication in ASCE – Journal of Structural Engineering*



# Modeling of Finger-joint Failure in Glued-laminated Timber Beams

Erik Serrano<sup>1</sup>, Per J. Gustafsson<sup>2</sup> and Hans J. Larsen<sup>3</sup>

*Submitted for publication in ASCE – Journal of Structural Engineering*

## Abstract

This paper presents a novel approach to the modeling of failure of finger-joints in glued-laminated beams. A nonlinear strain-softening model with stochastic material parameters was used to characterize the failure zone of the finger-joint. Monte Carlo simulations of the behavior of finger-jointed laminations and of laminated beams were performed using the finite element method. Various lamination thicknesses and beam depths were investigated, as well as the effect of varying the ductility of the finger-joint. Finally the use of simplified finger-joint material models was also investigated. The results show that the proposed approach can account for such phenomena as the size effect and the laminating effect. Another observation is that the finger-joint ductility has a major influence on the lamination and beam strength and that a special case of the present modeling approach can be made to coincide with the classic weakest link theory of Weibull.

**Keywords:** laminated wood, glued-laminated timber, finger-joint, laminating effect, size effect, tensile strength, bending strength, finite element analysis

## 1 Introduction

### 1.1 Background

The present study is part of a research project dealing with the properties of finger-joints and laminated wood products. The overall aim of this research project is to contribute knowledge and methods to the rational modeling, analysis and prediction of the strength of glued-laminated timber (glulam).

To predict the strength properties of glulam two methods are, in principle, possible:

- testing of a number of glulam members, using a sample size sufficiently large to determine the properties on a statistical basis
- using a model, verified by testing, linking the properties of the glulam to the properties of the individual laminations.

---

<sup>1</sup>Division of Structural Mechanics, Lund University, P.O. Box 118, SE-221 00, Lund, Sweden. Telephone: +46 46 222 95 88. Fax: +46 46 222 44 20. E-mail: Erik.Serrano@byggmek.lth.se

<sup>2</sup>Assoc. Prof., Division of Structural Mechanics, Lund University, Sweden.

<sup>3</sup>Prof., Division of Structural Mechanics, Lund University, Sweden.

Taking into account the many parameters influencing the properties of glulam - e.g. timber species and grade, lamination thickness, the properties of finger-joints, member depth - and the number of specimens needed, the former method is clearly too expensive as a general method. A model which makes it possible to estimate the properties of glulam from those of the laminations is therefore desirable. In addition, a rational model adds to the understanding of glulam behavior.

## 1.2 Previous Work

Several models to predict the behavior of glulam have been proposed by e.g. Foschi and Barrett (1980), Ehlbeck et al. (1985) and Colling (1990) – known as the “Karlsruhe model”, Hernandez et al. (1992), Nestic et al. (1994), Faye et al. (1996) and Renaudin (1997). All these models, except those of Hernandez et al. and Nestic et al., are based on a subdivision of the glulam member into elements, frequently standard finite elements. Loading is applied to the beam, and the stresses in all the elements are evaluated. This is done for the centroid of the element, each element having the same height as the lamination. The models of Hernandez et al. and Nestic et al. use transformed section methods (based on beam theory) to calculate the stresses at the mid-depth of each lamination, to determine the ultimate load-bearing capacity of the beam. This means that in all models the stress at mid-depth of a lamination is used as a measure of the risk of failure.

The original model of Foschi and Barrett was based on a brittle stress criterion, i.e. when the stress in the most stressed element was equal to the strength the beam was considered to have no load-bearing capacity left. Later models introduced the nonlinearities in compression and accounted for stress redistribution when an element failed in tension: failed elements were removed, and the beam response re-calculated.

In the Karlsruhe model, the finger-joints are assumed to be brittle and failure in a finger-joint means failure of the entire beam. For tensile failure in the wood, the surrounding elements are assumed to take up the released stresses.

In the model proposed by Renaudin, the failure of an element results in redistribution of stresses to neighboring elements, following explicit rules that have been set up using finite element analyses of the stress distributions in the vicinity of the cracks resulting from the failure.

Although a locally brittle response of the material in tension is assumed in all the above models, the assumption of redistribution of stresses after failure introduces a considerable amount of ductility in the model at a global level.

In Serrano and Larsen (1999), using both linear elastic fracture mechanics and non-linear fracture mechanics, the behavior of a beam after failure in the outer lamination was studied. It was assumed that a crack is formed at the failed section in the glue line between the outer and the second lamination, and the condition for that crack being stable, which is a condition for redistribution of stresses, was investigated. By a stable crack is meant a crack which will propagate only by increasing the load, in other words the initial failure of the finger-joint does not lead to a total collapse of the beam. A stable crack-propagation along the outer lamination can take place, but only for small lamination thicknesses, typically less than 10 mm. A series of linear elastic finite element analyses also showed that commonly made assumptions regarding the stress distribution in glulam beams are not always true. A beam loaded in pure bending was simulated.

The outer lamination on the tension side was assumed to contain a zone with lower stiffness than the rest of the beam. The influence of the length of this low-stiffness zone was investigated. As an example, it was found that for a small length of this zone (30 mm) the mean stress in the outer lamination was only reduced by 3% for a 25% stiffness reduction.

A number of theoretical, numerical, studies on finger-joints have been presented in the past. Mostly linear elastic stress analyses are used in these studies, in order to assess the influence of adherend stiffness, Leichti (1988), finger geometry, Aicher and Klöck (1990) and defects, Pellicane (1994). Other studies are concerned with the use of special high aspect ratio finite elements, Milner and Yeoh (1991) and Pellicane (1992). Aicher and Klöck (1991) presented results from nonlinear analysis using plasticity theory and from linear elastic fracture mechanics analysis in order to examine the influence of finger-geometry on tensile strength. A recent study on this theme is also presented by Aicher and Radovic (1999). Wernersson (1994), showed that a nonlinear fracture mechanics approach can be useful in obtaining the response of a timber finger-joint and, using the same approach, Serrano and Gustafsson (1999) investigated the influence of defects on the strength of finger-joints.

In Serrano (1997) an experimental and numerical investigation on the behavior of finger-joints is presented. It was found that it is possible to simulate the strain-softening behavior of a finger-joint in pure tension. It was also found that a brittle and apparently linear elastic behavior, from a global point of view, was strongly influenced by the local nonlinear behavior of the bond line.

The properties of the outer laminations, especially the strength of the finger joints, are very important for the modeling of glulam, Ehlbeck et al. (1985) and Colling (1990). Using as a failure criterion the fact that the mid-depth stress in the outer lamination corresponds to the tensile strength of the lamination, defined as the average stress at failure in a uni-axial tension test, is far too primitive. Nevertheless, as mentioned above, this is the failure criterion used in previously proposed models. Instead a failure criterion which includes the response of the complete lamination depth and permits a progressive failure through the lamination is thought to be more appropriate. Using such a failure criterion, the present study shows that the mid-depth stress criterion is obtained only as a special case for large beam depths.

The use of the mid-depth stress in a failure criterion is one of the reasons why the theoretical models are not used in practice to determine the properties of glulam. Instead, semi-empirical models, e.g. the one proposed in Schickhofer (1996), are used. They are, however, only valid within a small parameter range.

In the following, a more detailed modeling of the finger-joint failure in a glulam beam is described. The modeling is more detailed in the sense that it takes into account the variability *within* the outer tension lamination and also the possibility of progressive failure and crack propagation within the lamination. In principle, it is possible to use the same type of detailed modeling approach for the failure of the wood or for the bond line between the laminations.



## 2 Present study

### 2.1 Aim

The aim of the present study is:

- to establish a better fundamental understanding of the failure mechanisms of finger-joints in glulam, by
- setting up a detailed model of a finger-joint, using an approach based on non-linear fracture mechanics (NLFM) assuming that the material parameters are stochastic, and
- to use the finger-joint model in finite element simulations, and investigate behavior of the finger-joint and laminated beams in terms of a) size effect, b) depth effect, c) laminating effect and d) effect of finger-joint ductility

In order to isolate the effect of the modeling approach used for the finger-joint, the wood outside the finger-joint region is regarded as a homogeneous material with deterministic properties. Consequently, it has not been possible, nor the aim of the present study, to validate the glulam beam analyses with independent test data. However, the present modeling approach can be included into existing glulam beam models such as those discussed above, which use sophisticated modeling for the wood variability.

### 2.2 Model Description

Wood is known to be a material with highly variable properties and several options to model the wood material and the finger-joints exist: deterministic or stochastic models which in turn can be linear, nonlinear or perfectly plastic to account for plasticity, damage or crack formation. For the finger-joints a rigid model could also be used. Different possibilities of modeling the stress-deformation properties of a finger-joint are shown schematically in Fig. 1.

In the models taking the variability into account, the stochastic parameters can be correlated or not. The types A, B and D can be regarded as different special cases of C, and the deterministic modeling as a special case of stochastic modeling.

The present study primarily concerns the behavior of the finger-joints and their influence on lamination tensile strength and beam bending strength. In order to isolate the effect of the finger-joints the material outside the finger-joint region is modeled in the simplest possible way, as a linear elastic, orthotropic and homogeneous material with deterministic properties. The bondline between the outer tension lamination of a beam and the next lamination was modeled with a nonlinear bondline model. However, it turns out that for all cases studied, the stresses in this bondline are within the linear elastic range.

The finger-joint is modeled with a number of parallel nonlinear spring elements of initial zero length, see Fig. 2.

Due to the zero initial length, the elongation of such a spring is associated with crack formation and represents the local additional deformation due to the presence of the finger-joint. Each spring is assumed to represent the response of a finger-joint area

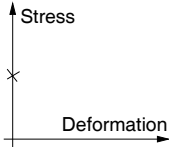
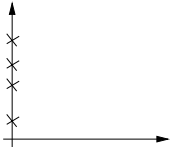
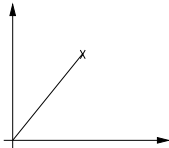
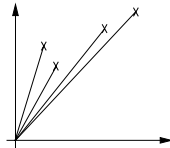
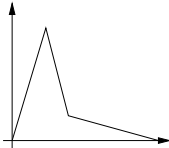
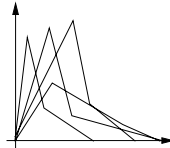
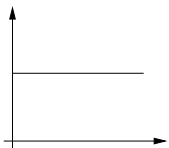
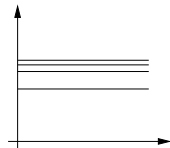
Material properties	I. Deterministic	II. Stochastic
A. Rigid 1 parameter $f_t$		
B. Linear 2 parameters e.g. $f_t + k$ , $f_t + G_f$		
C. Nonlinear several parameters		
D. Plastic 1 parameter $f_t$		

Figure 1: Different approaches of modeling the stress vs. the deformation response of a finger-joint.  $f_t$  is the strength,  $k$  is the stiffness and  $G_f$  is the fracture energy.

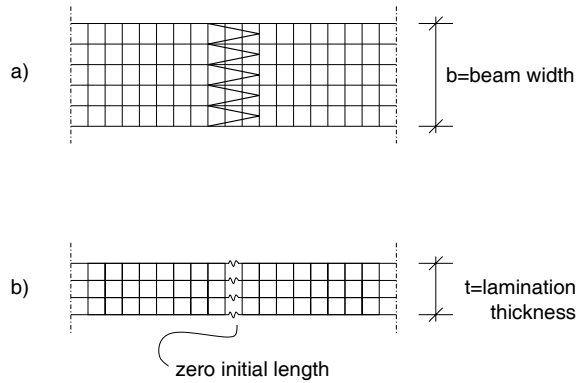
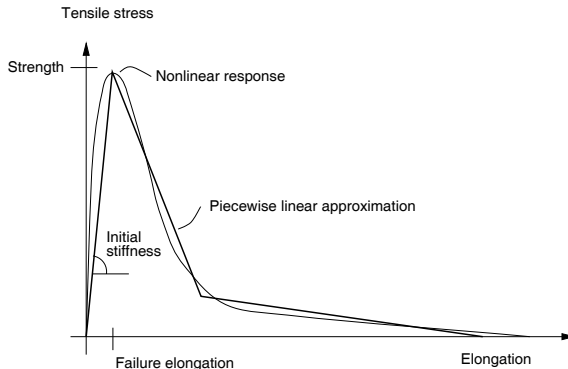


Figure 2: Schematic of finger-joint and FE-modeling used in a) Serrano (1997) and b) in the present study.

defined by the lamination width times the distance between neighboring nodes in the height direction of the lamination. The present modeling is thus closely related to a so called fictitious crack model, a fracture mechanics model for describing the gradual localized damage of a material, Hillerborg et al. (1976), Gustafsson (1985).

The finger-joint spring characteristics are chosen in line with results from tests and elaborated wide face FE-modeling of finger-joints (Serrano 1997), see Fig. 2a, taking into account the finger geometry and the nonlinear bondline performance. The nonlinear responses of the finger-joint springs are described by piecewise linear relations, see Fig. 3, and it is assumed that the stress-elongation relations are linear up to failure.



*Figure 3: Nonlinear stress-elongation response of a finger-joint and a piecewise linear approximation.*

The finger-joint springs are characterized by strength, elongation at failure and the shape of the force-elongation curve. The strength and the elongation at failure are both described by an average value and a coefficient of variation (COV). Furthermore it is assumed that these variables are spatially uncorrelated, i.e. the strength at a certain location does not depend on the strength at any other location. This is an assumption which is used e.g. in classic Weibull-theory, Weibull (1939)

The present modeling of the finger-joint thus corresponds to a modeling of type C in Fig. 1.

The present study primarily concerns the bending strength of laminated beams of different height and with different lamination thicknesses, with a finger-joint located in the outer tension lamination. The beams are subjected to pure bending and analyzed using the finite element method.

### 2.3 Finite Element Implementation

In the finite element models, plane stress conditions are assumed, and due to symmetry only one half of the beam is modeled. The finger-joint is located in the symmetry plane, resulting in the finger-joint nonlinear springs acting in pure tension. The total length of the beam is set to be 1 m, which is enough to avoid boundary effects of the loading which is imposed by rotating the end sections of the beam. The end sections are assumed to remain plane during deformation. The total number of elements are 3900–5700 and the number of nodes are 4100–6000 for the different beam sizes. An example of the

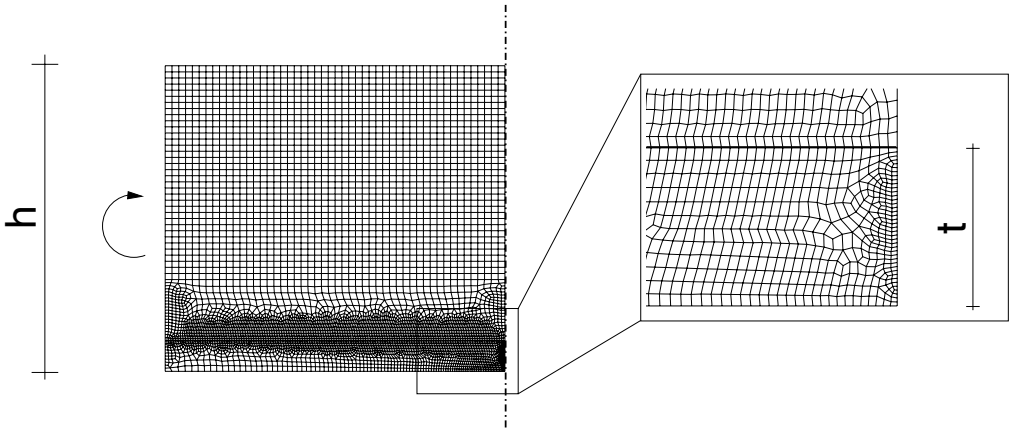


Figure 4: FE-mesh used for beams with  $h = 450$  mm and  $t = 45$  mm.

FE-mesh used for the beam height,  $h$ , being 450 mm and the lamination thickness,  $t$ , being 45 mm is shown in Fig. 4.

The wood is treated as a linear elastic orthotropic material with  $E_x = 16800$  MPa,  $E_y = E_x/30 = 560$  MPa,  $G_{xy} = E_x/16 = 1050$  MPa,  $\nu_{xy} = 0.45$ . Here  $x$  denotes the fiber direction which is assumed to coincide with the beam axis. The value of  $E_x$  was taken from an investigation by Serrano (1997) and stems from flatwise bending tests on finger-jointed laminations. Although the value of  $E_x$  is rather high, due to use of high quality clear wood specimens, the results of the present study are believed to be valid also for lower values of  $E_x$ . In Serrano (1997), the main aim was to accurately monitor the response of a finger-jointed lamination in tension under conditions similar to those of a lamination contained in a glulam beam. Therefore the tests were performed with clamped ends and a short free specimen length (approximately 200 mm). The specimens were 70 by 10  $mm^2$  with a 20 mm long finger-joint visible on the wide face of the lamination. Ten strain gauges mounted within 20 mm from the finger-joint and two 150 mm long LVDT's were used to monitor the straining.

The bondline of the outer tension lamination is modeled with nonlinear bondline elements, Serrano and Larsen (1999). However, for all cases the stresses in this bondline are within the elastic region.

To calibrate the input data of the nonlinear springs, test results from the tensile tests on finger-jointed laminations mentioned above were used (Serrano 1997). The idea of the present study is to link the properties of large scale specimens to those of smaller scale specimens. Therefore it was decided to calibrate the model for 10 mm thick specimens and calculate the response of laminations of other thicknesses.

The tests in Serrano (1997) were performed on different adhesive types and only three nominally equal tests were made, so that the variability in strength could not be accurately determined from this test series, but was estimated to be in the range of 15%. From this test series, finger-joints glued with a commonly used resorcinol-phenol adhesive were chosen for the calibration. Their mean strength was approximately 55 MPa.

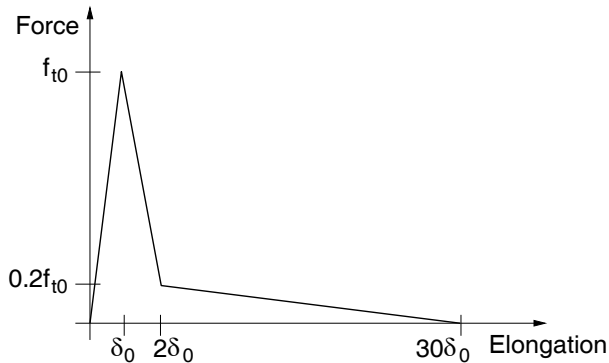


Figure 5: Nonlinear force-elongation response of a finger-joint spring element.

The shape of the force-elongation curves of the springs was set to be according to Fig. 5, which is in line with the results reported in Serrano (1997). The tri-linear shape of the curve as given in Fig. 5 is the simplest possible shape which still captures the most important features of the force-elongation response. These features include the linear elastic behavior up to maximum load which was also recorded in the tests, Serrano (1997), followed by strain softening at two distinctively different slopes. Such strain softening shape on the stress-deformation behavior has been obtained in tests of wood adhesive bonds, Wernersson (1994) and Serrano (1999). Using this shape it is possible to determine the spring response in terms of two parameters only, the strength and the failure elongation of the spring,  $f_{t0}$  and  $\delta_0$  respectively.

To obtain the appropriate model parameter values, i.e. strength and failure elongation of the finger-joint springs, an iterative procedure was used. Initially it was assumed that the failure elongation of the springs was deterministic and equal to  $\delta_0 = 0.02$  mm. Assuming furthermore a log-normal distribution for the strength of the springs,  $f_{t0}$ , the mean value, denoted  $\bar{f}_{t0}$ , and the COV were varied in a number of FE-simulation series, each consisting of 1000 simulations, until the mean tensile strength of the lamination was close to 55 MPa (same as above), and the COV of the tensile strength 15% (same as above). This mean and COV of lamination strength was achieved for  $\bar{f}_{t0} = 82$  MPa and a COV of 40%. Following this, the failure elongation was also assumed to be a log-normal distributed stochastic variable, uncorrelated with the strength and with a mean value of  $\bar{\delta}_0 = 0.02$  mm and a COV equal to 40%. New simulations were performed, changing the mean strength and COV of the springs, until the mean and COV of lamination strength again were 55 MPa and 15% respectively. This mean and COV of lamination strength was finally achieved for the mean and COV of the spring strength being  $\bar{f}_{t0} = 80$  MPa and 30% respectively.

The above reported calibrated values of strength apply to all springs that are not located on the edge of the lamination. In these inner parts of a lamination, each nonlinear spring represents a finger-joint area of  $b \times 1.125$  mm<sup>2</sup>. Here  $b$  is the width of the beam and the 1.125 mm represent the distance between the nodes along the symmetry plane. Since the edge springs represent only half of this area, it is reasonable to give them a higher strength value. This was done according to the weakest link theory of Weibull (1939), using the 2-parameter Weibull distribution. For the present values of  $\bar{f}_{t0} = 80$

with a COV of 30%, this means that the edge springs were given an approximately 20% larger value of  $\bar{f}_{i0}$ . The calibrated values are given in Table 1.

Table 1: Calibrated spring characteristics. Log-normal distribution.

Parameter	Mean	COV
$f_{i0,inner}$	80.0 MPa	30%
$f_{i0,edge}$	96.4 MPa	30%
$\delta_0$	0.02 mm	40%

## 3 Results

### 3.1 General Remarks

The finite element simulations performed involve four major simulation series:

1. Bending strength of laminated beams. Three different heights,  $h = 135, 450$  and  $900$  mm and two different lamination thicknesses  $t = 33$  and  $45$  mm.
2. Tensile strength of laminations with thickness  $t = 10, 33$  and  $45$  mm.
3. The effect of finger-joint ductility on the tensile strength of a lamination and on the bending strength of a beam.
4. The effect of using a simplified finger-joint material model on the bending strength.

The statistics from the FE-Monte Carlo simulations are presented with a mean value and a corresponding 95%-confidence interval of the mean value, lower 5th percentile values and the COV. The bending strength is estimated using the ultimate bending moment from the finite element simulations and assuming ordinary beam theory to be valid. The lower 5th percentile values given are distribution-free estimates. All strength statistics are based on 1000 simulations.

From the results of simulation series 1 and 2, different factors relating to the strength of glulam beams and laminations are calculated. Since these factors are inconsistently defined in literature, the definitions used here are given:

**Size effect** – For a structure of fixed geometrical shape, the effect that the strength, as evaluated in terms of force/unit area, diminishes with an increasing size. For a glulam beam, the fixed geometrical shape means that the lamination thickness increases with increasing beam depth.

**Depth factor (in bending)** – For a beam in bending, the effect that the strength diminishes with an increasing depth. The other geometric parameters are kept constant, e.g. lamination thickness.

**Laminating effect** – The effect that the strength of a lamination increases when contained in a beam. Also the effect that the bending strength increases for a beam at decreasing lamination thicknesses.

### 3.2 Bending Strength and Tensile Strength

In Table 2, the bending strength statistics are given for the beam geometries investigated. Three different beam depths,  $h$ , and two different lamination thicknesses,  $t$ , were investigated.

*Table 2: Beam bending strength statistics.*

$h$ (mm)	$t$ (mm)	Mean (MPa)	5% (MPa)	COV (%)
135	45	58.4±0.5	44.6	14
450	45	51.5±0.4	41.0	12
900	45	49.5±0.4	39.6	12
135	33	58.6±0.5	44.7	14
450	33	52.3±0.4	41.3	12
900	33	50.8±0.4	40.4	12

The greater the depth of the beam, the closer the state of pure tensile stress is achieved in the outer lamination. Therefore, for comparison with the beam bending results, a series of simulations was performed involving pure tension of laminations, 33 and 45 mm thick. These results are summarized in Table 3. For comparison, the results from the calibration procedure are also given in Table 3 ( $h = t = 10$  mm).

*Table 3: Lamination tensile strength statistics.*

$h = t$ (mm)	Mean (MPa)	5% (MPa)	COV (%)
10	55.4±0.5	41.8	15
33	48.3±0.4	38.5	12
45	46.8±0.3	38.1	12

### 3.3 Effect of Size, Depth and Lamination Thickness

From the results reported above, it is possible to derive a number of factors related to the strength of the laminations and beams as a function of size, depth and of the lamination thickness according to the definitions above.

The size effect found for the different lamination thicknesses in pure tension is shown in Fig. 6.

The curves represent least square fits of a power relation according to:

$$f_t = f_{t0} \left( \frac{t}{1.125} \right)^{-\beta} \quad (1)$$

where  $f_t$  is the tensile strength of a lamination of thickness  $t$  mm and  $f_{t0}$  is the strength of the reference area of the finger-joint, i.e. the strength of the nonlinear spring. It is

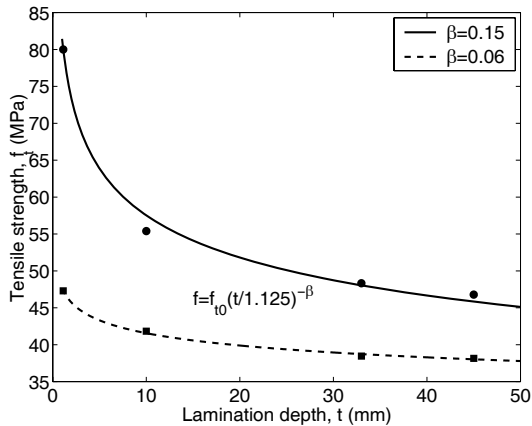


Figure 6: Size effect in pure tension. The solid line and dots represent mean values and the dashed line and squares represent lower 5th percentile values.

evident that the present model gives a size effect that is less pronounced at the lower 5th percentile level than at the mean value level.

The depth factors calculated are relative bending strengths, with the strength of a beam with  $h = 600$  mm and  $t = 45$  mm as reference. This beam depth was not simulated in the present study, and the strength values of this beam were computed using linear interpolation. The reason for using  $h = 600$  mm as reference is that this is also used in the present Eurocode 5 which states that a depth factor  $k_h$  should be used for beam depths  $h$  less than 600 mm.  $k_h$  is given by:

$$k_h = \min \left\{ \begin{array}{l} \left( \frac{600}{h} \right)^{0.2} \\ 1.15 \end{array} \right. \quad (2)$$

The relative strengths are given in Fig. 7 which shows that the depth factor is different for the mean values as compared to the characteristic values, and that the depth factor depends on the lamination thickness.

The apparent strength increase of laminations when contained in beams of different depths was calculated and the results are given in Fig. 8. Here the strength increase is defined as the ratio of beam bending strength to single lamination tensile strength. Finally the laminating effect due to the use of thinner laminations is given in Table 4. Here the bending strength of a beam with  $t = 45$  mm is compared with a beam having a lamination thickness of  $t = 33$  mm.

### 3.4 Influence of Finger-joint Ductility

A series of simulations was performed to investigate the influence of the finger-joint ductility on the tensile strength of a lamination. Here the ductility of the finger-joint is defined by its fracture energy, which is equal to the area under the stress-elongation curve. This fracture energy is equal to the energy required to fully separate a unit area of the finger-joint.



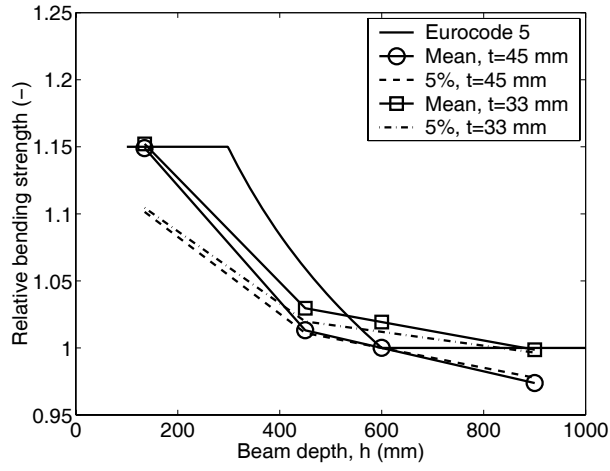


Figure 7: Relative bending strength (depth factors).

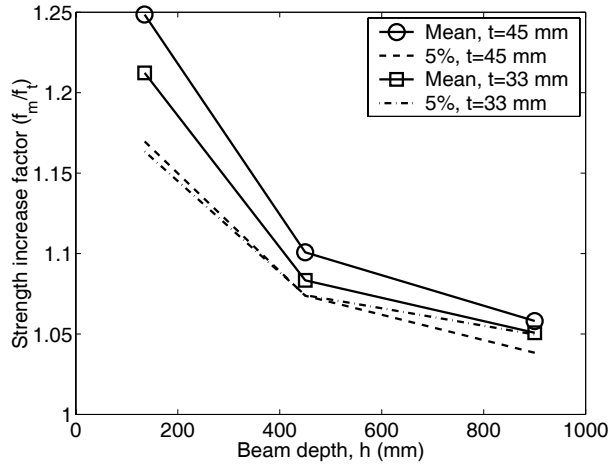


Figure 8: Strength increase factors.

Table 4: Relative bending strength for thinner laminations ( $f_{t=33}/f_{t=45}$ ).

$h$ (mm)	Mean (MPa)	5% (MPa)
135	1.00	1.00
450	1.02	1.01
900	1.03	1.02

The different ductilities were simulated by changing the positions of the breakpoints,  $\delta_0$ , of the piecewise linear response of the nonlinear springs, cf. Fig. 5. Two different approaches were tested, one where all three breakpoints were changed and one where the initial stiffness was unchanged. Changing all the breakpoint positions results in a change of the initial stiffness of the springs so that the ratio of the spring stiffness to the wood stiffness will be different for different values of the fracture energy. This results in turn in different linear elastic stress distributions for different fracture energy values. However, keeping the initial stiffness of each spring constant gives as a result that the linear elastic stress distributions are equal, irrespective of the fracture energy. Therefore, for this case there exists a minimum mean tensile strength of the lamination which is the one obtained for the case of a weakest link failure.

The mean fracture energy of the springs was for the reference case  $G_f = 6.4 \text{ kJ/m}^2$  and the different simulations represent fracture energies of this value multiplied by factors varying between 0.125 and 8. The case of pure tension for a 45 mm thick lamination was investigated and the results are presented in Fig. 9, showing the mean values and error bars, corresponding to 95% confidence intervals. The dashed line represents the results when all breakpoints of the stress-elongation curve are changed and the solid line represents the case with the initial stiffness kept constant. Fig. 9, solid line, shows that the reference case ( $G_f = 6.4 \text{ kJ/m}^2$ ) almost coincides with a weakest link failure, since the tensile strength diminishes very little for smaller values of fracture energy.

Using the concept of letting the initial stiffness of the springs being unchanged, a series of simulations was performed in order to investigate the effect of finger-joint ductility on the beam bending strength. Here the case of a 450 mm deep beam with a 45 mm thick lamination was investigated. The results from this study are also depicted in Fig. 9, dashed-dotted line. Fracture energy values ranging from  $G_f = 6.4 \text{ kJ/m}^2$  for the reference case to eight times this value were investigated. The strength increase found for the beam bending strength is in line with the lamination tensile strength increase.

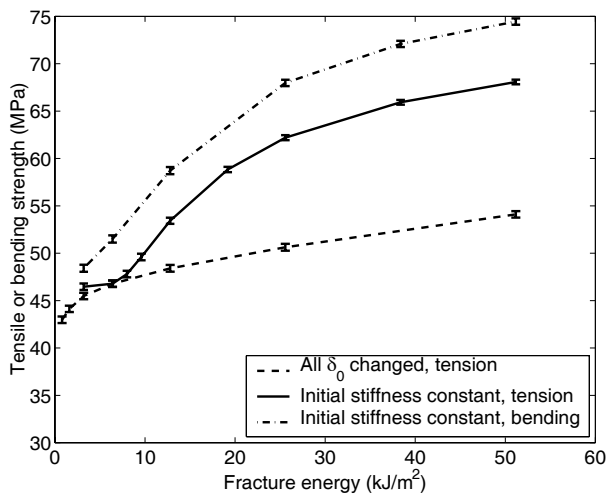


Figure 9: Influence of fracture energy on tensile and bending strength.  $t=45 \text{ mm}$  and  $h=450\text{mm}$ .

### 3.5 Influence of the Finger-joint Model

The finger-joint model presented above uses a nonlinear fracture mechanics approach with two stochastic variables to characterize the finger-joint “material”. The strength and the failure elongation of the nonlinear spring elements were assumed to be uncorrelated.

In order to investigate the influence of this lack of correlation a model with the strength and failure elongation being fully correlated was tested. The full correlation means that instead of two stochastic variables (strength and failure elongation) only one stochastic variable has to be used (e.g. strength) and that the stiffness is always the same. However, if the strength is to be the only stochastic variable, there exists also the possibility of choosing the initial stiffness of the finger-joint to be fully correlated with the strength, which will lead to the failure elongation being always the same. Thereby we are left with two possibilities: “equal initial stiffness” or “equal failure elongation”. These two cases of models with only one stochastic variable are shown in Fig. 10. The previously used concept of two stochastic variables is shown together with two alternative models, equal stiffness and equal failure elongation.



Figure 10: Left: The model with two stochastic variables, Center: Equal stiffness, Right: Equal failure elongation

It turns out that the equal stiffness model results in a state of deformation which is very close to the one predicted by ordinary beam theory. Furthermore, since the failure of the beam is brittle and occurs at the instant of failure of the first nonlinear spring (weakest link failure), simple linear elastic beam theory analyses give the same results as the finite element simulations. If the input of the model in terms of strength of the nonlinear springs is assumed to be from a Weibull distribution, analytical solutions exist and no Monte-Carlo simulations have to be performed. For this case the present model coincides with the classic Weibull weakest link theory.

To compare the different models, a calibration of input data according to the method described earlier was performed. In an iterative manner the mean strength of the nonlinear springs was changed until the strength statistics of the 10 mm lamination was the same as previously reported (mean 55 MPa and COV 15%). For both models the strength was assumed to be log-normally distributed. The calibrated values of strength are  $\bar{f}_{i0} = 82\text{MPa}$  with  $\text{COV}=26\%$  for the equal stiffness model and  $\bar{f}_{i0} = 82\text{MPa}$  with  $\text{COV}=40\%$  for the equal failure elongation model. The bending strength statistics using the two models are summarized in Table 5. In the simulations using the equal stiffness model, ordinary beam theory was used.

Table 5: Bending and tensile strength statistics using models with one stochastic variable.

$h$ (mm)	$t$ (mm)	Equal stiffness			Equal failure elongation		
		Mean (MPa)	5% (MPa)	COV (%)	Mean (MPa)	5% (MPa)	COV (%)
135	45	57.5	43.5	14	61.0	49.6	11
450	45	50.5	40.0	12	55.3	46.9	9
900	45	48.4	38.8	12	53.4	46.1	8
10	10	55.3	41.4	15	54.7	42.3	15
33	33	47.8	37.7	12	51.2	43.7	9
45	45	46.1	36.8	12	50.3	43.2	8

## 4 Discussion

### 4.1 Bending and Tensile Strength

As expected, the beam bending strength is higher than the tensile strength of the lamination. As an example, the strength increase of the 45 mm lamination when contained in a 135 mm deep beam was found to be approximately 25% at the mean value level and 17% at the lower 5th percentile level, cf. Fig. 8. This strength increase is mainly due to the fact that the outer lamination is exposed to a non-uniform stress distribution, and that when evaluating the strength of the beam, the nominal stress at the outer edge is used as a reference. However, due to the stochastic nature of the strength distribution the actual failure position is not necessarily the outer tensile edge. So, instead of interpreting the results as a “strength increase” of the lamination, it is perhaps more natural to assume that the position of failure in the finger-joint changes if the beam depth is changed. The strength increase can then be expressed as an equivalent position of failure in the outer lamination. Here for simplicity this equivalent failure position,  $z$ , which is measured from the outer tensile edge, is calculated assuming ordinary beam theory to be valid:

$$z = \frac{h}{2} \left( \frac{f_m}{f_t} - 1 \right) \quad (3)$$

where  $f_m$  and  $f_t$  denote the bending strength of the beam and the tensile strength of a lamination, respectively, and  $h$  is the beam depth. For the case of a zero strength increase in bending, i.e.  $f_m = f_t$ , (3) states that the failure takes place at the outer tensile edge,  $z = 0$ .

For the case of the 45 mm thick lamination it is found, using (3) and the results from Fig. 8, that the failure positions are 9.8, 14.7 and 17.3 mm when the beam depth is 135, 450 and 900 mm respectively. This shows that the larger the beam depth, the closer a state of pure tension in the outer lamination is achieved, leading to the average failure position being equal to the mid-depth of the lamination, i.e. 22.5 mm for the present case. As mentioned in the introduction, a common assumption made in previous models is that this mid-depth is the characteristic point of failure initiation, independent of beam depth and lamination thickness.

## 4.2 Finger-joint Ductility

For the smaller values of the fracture energy, the failure of the finger-joint, and of the beam, is very brittle and occurs before the stress has reached zero in any spring. For these brittle failure cases it is the slope of the first descending part of the stress-elongation relation of the springs that determines the strength. Thus, for such cases a change in slope of the descending branch will have the same effect as a change of fracture energy. As an example, what has been presented here as a doubling of the fracture energy of the finger-joint is equivalent to halving the negative slope of the descending part of the stress-elongation curve. In the present modeling, a number of nonlinear springs across the lamination are used to model the behavior of a more complex geometry, cf. Fig. 2. Thus the fracture energy of the finger-joint relates to the cross sectional area of the lamination rather than to the actual bond line area of the finger-joint. Consequently, what has been presented here as a change of ductility of the finger-joint can also be interpreted as a change of finger-joint geometry, leading to a more or less ductile behavior.

## 4.3 Modeling Aspects

Being closely related to a fictitious crack model, the present finger-joint modeling approach includes the brittle failure at zero fracture energy and the perfectly plastic failure as special cases. Furthermore, as opposed to a linear elastic fracture mechanics approach, it is possible to use the present approach irrespective of the presence of stress gradients.

The two extreme cases of equal stiffness or equal failure elongation of the finger-joint nonlinear springs can be seen as special cases of the more complex model with two stochastic variables. Both the equal stiffness model and the model with two stochastic variables predict reasonable results in terms of size effects and laminating effects. The equal stiffness model, however, has only been tested for the case of an extremely brittle finger-joint where ordinary beam theory could be used for the simulation. For other cases FE simulations must be performed and there is no longer any need for a simplified material model.

The equal failure elongation model results in a larger loss of variability compared with the other models. The COV of the tensile strength of a lamination changed from 15% to 8% when the lamination thickness changed from 10 to 45 mm. As a result, the size effect in tension is very small and at the characteristic level even negative, i.e. a higher tensile strength for larger sizes.

## 5 Conclusions

The following conclusions can be drawn from the present study:

- The finger-joint model is general in the sense that it can be used for both locally brittle and ductile materials.
- The present finger-joint model predicts a size effect, a depth effect and laminating effects.

- The COV of the bending strength was of the same magnitude as for the finger-jointed lamination, but about 40–50% of the COV of the nonlinear springs.
- The characteristic position of failure initiation in an outer lamination of a beam depends on the beam depth.
- A simplified version of the present finger-joint model can be made to coincide with the classic Weibull theory.

## 6 Acknowledgements

The financial support by the Swedish Council for Building Research (BFR), which made this research possible, is gratefully acknowledged.

## Appendix I. References

- Aicher, S. and Klöck, W. (1990), “Spannungsberechnungen zur Optimierung von Keilzinkenprofilen für Brettschichtholz-Lamellen”. *Bauen mit Holz*. Karlsruhe, Germany, 92(5), pp. 356–362.
- Aicher, S. and Klöck, W. (1991), “Finger joint analysis and optimization by elastic, nonlinear and fracture mechanics finite element computations.” Proc. 1991 International timber engineering conference, TRADA, London, England. Vol. 3. pp. 3.66–3.76.
- Aicher, S. and Radovic, W. (1999), “Untersuchungen zum Einfluß der Keilzinkengeometrie auf die Zugfestigkeit keilgezinkter Brettschichtholz-Lamellen.” *Holz als Roh- und Werkstoff*. Berlin, Germany, (57) pp. 1–11.
- Colling, F. (1990). “Tragfähigkeit von Biegeträgern aus Brettschichtholz in Abhängigkeit von den festigkeitsrelevanten Einflußgrößen.” PhD thesis, University of Karlsruhe, Germany.
- Ehlbeck, J., Colling, F. and Görlacher, R. (1985). “Einfluß keilgezinkter lamellen auf die Biegefestigkeit von Brettschichtholzträgern. Entwicklung eines rechenmodells.” *Holz als Roh- und Werkstoff*. Berlin, Germany, (43) pp. 333–337.
- Falk, R. H., Solli, K. H. and Aasheim, E. (1992). “The performance of glued laminated beams manufactured from machine stress graded Norwegian spruce.” *Rep. no. 77*. Norwegian Institute of Wood Technology, Oslo, Norway.
- Faye, C., Lac, P., and Castéra, P. (1996). “Application of SFEM to the design of glued laminated timber beams.” Paper presented at the European Workshop on Application of Statistics and Probabilities in Wood Mechanics, LRBB, Bordeaux, France.
- Foschi, R. O., and Barrett, J. D. (1980). “Glued-Laminated Beam Strength: A Model.” *J. Struct. Div.*, ASCE, 106(8), 1735–1754.

- Gustafsson, P. J. (1985). "Fracture Mechanics Studies of Non-yielding Materials Like Concrete: Modelling of Tensile Fracture and Applied Strength Analyses." PhD thesis. *Report TVBM-1007*. Division of Building Materials, Lund Institute of Technology, Lund, Sweden.
- Hernandez, R., Bender, D. A., Richburg, B. A., and Kline, K. S. (1992). "Probabilistic modeling of glued-laminated timber beams." *Wood and fiber science*, 24(3), pp. 294-306.
- Hillerborg, A., Mod er, M. and Petersson, P-E. (1976). "Analysis of crack formation and crack growth in concrete by means of fracture mechanics and finite elements." *Cement and concrete research*. Oxford, England, 6(6) pp. 773-782.
- Leichti, R.J. (1988) "Structural finger joints under tensile loading modeled with finite elements and strength theory". Paper 2415, Forest research laboratory, Corvallis, Oregon.
- Milner, H. R. and Yeoh, E. (1991) "Finite element analysis of glued timber finger joints" *Journal of Structural Engineering*. ASCE, 117 (3) pp. 755-766.
- Nestic, R., Milner, H. R. and Stringer, G. R. (1994). "The evaluation of glued laminated timber strength from lamination tension tests." Paper presented at the IUFRO-S5.02/Timber Engineering meeting, Sydney, Australia.
- Pellicane, P.J. (1992) "A finite element to model thin inhomogeneities in solids" *Forest Products Journal*. 42(1), pp. 50-52.
- Pellicane, P.J. Gutkowski, R.M. and Jauslin, C. (1994) "Effect of glueline voids on the tensile strength of finger-jointed wood." *Forest Products Journal*. 44(6), pp. 61-64.
- Renaudin, P. (1997). "Approche probabiliste du comportement mecanique du bois de structure, prise en compte de la variabilite biologique." PhD thesis. Ecole Normale Superieure de Cachan, Paris, France.
- Schickhofer, G. (1996). "Development of efficient glued laminated timber." *Proc., CIB-W18, Meeting 29, Bordeaux, France*, International Council for Building Research Studies and Documentation, University of Karlsruhe, Germany, pp. 12.1.1-12.1.17
- Serrano, E. (1997). "Finger-joints for Laminated Beams. Experimental and numerical studies of mechanical behaviour." *Report TVSM-3021*, Lund University, Division of Structural Mechanics, Lund, Sweden. (<http://www.byggmek.lth.se>).
- Serrano, E. and Gustafsson, P. J. (1999). "Influence of bondline brittleness and defects on the strength of timber finger-joints." *International Journal of Adhesion and Adhesives*. Oxford, England, 19(1) pp. 9-17.
- Serrano, E. and Larsen, H. J. (1999). "Numerical investigations of the laminating effect in laminated beams." *Journal of Structural Engineering*. ASCE, 125 (7) pp. 740-745.
- Weibull, W. (1939). "A statistical theory of the strength of materials." *Nr. 151. Proc. Royal Swedish Institute for Engineering Research*. Stockholm, Sweden.

Wernersson, H. (1994). “Fracture characterization of wood adhesive bonds”. PhD thesis. *Report TVSM-1006*, Lund University, Division of Structural Mechanics, Lund, Sweden.

## Appendix II. Notation

The following symbols are used in the present paper:

$b$	=	beam width;
$E_x, E_y$	=	moduli of elasticity in grain and across grain direction;
$f_m$	=	beam bending strength;
$f_t$	=	tensile strength of lamination;
$f_{t0}$	=	tensile strength of nonlinear spring (stochastic model parameter);
$\bar{f}_{t0}$	=	mean tensile strength of nonlinear spring;
$G_f$	=	fracture energy;
$G_{xy}$	=	shear modulus;
$h$	=	beam depth;
$k_h$	=	depth factor;
$t$	=	lamination thickness;
$\beta$	=	power in size effect equation;
$\delta_0$	=	displacement at first breakpoint of a stress-elongation curve (stochastic model parameter); and
$\nu_{xy}$	=	Poisson’s ratio.





# *Paper V*

---

*Glued-in Rods for Timber Structures*  
– *A 3D Model and Finite Element Parameter Studies*  
by  
*Erik Serrano*

*Accepted for publication in Int. J. Adhesion and Adhesives*



# Glued-in Rods for Timber Structures

## – A 3D Model and Finite Element Parameter Studies

Erik Serrano

Division of Structural Mechanics, Lund University

*Accepted for publication in International Journal of Adhesion and Adhesives*

### Abstract

A nonlinear 3D finite element model and a theoretical parameter study in relation to glued-in rods for timber structures are presented. A strain-softening crack band model was used to characterise the behaviour of the adhesive layer between the rod and the wood. The model is general in the sense that it bridges the gap between the theory of an ideal plastic bondline and the theory of linear elastic fracture mechanics. Two parameter studies were made. One in relation to fracture energy and geometrical parameters and the second in relation to loading conditions. The results show that the fracture energy is of major importance for the pull-out load capacity, that the present model can be used to predict such phenomenon like the size effect and that the loading in pull-compression results in lower load-bearing capacities than the loading in pull-pull.

*Keywords:* Wood, Fracture mechanics, Finite element stress analysis, Stress distribution, Glued-in rod

## 1 Introduction

### 1.1 Background

Glued-in rods are used primarily for two purposes in timber engineering: either as a connector between structural elements or as a reinforcement of the wood in areas of high stresses perpendicular to the grain, such as around holes and notches and in the apex zone of curved and tapered beams. As connectors, glued-in rods have been used, especially for glued-laminated timber (glulam), for many years – in Europe mainly in the Nordic countries and in Germany. The glued-in rod connection makes it possible to obtain strong and stiff joints with excellent performance in load transfer without the disturbing appearance of the large metal plates often used for other connector types. Another advantage is the good fire resistance, since the connection is embedded in the insulating wood.

This paper reports some results from a part of a European research project, “GIROD–Glued-in Rods for Timber Structures” which has been running since 1998. The project aims at developing new design equation proposals for glued-in rods. The need for such design equations in the European codes was pointed out by Aicher and Herr in [1]. They showed that the present design *recommendation* to the annex of the European standard

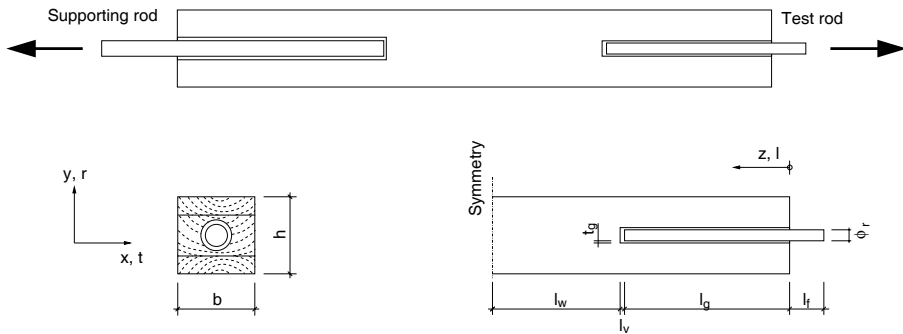


Figure 1: Schematic of test specimens and model used for simulations.

(EC5), ENV 1995-Part 2 Bridges, is questionable. The EC5-equation assumes that the nominal shear strength in the case of failure in the wood adjacent to the glue-line is independent of the glued-in length. Aicher and Herr [1] showed that on the basis of test data taken from the literature and from a new test series, the EC5-equation gives approximately two times higher design values of the pull-out load than the test results indicate. The tests were focused on long glued-in lengths with a 20 mm diameter threaded rod of 600 mm glued-in length.

In the GIROD project, the work is concentrated on the prediction of the pull-out strength of *axially* loaded glued-in rods. The rods used are threaded steel rods of different diameters and glued-in lengths, and rods of glass-fibre reinforced polyester. All rods are glued into glulam beams in holes with a diameter which is 1 mm larger than the nominal diameter of the rod. Three different adhesives are included in the project: a fibre reinforced phenol-resorcinol, a 2-component polyurethane and an epoxy. A schematic of the GIROD test specimens and the geometry of the model used for the numerical simulations in the present study are shown with some main notations in Figure 1. In the numerical model of the present study, it has been assumed that a symmetry plane exists at half the specimen length, since it is reasonable to assume that at some distance from the glued-in end of the testing rod, the wood is in a state of uniaxial tensile strain.

## 1.2 Previous Work

### 1.2.1 Experimental

The performance of glued-in rods in timber has been investigated experimentally by several researchers in the past. These investigations mainly concern glued-in bolts or reinforcement bars, glued into glulam. Threaded steel bolts were tested by Riberholt [2], by Ehlbeck and Siebert [3] and recently by Deng [4], Aicher and Herr [1], and Aicher et al. [5]. Tests on glued-in, ribbed, reinforcement bars were performed by Kangas [6] and Korin [7].

The adhesives used in these experimental investigations are epoxies, polyurethanes or resorcinol/phenolic adhesives. In [8], a large number of potential adhesives for glued-in rods are tested.

The results from all these investigations show that the average shear stress at failure is influenced by the glued-in length. Both Riberholt [9] and Kangas [6] derived design equations in which the effect of the glued-in length on the average shear stress at failure was taken into account. Riberholt, [9], proposes a design equation for the axial load capacity,  $P_u$ , for long glued-in lengths ( $> 200$  mm) according to:

$$P_u = k\rho\phi_r\sqrt{l_g} \quad (1)$$

where  $k$  is a material constant, different for different adhesives,  $\rho$  is the wood density,  $\phi_r$  is the rod diameter and finally  $l_g$  is the glued-in length. This equation was derived on a purely empirical basis by curve fitting of the experimental results. This result is typical for the design equations found in the literature with the pull-out load given by a nonlinear function of the material and geometrical parameters. The expression found in Eurocode 5 in contrast assumes a relation according to:

$$P_u = f_v\pi\phi_{equ}l_g \quad (2)$$

with  $f_v$  being the equivalent shear strength of the wood, which is given by:

$$f_v = 1.2 \cdot 10^{-3}\phi_{equ}^{-0.2}\rho^{1.5}, \quad \phi_{equ} = \min\{\phi_h, 1.25\phi_r\} \quad (3)$$

Here  $\phi_h$  is the hole diameter and  $\phi_r$  is the nominal diameter in the case of threaded rods. These diameters are used to obtain the equivalent diameter used in the expression,  $\phi_{equ}$ . These equations give as a result an average shear stress at failure that is slightly influenced by the diameter of the rod, not at all influenced by the glued-in length and finally very much influenced by the wood density. As stated in the introduction these relations seem to give non-conservative values for long glued-in lengths [1].

## 1.2.2 Analytical

Several theoretical bases could be used for the development of calculation models for the pull-out of glued-in rods, the most trivial one being the assumption of a uniform shear stress distribution along the entire rod. Such a model can be expected to work well for small glued-in lengths and ductile adhesives, but is not realistic for design purposes. The glued-in lengths used in practice will result in non-uniform stress distributions, [3, 10, 11, 12].

A linear elastic stress analysis using the traditional Volkersen assumptions [13], is one way to take into account the non-uniform stress distribution. However, since large stress gradients are common, the nonlinear, post-peak stress, behaviour of the bondline is essential and consequently a linear elastic stress analysis is of little use.

To take into account the large stress gradients, an approach based on the assumptions of linear elastic fracture mechanics (LEFM) can be used to develop a design equation. However, for LEFM to be applicable, the size of the fracture process region must be small in comparison to other dimensions of the structure. This is only true for very brittle adhesives or very large glued-in lengths.

A theory which includes the two extremes of a perfectly plastic behaviour and the brittle behaviour according to LEFM is the so-called generalised Volkersen theory, developed by Gustafsson [14]. Based on this theory, a rational expression for the pull-out

of a glued-in rod was derived by Johansson et al. [11]. The generalised Volkersen theory takes into account the fracture-softening capabilities of the bondline by introducing the fracture energy in the constitutive equations. Instead of using the linear elastic shear modulus of the adhesive layer, an equivalent stiffness defined in terms of the fracture energy and the bondline thickness is used. The expression for the ultimate pull-out load,  $P_u$ , reads:

$$P_u = \tau_f \phi_r \pi l_g \frac{(1 + \alpha) \sinh \beta}{\beta((\alpha + \cosh \beta) \cosh \beta - \sinh^2 \beta)} \quad (4)$$

$$\beta = \sqrt{\frac{1 + \alpha}{2}} \sqrt{\frac{l_g^2 \tau_f^2 \phi_r \pi}{(EA)_w G_f}}, \quad \alpha = \frac{(EA)_w}{(EA)_r} > 1 \quad (5)$$

where  $\tau_f$  is the shear strength of the adhesive layer,  $\phi_r$  is the rod diameter,  $l_g$  is the glued-in length and  $\alpha$  is the axial stiffness ratio of the adherends,  $(EA)_w/(EA)_r$ .  $E$  denotes the Young's moduli in the axial direction,  $A$  the respective cross-sectional areas and indices  $w$  and  $r$  denote wood and rod respectively.  $G_f$ , finally, is the fracture energy of the adhesive layer. A corresponding expression was also set up for the case of  $\alpha \leq 1$ . For small values of  $\beta$ , Eq. (4) coincides with the theory of a perfectly plastic bondline, i.e. the pull-out load is determined by the glued-in length and diameter of the rod, and the strength of the bondline. For large values of  $\beta$ , the pull-out load is determined by the fracture energy of the bondline, the stiffness of the adherends and the square root of the absolute size of the structure. The ratio of axial stiffnesses of the adherends,  $\alpha$ , depicts the stress distribution for given values of the other joint parameters. If  $\alpha$  equals unity, the joint has a balanced adherend stiffness combination and the stress distribution is as uniform as possible, leading to the highest possible ultimate load capacity.

Some further developments of this shear lag fracture model based on generalised Volkersen theory is given by Gustafsson and Serrano, [15]. In this work a refined model, which takes into account the shear flexibility of the wood adherend, is presented.

### 1.2.3 Numerical

An early example of using finite elements in the modelling of glued-in rods is the work by Müller and Roth [12]. They used a rather coarse FE-mesh to examine the linear elastic stress distribution and its dependence on some geometrical parameters. Later, larger models have been presented, e.g. by Aicher et al. in [10, 16], used for stress distribution analyses and heat transfer simulations. A somewhat more complex modelling approach was used by Guan [17], who used a built-in stress-based debonding feature of the FE-code combined with a contact algorithm to model the failure of the adhesive layer and the interaction between the failure surfaces. A nonlinear modelling with a bondline model tailor-made for wood adhesive bonds was presented by Johansson et al. in [11]. Here the strain-softening capabilities of the bondline was taken into account and the progressive failure of a glued-in rod was modelled. As in the other numerical studies, a two-dimensional, axisymmetric, model was used.

In evaluating the numerical results, some previous results from Gustafsson [14] relating to the use of a nonlinear fracture mechanics (NLFM) approach will be used. By the theory of NLFM is meant a theory based on a cohesive crack model, e.g. a fictitious crack model (FCM) or a crack band model (CBM), which can take into account strain softening and progressive crack growth.

From the one-dimensional theory of NLFM, a characteristic length,  $l_{ch}$ , of a material can be defined by:

$$l_{ch} = \frac{EG_f}{f_f^2} \quad (6)$$

where  $E$  is the stiffness,  $G_f$  the fracture energy and  $f_f$  the strength of the material. The characteristic length is a measure of the brittleness of the material and also a measure of the size of the fracture process zone. A brittleness ratio,  $\omega$ , of a structure can be defined in terms of its size normalised with respect to the characteristic length:

$$\omega = \frac{d}{l_{ch}} = \frac{df_f^2}{EG_f} \quad (7)$$

where  $d$  is a typical dimension of the structure. The brittleness ratio  $\omega$  defined by Eq. (7) has been used for parameter studies using a FCM, see e.g. [18]. It is now possible, [14], to express the load-bearing capacity in a dimensionless form if all geometrical and material properties are normalised. This means that in a parameter study, a change in material stiffness must be made proportional for all the materials in the model, the geometrical shape of the structure must not be changed and the nonlinear response of the strain softening material must have an unchanged normalised shape. This normalised shape can be defined in several ways and the definition used in the present study is described in the results section. Using normalised parameters, the load-bearing capacity of the structure in dimensionless form is given by a nonlinear function of  $\omega$  only:

$$\bar{\tau} = \mathcal{F}(\omega) \quad (8)$$

where  $\mathcal{F}$  denotes an unknown function. According to [14] there are bounds on  $\frac{d\mathcal{F}}{d\omega}$ :

$$-0.5 < \frac{d\mathcal{F}}{d\omega} < 0. \quad (9)$$

The bounds coincide with the linear elastic fracture mechanics theory for  $\frac{d\mathcal{F}}{d\omega} = -0.5$  and the theory of perfect plasticity for  $\frac{d\mathcal{F}}{d\omega} = 0$ . These bounds are useful for checking a numerical implementation of FCM-like models for the cases of extremely brittle or extremely ductile behaviour.

### 1.3 Failure Modes

All the previously mentioned investigations regard the failure of a glued-in rod as being determined by the pull-out of the rod, with a shear failure in the adhesive/rod interface, in the wood/adhesive interface or in the wood close to the bondline. However, if the edge distance is short, splitting failure of the wood will determine the strength of the connection. The splitting failure is caused by tensile stresses perpendicular to the wood grain. An early design proposal by Möhler and Hemmer [19] states that the minimum edge distance should be 4 times the nominal diameter of the rod. Riberholt [9] proposed the minimum edge distance to be 1.5–2.5 times the rod diameter if the adhesion to the rod is good and 2.5–4 times the diameter for the case of bad adhesion to the rod.

In the experimental investigation conducted by Deng [4], the splitting failure proved to be the dominating one. In this study however the edge distances were 1.5–2.25 times the diameter of the rod and the failure often located at the rod/adhesive interface.



## 1.4 Present study

The present paper presents a 3D nonlinear model developed for the prediction of the pull-out strength of glued-in rods. Results from a FE parameter study of factors affecting the strength of such rods are also presented. Two different parameter studies with somewhat different objectives are presented:

I influence of various geometry and material properties on the pull-out strength

II influence of the loading conditions on the pull-out strength

The results from the FE calculations in study I are compared with hand calculation formulas based on the classic theory of strength of materials, linear elastic fracture mechanics and the generalised Volkersen theory. The main aim of the present paper is to present a new approach in modelling the pull-out strength of glued-in rods and to indicate what factors might be of interest to include in future design equations. The material model has not yet been calibrated with test results. The aim is to calibrate the model using test results from small specimens with short glued-in lengths, and to predict the test results from large-scale axial pull-out tests. This procedure is part of the ongoing research in the GIROD project. However, some preliminary test results on large pull-out specimens have been published elsewhere, [5]. These results show that the average shear stress at failure does depend on the glued-in length. The average shear strengths obtained were in the range of 4-8 MPa for the three adhesives used (epoxy, 2-component polyurethane and a fibre reinforced phenolic resorcinol) and glued-in lengths (80-640 mm) and rod diameters (8-30 mm). These results are well within the capabilities of the present model.

## 2 Computational Model

### 2.1 General Remarks

All simulations have been performed with three-dimensional finite elements using the general purpose finite element code ABAQUS [20]. The model of a specimen consists of three materials: wood, bondline and steel. The wood and the steel parts are treated as linear elastic continua, while the bondline is modelled as a layer in which the shear stresses and the peel stress are nonlinear functions of the relative shear and normal displacements across the layer. The bondline model was implemented using an option of the FE-code allowing a user-defined material to be included in the analysis, [20]. The material model results in an unsymmetric tangential stiffness matrix of the equation system, so that the unsymmetric equation solver available in ABAQUS had to be used. This solver uses a standard Newton method to obtain an incremental solution [20].

The failure of the glued-in rod is assumed to take place within or in the vicinity of the adhesive layer. The input for the present bondline model is the stress-slip performance of the adhesive layer. It is assumed that such a stress-slip performance can be recorded for a small specimen in a stable pull-out test. A stable test is a test that includes the strain-softening branch of the stress-slip curve. It is then possible to calibrate the input data for the bondline model in such a way that the test results can be reproduced in a numerical finite element simulation. If the mode of failure for such a test is equal

Table 1: Adopted material parameters for the wood.

Young's modulus (MPa)	Shear modulus (MPa)	Poisson's ratio (-)
$E_T$ 500	$G_{TR}$ 60	$\nu_{TR}$ 0.3
$E_R$ 800	$G_{TL}$ 700	$\nu_{TL}$ 0.02
$E_L$ 14000	$G_{RL}$ 600	$\nu_{RL}$ 0.02

to the failure mode expected for structural-sized glued-in rods, the assumption is that the present modelling is accurate. In this sense the bondline model is a model for the adhesive itself as well as for the boundary layers on either side of it.

Steel rods used in timber connections are often threaded, but this threading is not modelled in detail in the present study. The effect of the threading is twofold: firstly it may give a different response of the bondline compared to a smooth rod of the same diameter and, secondly, it reduces the axial stiffness compared to a smooth non-threaded rod of the same diameter.

## 2.2 Material Modelling

### 2.2.1 Wood and Steel

The wood is modelled as being a linear elastic orthotropic material. The influence of taking into account the actual annual ring curvature of the timber, shown schematically in Figure 1, was investigated but it was found to have a negligible effect on the results, and therefore the material directions were assumed to be constant in the timber. The numerical values of the elastic parameters that have been used are given in Table 1 ( $T$  = tangential,  $R$  = radial and  $L$  = longitudinal direction (MPa))

The steel rods are modelled as being linear elastic and isotropic. The Young's modulus is set to 210 000 MPa and the Poisson's ratio  $\nu = 0.3$ .

### 2.2.2 Bondline Model

The strain-softening bondline model used is a further development of a model by Wernersson [21], and applied by Serrano and Gustafsson [22]. The original model was two-dimensional and developed for thin bondlines which were assumed to fail along a line of failure, involving only one shear-stress component and the peel stress of the bondline. An expansion of this model was made for the present study so that it now involves the two shear-stress components and the peel-stress component of an assumed plane of failure. Thereby the model can be used for adhesive layers in three-dimensional structures. For cases of axial pull-out with the wood fibres aligned parallel to the rod, the state of deformation could be approximated using an axisymmetric approach. However, for other loading conditions and for cases where the loading is not applied parallel to the wood fibres a full three-dimensional approach is necessary.

The behaviour of the bondline is defined by piecewise linear curves, describing the uniaxial behaviour for shear stress vs. shear slip (2 curves) and peel stress vs. normal displacement. Assuming a piecewise linear relation is the simplest way of obtaining a

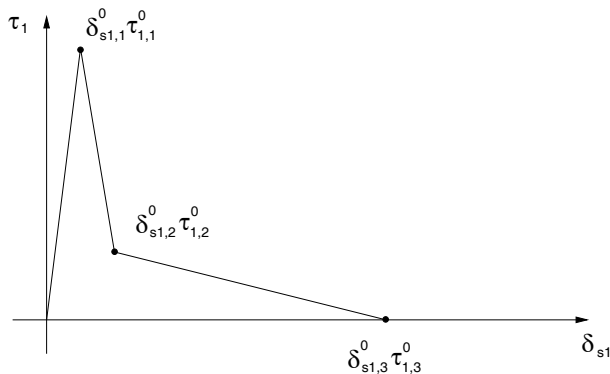


Figure 2: Stress-slip curve for a bondline in uniaxial shear.

good fit to experimental data, yet making it possible to fit complicated response curve shapes. In the present study piecewise linear relations with three segments are used. An example of such a piecewise linear curve is given in Figure 2.

The stress-strain relations in the bondline plane directions are assumed to be linear elastic. The three stress components in these directions (two normal and one shear stress) are not considered in the fracture model.

A general mixed-mode state of deformation of the bondline is given by two shear-slip deformations ( $\delta_{s1}, \delta_{s2}$ ) and by the normal deformation across the bondline ( $\delta_n$ ). The bondline response is assumed to retain its piecewise linear shape for radial deformation paths (constant ratio ( $\delta_{s1} : \delta_{s2} : \delta_n$ )), but vary smoothly with the degree of mixed mode, expressed by the mixed mode angles  $\varphi_{ss}$  and  $\varphi_{sn}$ :

$$\varphi_{ss} = \arctan \frac{\delta_{s1}}{\delta_{s2}} \quad (10)$$

$$\varphi_{sn} = \arctan \frac{\delta_s}{\delta_n} \quad (11)$$

$$\delta_s = \sqrt{\delta_{s1}^2 + \delta_{s2}^2} \quad (12)$$

The following criterion is used to determine whether the current state of deformation is elastic or not:

$$\left(\frac{\delta_{s1}}{\delta_{s1,1}^0}\right)^{m1} + \left(\frac{\delta_{s2}}{\delta_{s2,1}^0}\right)^{m2} + \left(\frac{\delta_n}{\delta_{n,1}^0}\right)^p \leq 1 \quad (13)$$

In Eq. (13)  $s1$  and  $s2$  correspond to the two directions in a plane of failure. Subscript  $n$  refers to the peel response, subscript 1 refers to the first breakpoint of the piecewise linear curve and finally, superscript 0 stands for the uniaxial properties.

If the current state is elastic, according to Eq. (13), the response is linear and uncoupled, according to the uniaxial responses. If not, the current state of mixed mode is calculated according to Eq. (10)–(11). Following this, the new deformations ( $\delta_{s1,i}$ ,  $\delta_{s2,i}$  and  $\delta_{n,i}$ ) corresponding to the breakpoints on the piecewise linear curve are calculated with an expression analogous to Eq. (13). The stresses corresponding to each such

breakpoint,  $i$ , are then calculated according to:

$$\tau_{1,i} = \tau_{1,i}^0 \cdot \frac{\delta_{s1,1}}{\delta_{s1,1}^0} \quad (14)$$

$$\tau_{2,i} = \tau_{2,i}^0 \cdot \frac{\delta_{s2,1}}{\delta_{s2,1}^0} \quad (15)$$

$$\sigma_i = \sigma_i^0 \cdot \frac{\delta_{n,1}}{\delta_{n,1}^0} \quad (16)$$

Knowing the stresses at the breakpoints, the stress for the current state of deformation can be obtained by linear interpolation. In FE-analysis, it is necessary not only to define the state of stress for the current state of deformation, but also to give the tangential stiffness of the material for this state, i.e. the derivative of the stress with respect to the strains. In the current implementation this is performed numerically, since for the present material model it is very difficult to obtain a general explicit equation for the derivative. The above model is concentrated on the severe state of simultaneously acting peel and shear stresses. For the case of a compressive stress perpendicular to the bondline, the shear stress-slip behaviour is assumed to coincide with the uniaxial response, and the normal stress-displacement behaviour is assumed to be linear elastic.

In the FE-implementation of the above model, a so-called crack band approach has been used. This means that the above stress-displacement relations are transformed into corresponding stress-strain relations by dividing the displacements by the thickness of the continuum finite element used to model the bond layer. This results in a material length being introduced as a material property apart from the uniaxial stress-strain relations and the powers  $m1$ ,  $m2$ ,  $p$  of Eq. (13).

In the present study it has been assumed that

$$m1 = m2 = p = 2. \quad (17)$$

The tri-linear stress-displacement relation is defined through

$$\tau_{1,2}^0 = \tau_{1,1}^0/3, \quad \tau_{1,3}^0 = 0. \quad (18)$$

Furthermore

$$\delta_{s1,2}^0 = 4\delta_{s1,1}^0, \quad \delta_{s1,3}^0 = 40\delta_{s1,1}^0. \quad (19)$$

The performance in the  $s2$ -direction was assumed to be the same as in the  $s1$ -direction. In the  $n$ -direction it was assumed that

$$\sigma_2^0 = \sigma_1^0/4, \quad \sigma_3^0 = 0. \quad (20)$$

It was further assumed that

$$\delta_{n,2} = 30\delta_{n,1}, \quad \delta_{n,3} = 180\delta_{n,1}. \quad (21)$$

The strengths in the three directions are given by

$$\tau_f = \tau_{1,1}^0 = \tau_{2,1}^0, \quad \sigma_f = \sigma_1^0 \quad (22)$$

which together with the relations

$$G_{f,s} = \int \tau_1^0 d\delta_{s1}^0 = \int \tau_2^0 d\delta_{s2}^0, \quad G_{f,n} = \int \sigma^0 d\delta_n^0 \quad (23)$$

define the bond layer properties for the given numerical values of only four parameters:  $\tau_f$  and  $\sigma_f$  for the strengths in shear and peel, and  $G_{f,s}$  and  $G_{f,n}$  for the corresponding fracture energies.

### 2.3 Load and Boundary Conditions

All loading was applied using displacement control in order to make it possible to trace possible post peak-load behaviour.

In all simulations, half the width of the specimen was analysed, implying symmetry at this section. Modelling half the width of the cross-section makes it possible to vary, for example, the material properties across the height. Otherwise, for the present case, with a square cross-section and material directions according to Figure 1, only 1/4 of the total cross-section would have to be considered.

In study I, the load was applied by “pull-pull”, Figure 3a. In study II, the load was also applied by “pull-compression”, Figure 3b. Here the face of the glulam in the vicinity of the rod was assumed to interact with a stiff loading plate, which in turn was prescribed to zero displacement. A contact algorithm available in the FE code was used to model the interaction between the wood and the loading plate, and the coefficient of friction was set to be 0.6.

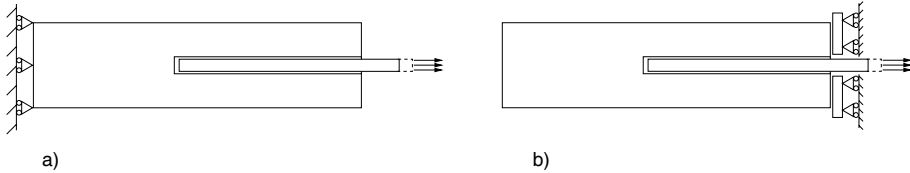


Figure 3: Loading of glued-in rod by a) “pull-pull” and b) “pull-compression”.

### 2.4 Finite Element Model

The element subdivision used for most calculations is shown in Figure 4. The model consists of approximately 14000 nodes and 12000 elements. The bondline is modelled with 50 elements in the axial direction and 12 elements in the circumferential direction. The elements representing the wood and the steel are standard isoparametric brick elements. The bondline was modelled using the same element type but with reduced integration (1 gausspoint) in order to avoid problems with the extreme slenderness ratio of the bondline elements.

For some of the calculations with extremely brittle adhesive properties, giving a small active fracture-process zone, the element subdivision along the rod was refined by increasing the number of elements from 50 to 100.

In order to check if the finite element subdivision in the plane of the cross-section was fine enough, a mesh consisting of approximately 65000 nodes (i.e. 195000 degrees of

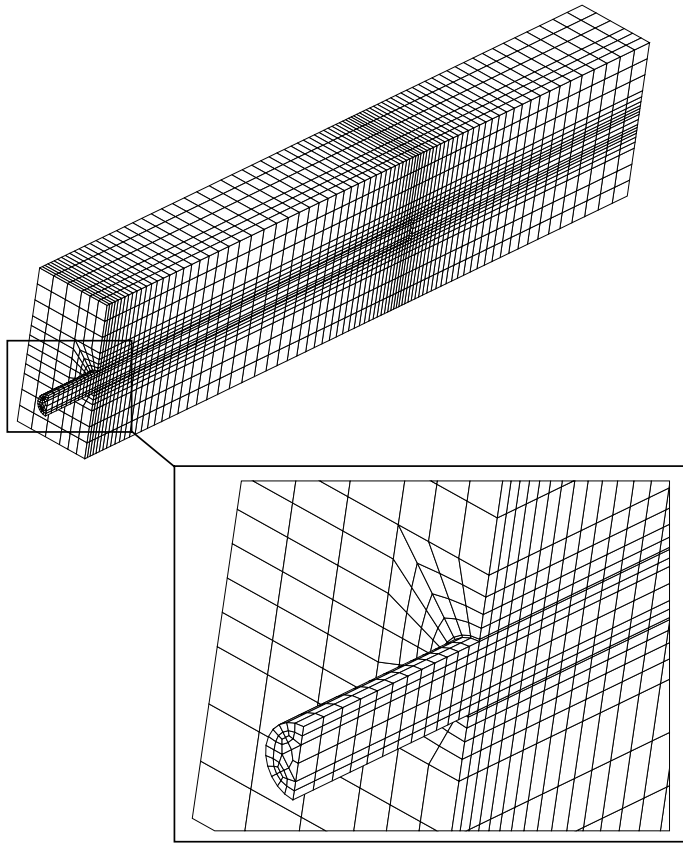


*Figure 4: The FE-mesh used in the parameter studies.*

freedom) was used in one calculation. The difference in calculated load-bearing capacity compared with the 14000 nodes model was less than 1%.

For the simulations in study II involving contact modelling, the FE-discretisation was slightly changed to better fit the different plate geometries studied.

## 3 Parameter Study I – Geometry and Material

### 3.1 Simulation Scheme

The different simulations performed are grouped into 6 different groups denoted A–F. Simulation A1 is the reference case, and each of the other groups involve simulations where parameters have been changed in relation to this case. The different groups of simulations involve:

- A: Variation of fracture energies,  $G_f$ , at a constant ratio  $G_{f,s}/G_{f,n} = 5$ , keeping the strength of the bondline and the shape of the stress-slip curves unchanged. The results obtained here also give information about the effect of a proportional change of  $\tau_f$  and  $\sigma_f$ , about the effect of a proportional change of all stiffness parameters of the wood and the steel, and about the effect of a *proportional* change of all geometrical dimensions (size effect), cf. Eq. (7).
- B: Variation of glued-in length  $l_g$  and length of wood  $l_w$  at a constant ratio  $l_g/l_w = 0.7$ , thus changing the slenderness ratio  $l_g/\phi_r$  of the rod. In total three slenderness ratios have thus been investigated, varying from 10 to 40. This range covers the most frequently used slenderness ratios.
- C: Variation of the rod diameter,  $\phi_r$ .
- D: Variation of the length of solid wood,  $l_w$ .
- E: Variation of the bondline strength. ( $\tau_f$  in simulations E1-E2 and  $\sigma_f$  in simulations E3-E4).
- F: Variation of cross-sectional dimensions,  $b$  and  $h$  at a constant ratio  $b/h = 1.0$ .

In the reference case, A1, the following numerical values of the geometry parameters were used, cf. Figure 1:  $\phi_r = 16$ ,  $t_g = 0.5$ ,  $l_g = 320$ ,  $l_w = 230$ ,  $l_v = 3$ ,  $b = 120$ ,  $h = 120$  (mm). The numerical values used for the material parameters in the bondline were:  $\tau_f = 12$ ,  $\sigma_f = 4$  (MPa),  $G_{f,s} = 2000$ ,  $G_{f,n} = 400$  (J/m<sup>2</sup>).

To obtain the input data necessary for the bondline model, tests on specimens with short glued-in lengths can be performed. A short glued-in length assures a more uniform stress distribution and makes it possible to estimate the local shear strength of the bondline. Also, a short glued-in length makes it possible to obtain the complete stress-slip relation of the bondline, including the descending, strain softening, part. This descending part of the stress-slip relation can be recorded provided that the tests are run under displacement control. With the complete stress-slip relation of the bondline it is possible to estimate the strength as well as the fracture energy. The fracture energy is equal to the area under the stress-slip curve. The numerical values used for the bondline are estimates based on such tests with short glued-in lengths from a preliminary study

on the behaviour of glued-in bolts [11] as well as from preliminary test results from the GIROD project. Also, results from tests on wood to wood adhesive bonds, [21], have been used in order to obtain realistic values of the bondline characteristics.

### 3.2 Results

The results from the simulations are summarised in Table 2. The table gives the changing input parameters in relation to the reference case and the results from the simulations in terms of the ultimate load,  $P_u$ , the mean shear stress at failure  $f_v = P_u/(\pi\phi_r l_g)$ , the normalised shear strength  $\bar{\tau} = f_v/\tau_f = P_u/(\pi\phi_r l_g \tau_f)$  and the mean tensile stress in the rod  $f_u = P_u/(\pi\phi_r^2/4)$ . The possible failure of the steel rod in the simulations involving high values of fracture energy has not been accounted for since these simulations were performed to illustrate the capabilities of the bondline model.

*Table 2: Ultimate load,  $P_u$ , and the corresponding average shear stress,  $f_v$ , normalised average shear stress,  $\bar{\tau}$ , and average tensile stress in the rod,  $f_u$ , are given. \* indicates that a refined FE-mesh was used.*

Name	Changing parameter and value	$P_u$ (kN)	$f_v$ (MPa)	$\bar{\tau}$ (-)	$f_u$ (MPa)
A1	Reference	83.8	5.21	0.434	417
A2*	0.125 $G_f$	33.6	2.09	0.174	167
A3*	0.25 $G_f$	45.8	2.85	0.237	228
A4*	0.5 $G_f$	65.9	4.09	0.341	327
A5	2 $G_f$	101.4	6.30	0.525	504
A6	4 $G_f$	121.4	7.55	0.629	604
A7	8 $G_f$	147.0	9.14	0.762	731
A8	16 $G_f$	171.6	10.7	0.889	853
A9	32 $G_f$	184.1	11.4	0.954	916
B1	0.5 $l_g$ , 0.5 $l_w$	54.9	6.83	0.569	273
B2*	2 $l_g$ , 2 $l_w$	99.2	3.08	0.257	493
C1	0.25 $\phi_r$	12.1	3.02	0.251	963
C2	0.5 $\phi_r$	33.0	4.10	0.342	657
C3	2 $\phi_r$	186.0	5.78	0.482	231
D1	0.25 $l_w$	84.4	5.24	0.437	420
D2	0.5 $l_w$	82.1	5.10	0.425	408
E1	0.5 $\tau_f$	60.7	3.78	0.629	302
E2*	2 $\tau_f$	97.2	6.04	0.252	483
E3	0.5 $\sigma_f$	83.7	5.21	0.434	416
E4	2 $\sigma_f$	84.5	5.25	0.438	420
F1	0.5 $b$ , 0.5 $h$	91.9	5.71	0.476	457
F2	2 $b$ , 2 $h$	81.8	5.08	0.424	407



Figure 5 shows the load-displacement response and Figure 6 shows the stress distributions along the bondline for the simulations A1, B1 and B2.

The stress distributions are given for the centroid of the bondline elements closest to the symmetry plane, but since the state of deformation in the bondline is almost axisymmetric, the shown distributions also apply, with negligible differences, for any other path along the rod. The stresses are given for two load levels of the tensile load, 5 kN and ultimate load. For all the cases, the 5 kN load level is within the linear elastic range. The plots are normalised with respect to the relative glue-line coordinates,  $z/l_g$  and the load is applied at the end closest to  $z/l_g = 0$ , cf. also Figure 1.

The linear elastic stress distributions reveal that tensile peel stresses develop at the end where the load is applied ( $z = 0$ ). For the simulations A1 and B2 the shear stress maximum also occurs at this end, while for simulation B1 it occurs at  $z = l_g$ . However, due to the tensile peel stresses, the fracture begins for all cases at  $z = 0$ . The stress distributions at ultimate load reveal that the bondline has started to soften at both ends for the simulations A1 and B1. For simulation B2 the bondline has started to soften only at  $z = 0$  at ultimate load.

Based on the above mentioned test results, the estimated bondline fracture energy in shear is in the range of 2–10 kJ/m<sup>2</sup> depending on the type of adhesive. In this range the series A simulations show that the fracture energy is a parameter with a major influence on the pull-out strength. A doubling of the fracture energy results in an approximately 20% higher load-bearing capacity.

The simulations in series B give the expected effect of glued-in length on the average shear strength,  $f_v$ . The longer the glued-in length, the more non-uniform the stress distribution, thus lower values of  $f_v$  are obtained. In addition to this size effect, which is predicted by the model, there exists a size effect due to variability in material parameters. Such Weibull-theory related size-effects are not investigated in the present study.

In simulations type C, the change of diameter of the rod also results in a different stress distribution. In the reference case, A1, the ratio of the axial stiffnesses,  $\alpha$ , is rather high, about 4.7. Increasing the rod diameter will result in a value of  $\alpha$  closer to unity and

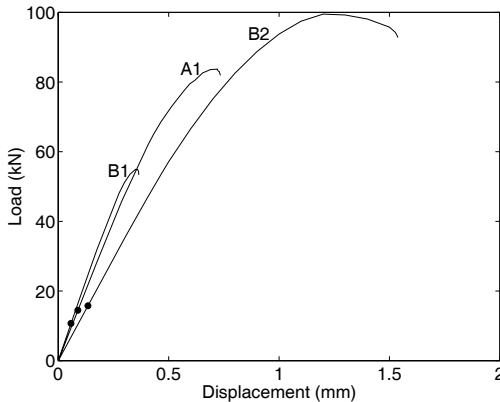


Figure 5: Load-displacement response from simulations A1, B1 and B2. The dots indicate the instance of fracture initiation.

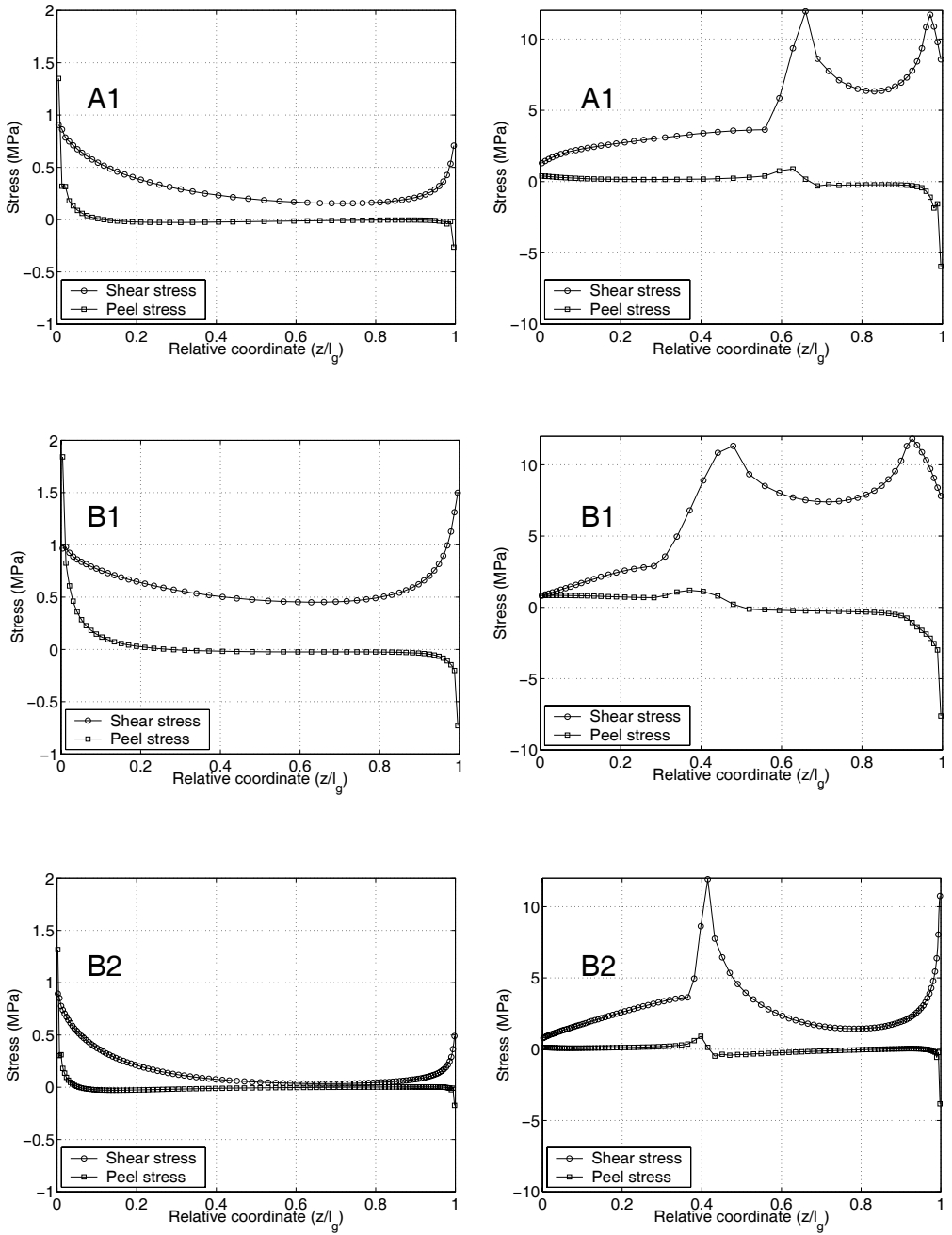


Figure 6: Linear elastic stress distributions at 5 kN global load (left) and stress distribution at ultimate load (right) for simulations A1, B1 and B2.  $z/l_g$  is defined in Figure 1.

consequently a more uniform stress distribution ( $\alpha = 1$  corresponds to a square wood cross-section of approximately 57 mm width and a rod of 16 mm diameter). A smaller rod diameter results in an increased value of  $\alpha$  and, consequently, a more non-uniform stress distribution, compared to the reference case.

The simulations of series D were performed to check that the distance  $l_w$  has been chosen large enough not to cause any boundary effects. This seems indeed to be the case.

In series E, the effect of performing a non-proportional change of the strength of the bondline in shear and in peeling was investigated. The results show that the dominating material strength is the shear strength of the bondline. The bondline model used assumes an interaction between shear stress and peel stress, reducing e.g. the shear strength if a tensile peel stress is applied, cf. Eq. (13). The linear elastic stress distributions include both peel stress and shear stress as shown in Figure 6. But after the fracture has occurred, the failure mode is dominated by pure shearing. Thus for the geometry of A1, the load level at which fracture begins is influenced strongly by the peel strength, but the ultimate load-bearing capacity is not affected to the same extent.

Series F, finally, shows the effect of changing the wood cross-section. The results can be explained in terms of axial stiffnesses and the stiffness ratio  $\alpha$ , in line with the discussion above. For the case F1, the reduced wood cross-section results in a stiffness ratio closer to unity ( $\alpha = 1.3$ ) as compared to the reference case ( $\alpha = 4.7$ ). For the case F2 the *larger* wood cross-section gives a value of  $\alpha = 22.8$ , and thus a more non-uniform stress distribution, compared to the reference case.

Now we turn again to the series A simulations using the dimensionless format previously discussed. The brittleness ratio,  $\omega$ , was defined in Eq. (7) and is now used with  $f_f = \tau_f, E = E_L, G_f = G_{f,s}, d = l_g$  to present the results from simulations A1–A9 in dimensionless form as  $\bar{\tau}$  vs.  $\omega$ . The normalised shape of the bondline response as discussed in relation with Eq. (8)–(9) is defined by  $\tau_{s1}/\tau_{f,s1}$  and  $\delta_{s1}/(G_f/\tau_{f,s1})$  for normalised stress and normalised deformation respectively. Figure 7 shows the results from simulations A1–A9 using this normalised format. Note that the normalised format gives information about the effect of *proportional* changes in e.g. geometry. This means that the shape of the structure is unchanged and that the effect of e.g. changing the glued-in length only can not be evaluated using Figure 7. Figure 7 also illustrates the strength as predicted by the theory of perfect plasticity ( $\bar{\tau} =$  constant = 1.0, and by the theory of linear elastic fracture mechanics  $\bar{\tau} = C \cdot \omega^{-0.5}$ , where  $C$  is a geometry (shape) constant and, finally, the strength predicted by Eq. (4). For the present case the following expressions apply, assuming that the thin bondline acts in pure shear and that the adherends act in pure tension:

$$P_{u,pl} = \tau_f l_g \pi \phi_f \quad (24)$$

$$P_{u,LEFM} = \sqrt{2 \overline{EA} G_{f,s} \pi \phi_f} \quad (25)$$

$$\overline{EA} = \left( \frac{1}{E_r A_r} - \frac{1}{E_w A_w + E_r A_r} \right)^{-1} \quad (26)$$

where indices *pl* and *LEFM* denote plasticity theory and linear elastic fracture mechanics respectively and  $\phi_f$  is the diameter of the assumed cylindrical failure surface and, possibly,  $\phi_f$  depends on the bondline thickness,  $t_g$ . The indices *r* and *w* denote rod and wood and  $EA$  denotes the axial stiffness. The wood area  $A_w$  is the net area,

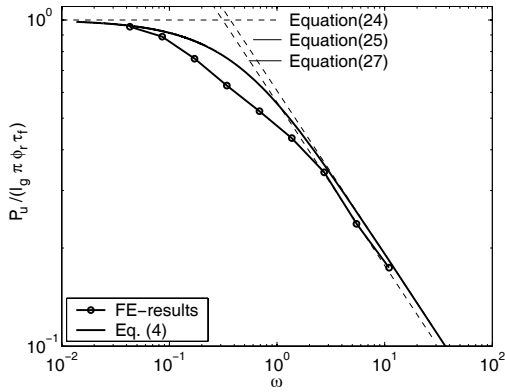


Figure 7:  $\bar{\tau}$  vs.  $\omega$  for simulations A1-A9. Note the logarithmic scales.

$A_w = b \cdot h - (\pi \cdot \phi_h^2/4)$ , for a rectangular cross-section with  $\phi_h$  being the hole diameter. If the bondline thickness is assumed to be small in relation to the other dimensions and the failure is assumed to take place along the curved surface defined by the rod diameter then  $\phi_r = \phi_h = \phi_f = \phi$ .

In general however, i.e. for the cases when the bondline thickness is not small, there will be an influence of the bondline thickness on the pull-out strength. Assuming that a crack propagates from the free end of the rod, Eq. (25) can easily be derived using an energy release rate approach, see any standard textbook on fracture mechanics, e.g. [23].

If  $E_w A_w \gg E_r A_r$  Eq. (26) results in  $\overline{EA} = E_r A_r$ , so that Eq. (25) can be rewritten:

$$P_u = \sqrt{2 E_r A_r G_{f,s} \pi \phi} \quad (27)$$

where it was assumed that  $\phi_r = \phi_h = \phi_f = \phi$ . In terms of nominal shear strength this yields:

$$f_v = P_u / (\pi \phi l_g) = k \lambda^{-0.5} l_g^{-0.5} \quad (28)$$

with  $k$  being a material constant  $k = \sqrt{0.5 E_r G_{f,s}}$  and  $\lambda$  denoting the slenderness ratio  $\lambda = l_g / \phi$ . As expected, and as is shown in Figure 7, the FE-results coincide with the analytical expressions of Eqs. (24), (25) and (27) for the cases of extremely ductile and extremely brittle behaviour. In the transition region, however, there is a difference and here the generalised Volkersen theory, Eq. (4), predicts results closer to the numerical results. The difference between Eq. (4) and the FE-results can be explained by the fact that Eq. (4) assumes the bondline to behave in a linear elastic manner. Furthermore Eq. (4) assumes a one-dimensional state of stress (pure shear) in the bondline and an axisymmetric geometry and loading. Since for the extreme values of  $\omega$ , the FE-simulations and the analytical results coincide, the assumptions of a one-dimensional stress-state and axisymmetry do not seem to influence the results for the present geometry. For larger timber cross sections, however, the use of an analytical expression assuming axisymmetry, would probably have to involve some kind of effective wood cross-section.

## 4 Parameter Study II–Loading Conditions

### 4.1 Scheme

In this study, the influence of applying the load by pull-compression versus loading by pull-pull was studied for a number of different glued-in lengths and fracture energy values. The effect of using plates of different sizes and shapes was investigated: a 120 mm square plate, a 100 mm diameter circular plate and a 40 mm circular plate. There was a hole for the rod in the plates. For all cases, this hole had a diameter equal to the hole in the wood plus 1 mm, i.e.  $16+0.5+0.5+1.0=18$  mm. For most of the simulations in this study, the finite element discretisation used was essentially the same as the one reported previously. In order to check that this was appropriate for the contact modelling, a finer element mesh with more nodes and elements at the contact surfaces was also tested. In addition to giving results regarding the effect of load application, this study also gives some additional information about the effect of rod length and fracture energy. The various loading conditions were applied for two glued-in lengths (160 and 320 mm) and for three different values of  $G_{f,s1}$  (1, 2 and 4 kJ/m<sup>2</sup>). As in the previous studies, it was assumed that  $G_{f,s2} = G_{f,s1}$  and that  $G_{f,n} = 0.2G_{f,s1}$ . All other geometry and material parameters were according to simulation A1.

### 4.2 Results

The results from the simulations in terms of pull-out strengths are summarised in Table 3. Some of the parameter combinations used in this study coincide with those of study I, but the results are repeated here for the purpose of completeness. The general outcome of this parameter study is that the pull-compression case, as expected, always gives lower load-bearing capacity than the pull-pull case. This is because the pull-compression case results in a more non-uniform shear stress distribution than the pull-pull case. The capacity is approximately 10–20% lower in pull-compression for the case with the square plate and the large circular plate. For the small circular plate the load-bearing capacity is reduced by approximately another 10%. The reduction in capacity is more severe for the more brittle cases, i.e. the longer glued in lengths and lower fracture energies.

Table 3: Ultimate load,  $P_u$ , for various combinations of loading and fracture energy values,  $G_{f,s}$ , and glued-in lengths,  $l_g$ . \* indicates that a refined FE-mesh was used.

Loading type	Plate type	$G_{f,s}$ (N/m <sup>2</sup> )	$l_g$ (mm)	$P_u$ (kN)
pull-comp.	□120	2000	320	73.3
pull-pull	-	2000	320	83.8
pull-comp.	ϕ100	2000	320	72.9
pull-comp.	□120	2000	160	50.3
pull-pull	-	2000	160	54.9
pull-comp.	□120	4000	320	90.9
pull-pull	-	4000	320	101.4
pull-comp.	□120	4000	160	60.8
pull-pull	-	4000	160	66.8
pull-comp.	□120	1000	320	53.4
pull-pull	-	1000	320	65.9
pull-comp.	□120	1000	160	41.3
pull-pull	-	1000	160	45.2
pull-comp.*	□120	2000	320	73.5
pull-comp.*	ϕ100	2000	320	72.7
pull-comp.*	ϕ40	2000	320	67.3

## 5 Conclusions

The following conclusions can be drawn from the present study:

- A nonlinear, 3-dimensional bondline model to simulate the behaviour of glued-in rods for timber structures by finite element analysis was developed.
- The model was tested for a wide range of material and geometrical properties and it was found that it reproduces the results according to the theory of perfect plasticity and the theory of linear elastic fracture mechanics. It can also be used for situations falling in between these two extremes.
- The model predicts the fracture energy of the adhesive layer to be an important parameter for the prediction of the ultimate load of glued-in rods.
- The model predicts effects of both absolute size as well as of glued-in length on the nominal shear strength of glued-in rods, a phenomenon known from the test results of several independent studies.
- Loading the glued-in rod in pull-compression reduced the ultimate load by 10–20% compared with loading in pull-pull.

## 6 Acknowledgements

The GIROD project involves the following research institutes: SP – Swedish National Testing and Research Institute, FMPA Otto-Graf Institute (Germany), University of Karlsruhe (Germany) and TRADA Technology (UK) and Lund University. The financial support through grant no. SMT4-CT97-2199 by the European Commission (DG XII) and the co-operation from the partners involved in this research project are gratefully acknowledged. This research was also in part financially supported by the Swedish Council for Building Research (BFR), project no. 19960633. This support is also gratefully acknowledged.

## References

- [1] Aicher, S. and Herr J. *Bonded glulam-steel rod connections with long anchorage length*. Otto-Graf Journal Vol. 8. Forschungs und Materialprüfungsanstalt Baden-Württemberg. Stuttgart, Germany 1997.
- [2] Riberholt, H. *Glued bolts in glulam*. Report R210, Department of Structural Engineering, Technical University of Denmark, Lyngby, Denmark 1986.
- [3] Ehlbeck, J. and Siebert, W. *Praktikable Einleimmethode und Wirkungsweisen von eingeleimten Gewindestangen unter Axialbelastung bei Übertragung von grossen Kräften und bei Aufnahme von Querzugkräften in Biegeträgern. Teil 1: Einleimmethode/Messverfahren/Haftspannungsverlauf*. Forschungsbericht: Versuchsanstalt für Stahl, Holz und Steine, Abteilung Ingenieurholzbau, Universität Karlsruhe, Germany 1987.
- [4] Deng, J.X. *Strength of Epoxy Bonded Steel Connections in Glue Laminated Timber*. PhD-thesis. Civil engineering research report 97/4. Dept. of Civil Engineering, University of Canterbury, Christchurch, New Zealand 1997.
- [5] Aicher, S., Gustafsson, P. J. and Wolf, M. *Load displacement and bond strength of glued-in rods in timber influenced by adhesive, wood density, rod slenderness and diameter*. In Proceedings 1<sup>st</sup> RILEM Symposium on timber engineering, Stockholm. Ed. L. Boström. pp. 369–378. RILEM Publications S.A.R.L. Cachan, France 1999.
- [6] Kangas, J. *Joints of glulam structures based on glued-in ribbed steel rods*. VTT Publications 196. Technical research centre of Finland. Espoo, Finland 1994.
- [7] Korin, U. *Development of Embedding Loads of Rebars in GLULAM*. Proceedings of the 1997 Conference of IUFRO S5.02 Timber Engineering. Copenhagen, Denmark 1997.
- [8] Kemmsies, M. *Comparison of Pull-out Strengths of 12 Adhesives for Glued-in Rods for Timber Structures*. SP REPORT 1999:20. SP Swedish National Testing and Research Institute, Building Technology. Borås, Sweden 1999.
- [9] Riberholt, H. *Glued bolts in glulam – Proposal for CIB Code*. Proceedings CIB-W18/21-7-2. Meeting twenty-one. Parksville, Canada 1988.
- [10] Aicher, S., Höfflin, L. and Wolf, M. *Influence of specimen geometry on stress distribution in pull-out tests of glued-in steel rods in wood*. Otto-Graf Journal Vol. 9. Forschungs und Materialprüfungsanstalt Baden-Württemberg. Stuttgart, Germany 1998.
- [11] Johansson, C-J., Serrano, E., Gustafsson, P.J. and Enquist, B. *Axial strength of glued-in bolts. Calculation model based on non-linear fracture mechanics - A preliminary study*. Proceedings CIB-W18. Meeting twenty-eight. Copenhagen, Denmark 1995.



- [12] Müller, J. and von Roth, W. *Untersuchungen zum Tragverhalten zur Faser in Nadelholz eingeleimte Stäben aus unterschiedlichen Materialien*. Holz als Roh und Werkstoff 1991;(49):85–90.
- [13] Volkersen, O., *Die Nietkraftverteilung in Zugbeanspruchten Nietverbindungen mit Konstanten Laschenquerschnitten*. Luftfahrtforschung, 1938;(15):41–47.
- [14] Gustafsson, P. J. *Analysis of generalized Volkersen-joints in terms of non-linear fracture mechanics*. In: Mechanical Behaviour of Adhesive Joints, pp. 323–338. Edition Pluralis, Paris, France 1987.
- [15] Gustafsson, P. J. Predicting the Pull-out Strength of Glued-in Rods. Proceedings 6<sup>th</sup> World Conference on Timber Engineering, Vol. 1 pp. 7.4.4-1–7.4.4-8. Department of Wood Science, University of British Columbia, B.C., Canada, 2000.
- [16] Aicher, S., Wolf, M. and Dill-Langer, G. *Heat flow in a glulam joist with a glued-in steel rod subjected to variable ambient temperature*. Otto-Graf Journal Vol. 9. Forschungs und Materialprüfungsanstalt Baden-Württemberg. Stuttgart, Germany 1998.
- [17] Guan, Z. W. *Structural behaviour of glued bolt joints using FRP*. Proceedings 5<sup>th</sup> World Conference on Timber Engineering, Vol. 1, pp. 265–272. Presses polytechniques et universitaires romandes, Lausanne, Switzerland 1998.
- [18] Gustafsson, P. J. *Fracture mechanics studies of non-yielding materials like concrete: modelling of tensile fracture and applied strength analyses*. Report TVBM-1007, Lund Institute of Technology, Division of Building Materials, Lund, Sweden, 1985.
- [19] Möhler, K. and Hemmer, K. *Eingeleimten Gewindestangen*. Bauen mit Holz 1981;83(5):296–98.
- [20] Hibbitt, Karlsson & Sorensen, Inc. *ABAQUS, Version 5.7*. Pawtucket, RI, USA 1997.
- [21] Wernersson, H. *Fracture characterization of wood adhesive joints*. Report TVSM-1006, Lund University, Division of Structural Mechanics 1994.
- [22] Serrano, E. and Gustafsson, P. J. *Influence of bondline brittleness and defects on the strength of timber finger-joints*. Int J Adhesion and Adhesives. 1999;19(1):9–17.
- [23] Hellan, K. *Introduction to fracture mechanics* McGraw-Hill Book Co. Singapore 1985.

# Appendix

Notations and symbols are explained in the text where they first appear. A list of main notations used is given below.

$( )_L$	property related to the longitudinal direction of wood
$( )_R$	property related to the radial direction of wood
$( )_T$	property related to the tangential direction of wood
$( )_n$	peel direction in bondline
$( )_r$	property related to the rod material
$( )_s$	shear direction in bondline
$( )_w$	property related to the wood material
$A$	cross-sectional area
$C$	geometry constant
$E$	modulus of elasticity
$G$	shear modulus
$G_f$	fracture energy
$P_u$	ultimate load
$b$	beam width
$d$	typical size of structure
$f_u$	average tensile stress in rod at pull-out failure
$f_v$	average shear stress at pull-out failure
$f_f$	strength of material
$h$	beam depth
$k$	material constant in design formulae
$l_{ch}$	characteristic material length
$l_g$	glued-in length
$l_w$	length of solid wood in test specimen
$m1, m2, p$	powers used in interaction equation of material model
$t_g$	bondline thickness
$z$	coordinate along axial direction of the glued-in rod
$\alpha$	adherend axial stiffness ratio
$\beta$	brittleness ratio of joint in generalised Volkersen theory
$\delta$	slip across bondline
$\nu$	Poisson's ratio
$\rho$	density
$\sigma_f$	bondline peel strength
$\bar{\tau}$	normalised, average shear stress at pull-out failure
$\tau_f$	shear strength of bondline
$\phi_f$	diameter of failure surface
$\phi_h$	diameter of hole
$\phi_r$	diameter of rod
$\varphi$	mixed mode angle
$\omega$	brittleness ratio of joint




# *Paper VI*

---

*Glued-in Rods for Timber Structures*  
– *An Experimental Study of Softening Behaviour*  
by  
*Erik Serrano*

*Submitted for publication in Materials and Structures*





# Glued-in Rods for Timber Structures

## – An Experimental Study of Softening Behaviour

Erik Serrano

Division of Structural Mechanics, Lund University

*Submitted for publication in Materials and Structures*

### Abstract

A test method to obtain the strength and the fracture characteristics of the bond of glued-in rods for timber structures is presented. Test results from a series of tests using the proposed method are also given. The test method makes it possible to record the complete stress-displacement response of small test specimens. This response includes the softening behaviour after peak stress, i.e. the decreasing stress at increasing deformation. The test series include three adhesives, two rod materials, four load-to-grain angles and two timber qualities with different densities. A method to evaluate the fracture-softening behaviour is also proposed. The fracture softening is evaluated by using only a part of the stress-displacement curve. The part used in the evaluation is determined in terms of the slope of the descending part of the stress-displacement curve.

## 1 Introduction

### 1.1 Background

Glued-in rods are used in timber engineering to join beams and columns. The rods used are often threaded steel rods or ribbed reinforcement bars. The glued-in rod connection results in stiff and strong joints, which can be used, e.g. for frame corners and column foundations. Glued-in rods have also been used to reinforce timber elements in areas of high stresses perpendicular to the grain such as in curved or tapered beams or at notches. Although glued-in rods have been used for several years, there is no current normative standard in the European timber code, EC5. The present paper presents a part of an ongoing European research programme, “Glued-in Rods for Timber Structures – GIROD”, aiming at developing such code proposals. The paper describes a test method to obtain the strength and the fracture characteristics of the bond of glued-in rods. Test results from using the proposed method are also presented. The fracture characteristics are recorded as the complete stress-displacement response of small test specimens. This response includes the softening behaviour after peak stress, i.e. the decreasing stress at increasing deformation.

## 1.2 Previous Work

Previous experimental work on glued-in rods for timber has mainly concerned the testing of structural-sized specimens and the results have been used to obtain empirical design equations. Examples of such experimental programmes are Riberholt [1], Ehlbeck [2], Kangas [3], Deng [4] and Aicher et al. [5]. Although testing on structural-sized specimens is necessary for the verification and calibration of theoretical models, such testing is usually not practicable for obtaining material-property parameters, e.g. parameters that define the local strength and fracture properties of the bond.

Tests on wood and wood-adhesive bonds to obtain fracture characteristics in terms of the fracture-softening behaviour have been performed e.g. by Boström [6] and Wernersson [7]. Boström reports on a test method for small, notched, wood specimens in tension (mode I) and in shear (mode II), to obtain their complete stress-displacement response, including the descending, strain-softening part. Using a similar technique, Wernersson performed tests on wood-adhesive bonds in mode I, II and in mixed modes.

In a preliminary study on glued-in rods by Johansson et al. [8], a test series on small glued-in rod specimens was presented. The method used in the present study is a further development and simplification of this, partly based on the experiences gained in that preliminary study.

## 1.3 Present Study

### 1.3.1 Aim

The present study concerns an experimental method to obtain the fracture characteristics of glued-in rods for timber structures. These characteristics involve the local strength of the adhesive bond, its fracture energy or critical energy release rate, and its strain-softening behaviour. The main aim is to record the local shear-stress versus shear-slip relation, and from this evaluate parameters for the strength, fracture energy and fracture softening. These material data are needed as input for theoretical material models used in numerical finite element simulations. Such numerical simulations can be used to calibrate rational hand-calculation models, which in turn can constitute the basis of future design equations.

### 1.3.2 Experimental Programme

The experimental programme involves testing of rods glued with three different adhesives: a fibre-reinforced phenol-resorcinol (PRF), a 2-component polyurethane (PUR) and an epoxy (EPX). These tests are performed with threaded steel rods (M16), glued parallel to the grain in pieces of wood cut from glulam beams of two different qualities. The EPX is also tested for various load-to-grain angles for one of the timber qualities and, finally, a series of tests is performed on a glass-fibre reinforced polyester (FRP) rod, again using the EPX. For each kind of specimen five nominally equal samples were tested.

## 2 Materials and Methods

### 2.1 General Remarks

In testing for mechanical properties, e.g. of an adhesive bond line, two markedly different approaches in sample preparation can be used: a) cut out a small, representative test specimen of appropriate size and shape from the structure to be analysed, or b) prepare a small test specimen of the size required in the test.

These two approaches have their respective advantages and disadvantages. The first approach is appealing because a test specimen is cut from a structure manufactured in the same way as it would be in practice. For the present application this approach would mean that a structural-sized rod is glued into a timber beam which is then cut (sliced) into pieces of appropriate size. If this approach is used, the curing of the adhesive will take place under circumstances similar to those used in practice. The test specimen is thus a representative sample of a structural-sized glued-in rod. The major drawback of this method is that the cutting of the rod might damage the specimen. Another drawback, is that the sample preparation, i.e. the cutting of the specimens, can be somewhat difficult to perform since it requires special sawing facilities.

The second approach is a more standard approach, at least for pure mechanical testing of materials. In the present context this approach means that a rod of short length is glued into a small piece of wood. Producing a specimen using this approach, the question arises whether the gluing and curing conditions of the adhesive are the same as for structural-sized rods. It is difficult, using a short glued-in length, to ensure a high pressure in the bondline during curing. This means that boundary effects during curing might have an impact on the strength of the bondline. One example of such boundary effects, related to the use of PUR-adhesive, is the forming of CO<sub>2</sub>-bubbles, which can become intense at free surfaces of the adhesive (foaming).

### 2.2 Materials and Climate Conditions

Three adhesives and two rod materials, as described above, were tested. All samples were prepared using pieces of wood cut from spruce glulam beams of two different strength classes, C35 and C24. The glulam beams were stored for several months in standard climate, 20°C, 65%RH, before sample preparation. The gluing and curing as well as the storing of the finished specimens also took place in this climate. All specimens were cured for at least seven days prior to testing.

The density and the moisture content of the wood were determined by cutting out small pieces close to the bondline and then weighing the pieces in air and under water. The specimens were subsequently dried at 105°C for 24 hours and again weighed. The density values reported are calculated as (dry mass)/(volume at 20°C, 65%RH)

### 2.3 Sample Preparation

Both the above methods of producing test specimens were investigated in a series of pre-tests, not reported here. The conclusion was that the second method, i.e. the gluing of small specimens, was the most reliable one, and therefore, this method was used in the main test series, reported here.



Glulam beams with a 120 mm square cross section were split into four pieces of  $48 \times 48 \text{ mm}^2$ . Each such piece was then cut to a thickness of 40 mm. In each piece, a hole of a diameter  $\phi=17 \text{ mm}$ , was drilled through the entire piece. From a threaded steel rod (M16), strength class 8.8, 90 mm long pieces were cut and further machined in a lathe, leaving a threaded length of 8 mm. Fig. 1 shows how the wood pieces were cut from the beams. After drilling, the holes were partially filled from one end with Tack-It, which is a kind of synthetic clay used to fix posters etc. An 8.5 mm deep hole was left, at the bottom of which a circular, 0.5 mm thick, Teflon film was put, leaving an 8 mm deep hole for the threaded rod to be glued into.

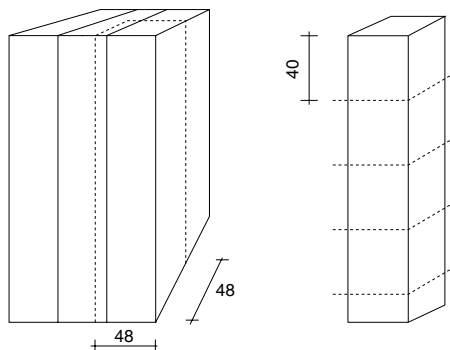


*Fig. 1. - The specimens were cut from glulam beams.*

Adhesive was poured into the holes and the rods placed in the holes. To ensure a good filling out of the grooves of the threads, glue was also spread on the thread of the bolts. A fixing device was used to ensure that the bolts were glued in and fixed in the desired direction during curing. In order to ensure a centrally placed bolt in the drilled hole, three metal clips were pressed into the synthetic clay so that the bolt was securely fixed at the centre of the hole. After curing of the adhesive the synthetic clay and the Teflon film were removed.

The same principle for sample preparation was used for the tests performed on the FRP rod. The 16 mm diameter rods were cut into 90 mm long pieces and were then machined to 12 mm diameter except for the 8 mm at one end. The FRP rods have a smooth surface and to improve the adhesion of the glue, they were lightly sanded by hand and then wiped clean using a cloth soaked with alcohol.

Three additional load-to-grain angles were tested:  $22.5^\circ$ ,  $45^\circ$  and  $90^\circ$  respectively. Each specimen was cut out so that the bond would consist of wood from only one lamination. This means that the  $90^\circ$  specimens, for instance, were cut almost in the radial direction of the wood, cf. Fig. 2.

## 2.4 Test Set-ups and Testing Conditions

All tests were performed using displacement control to make possible a recording of the softening behaviour of the bondline. Several pre-tests were performed to find a suitable rate of displacement, so that the peak load could be obtained within a few minutes and the total time to failure would be about 10–15 minutes.

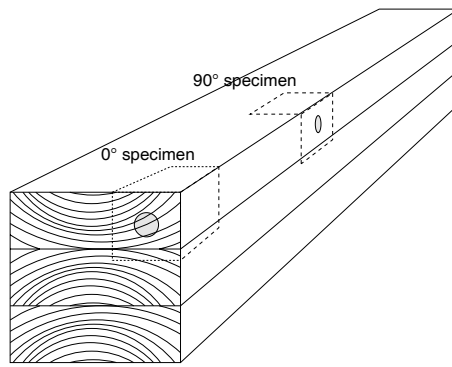


*Fig. 2. - Specimen cutout for two load-to-grain angles.*

The test specimens were placed on a self-aligning plate, which in turn was mounted into the lower hydraulic grips of the testing machine. The self-aligning plate was used in order to achieve a more uniform stress distribution at the contact surface. The specimen and the set-up is shown in Fig. 3.

The initial speed of the hydraulic actuator was 0.003 mm/s (cross-head speed). After a 40% load drop after peak load, the speed was gradually increased, and the final speed was 0.03 mm/s. In addition to the original plan, including five nominally equal tests for each material combination, a decision was made to investigate the characteristics at unloading after peak stress for one specimen. Here, unloading means decreasing deformation. The unloading sequence of these tests was automatically initiated by the software of the test system. The unloading was set to take place after a 20% load drop. After the unloading down to zero load, a new loading sequence was run until complete failure of the specimen was achieved.

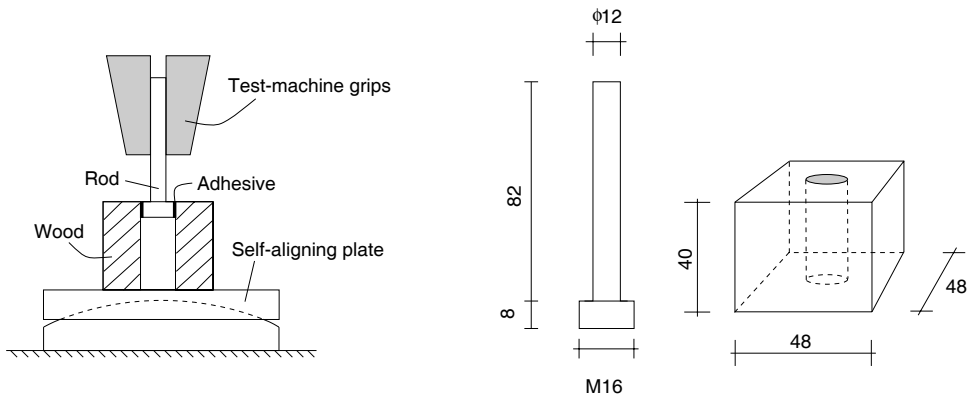


*Fig. 3. - Test specimen and set-up.*

## 2.5 Methods of Evaluation

### 2.5.1 Strength and Work to Failure

From the tests it is straightforward to evaluate the strength of the bond (load divided by fracture area), and to integrate the stress-displacement curve to obtain the work to failure. Here, failure is defined either as a total separation of the bondline with zero load-bearing capacity, or, if the bondline at the end of the test still has a load-bearing capacity due to friction, at a 10 mm deformation of the rod.

When integrating the stress-deformation curve, it was assumed that the fracture area was equal to the area of a cylinder of 16 mm diameter. The lengths of the fracture surfaces were measured after splitting the test specimens to obtain specimens for the density measurements.

The bond shear strength obtained in this way is estimated to be representative, since the short length and the support conditions of the specimen contribute to a uniform stress distribution and small peel stresses. The evaluation of the fracture energy of the bond requires some further consideration since the recorded work to failure is mainly due to friction after the local fracture has taken place in the bond layer. As an example, consider the PRF-bonded specimens, which failed at the thread-adhesive interface. Bearing in mind that the pitch of the used thread is 2 mm, it is obvious that the PRF bondline has fractured completely after a deformation of about 0.5–1.0 mm. The remaining load-bearing capacity is therefore completely due to friction. To overcome such difficulties in the test evaluation a trial and error approach using nonlinear finite element simulations of the tests can be used, fitting local bond strength (shear and peel strength) and fracture energies until the test results (strength, energy and shape of curve) can be reproduced numerically. Another alternative to overcome the difficulty in fracture energy evaluation is discussed and applied below.

### 2.5.2 Evaluation of Shear-slip Curve

To estimate the initial stiffness, all slopes from zero to maximum load were calculated using least square fits, for intervals of length of 25% of the maximum load. The steepest slope was chosen as initial stiffness. Fig. 4 shows the results of the evaluation process for one of the PRF specimens. Three curves are shown. One represents the recorded test data with the load divided by the nominal shear area. As is evident, the slope of the curve increases initially, probably due to rough contact surfaces and the initial movement of the self-aligning plate of the test set-up. Following this initial nonlinear region, an almost perfectly linear part is found, followed by nonlinearities close to peak stress, probably due to an initiating fracture and possibly to plasticity. The second curve shown in Fig. 4 represents the response with the approximated initial elastic stiffness. Finally a curve with the elastic deformations subtracted is shown. For this curve the deformation represents the additional deformation due to damage in the bondline.

### 2.5.3 Characterisation of Fracture Softening

The total energy consumed during the tests is mostly due to friction, after the fracture has taken place, and is not a parameter of large influence on the load-bearing capacity in a structural-sized specimen. Therefore, instead of using the area below the complete

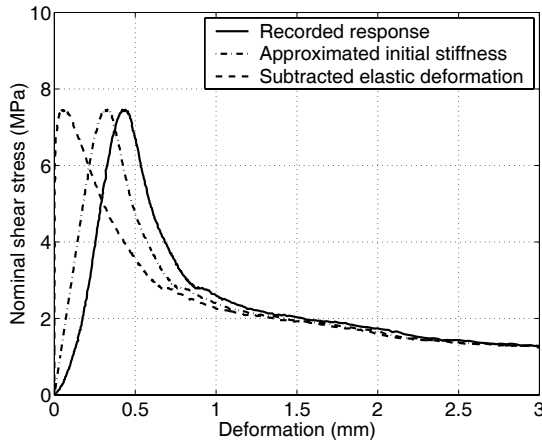


Fig. 4. - Evaluation of the initial stiffness.

stress-displacement curve as a measure of the fracture energy of the bond, the slope of the descending branch is used. This slope is the critical one for a stable response and, furthermore, for structural-sized bonds, the total deformation before collapse is in the range of 1–2 mm rather than of 8–10 mm, which was the typical deformation at complete failure for most of the small specimens tested. For bonds that show negligible plastic response before peak stress, a typical slope of the descending part, together with the strength, define a triangular area that can be used as a measure of the fracture energy. For the cases of considerable plastic response before peak stress, the slope together with the strength and the stress-displacement curve prior to peak stress, define another effective area. This is shown schematically in Fig. 5 for the case with plastic response before peak stress. Note that the initial elastic response of this curve has been subtracted, so that the deformation corresponds to the plastic strain before peak stress and, to the relative slip due to damage or microcracking in the bondline after peak stress.

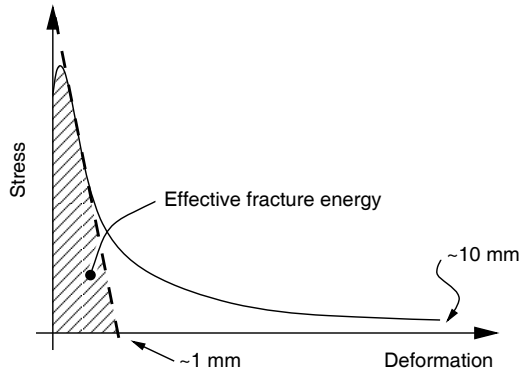


Fig. 5. - An example of how to evaluate the fracture softening of the specimen.

After subtracting the elastic deformations from the recorded shear-slip response, the slope of the descending part of the shear-slip curve was evaluated with the same algorithm as described above for the evaluation of the initial elastic stiffness. This means that here, the fracture-softening properties are characterised by the steepest 25% of the maximum load interval.

### 3 Results and Discussion

#### 3.1 General Remarks

A total of 62 tests were performed, 61 of which are included in the results. The test rejected was one of the FRP specimens, which failed in the rod itself, probably due to damage caused to the rod in the manufacturing of the specimen. The different material combinations and load-to-grain angles, together with the result statistics, are summarised in Table 1. The table gives the average and coefficient of variation (COV) of density, moisture content, strength, negative slope after peak stress, and work to failure respectively. For each nominally equal material combination, five replications were performed with monotonically increasing deformation of the testing machine’s crosshead. In addition, for each material combination, one test was performed with unloading of the specimen in the softening region, after peak stress. The strength and initial elastic slope statistics are all based on six replications, while the other statistics are based on five replications since the unloading part of the curve complicates the evaluation of these quantities. The statistics from the FRP-rod tests are based on seven and six tests respectively. It was possible to record the complete stress-slip curve for all the material combinations and examples of such curves are given below, together with the discussions about the influence of the adhesive type and of the load-to-grain angle.

Table 1: Results from tests, mean values (COV in %).

Material combination (-)	Density (kg/m <sup>3</sup> )	MC (%)	Strength (MPa)	Negative Stiffness (MPa/mm)	Work to failure (kJ/m <sup>2</sup> )
St./C35/PRF/0°	449 (2)	14.4 (1)	7.05 (6)	8.6 (20)	12 (20)
St./C35/PUR/0°	492 (2)	13.2 (2)	10.5 (10)	62 (23)	9.6 (9)
St./C35/EPX/0°	462 (1)	12.8 (1)	13.1 (10)	60 (18)	22 (14)
St./C24/PRF/0°	348 (4)	12.8 (2)	6.18 (5)	7.0 (20)	14 (14)
St./C24/PUR/0°	368 (3)	13.1 (2)	10.6 (5)	62 (4)	8.0 (9)
St./C24/EPX/0°	341 (3)	12.7 (3)	11.0 (12)	52 (8)	21 (18)
St./C35/EPX/22.5°	454 (1)	13.8 (1)	12.8 (4)	48 (13)	23 (4)
St./C35/EPX/45°	429 (10)	13.3 (2)	10.7 (6)	28 (19)	25 (10)
St./C35/EPX/90°	469 (6)	13.5 (2)	7.12 (6)	3.1 (42)	25 (4)
FRP/C35/EPX/0°	451 (1)	13.5 (3)	11.8 (7)	44 (7)	28 (10)

### 3.2 Failure Modes

The failure modes obtained in the tests are of three types, each typical for one type of adhesive:

1. Failure in the adhesive at the threading of the bolt. This failure mode was obtained only for the PRF adhesive covering about 75-100% of the fracture area. The remaining fracture area presented a wood-interface failure.
2. Failure in the adhesive close to the wood. This failure was obtained only for the PUR specimens and, covered 100% of the fracture area.
3. Failure in the wood in the vicinity of the adhesive. Note that this wood failure is not characterised by a large plug being pushed out, but rather by a wood-interface failure due to a weak boundary layer. This failure type was obtained only for the EPX specimens. For the 0° load-to-grain angle tests, there was a fairly large amount of wood fibres visible on the adhesive after failure. For the other load-to-grain angles the fracture surface was almost free from fibres.

In Fig. 6, examples of the different failure modes obtained are shown.

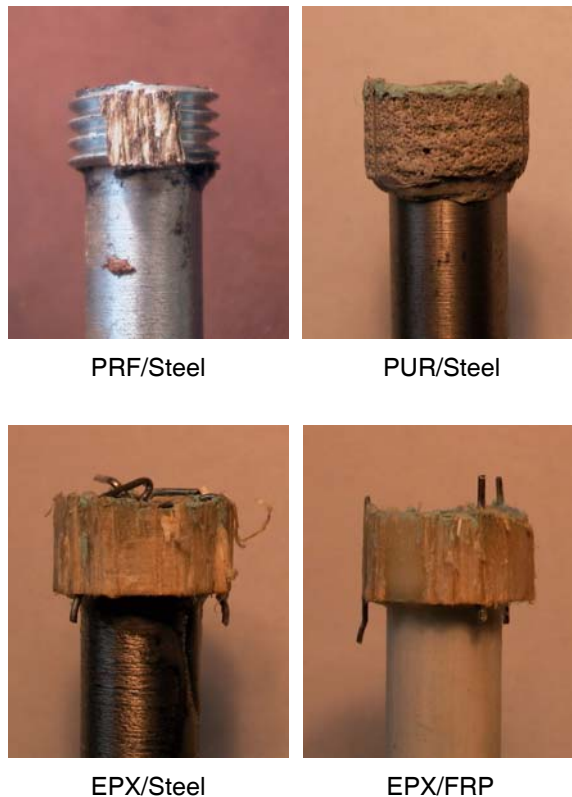


*Fig. 6. - Failure surfaces for PRF, PUR and EPX adhesives respectively.*

The reason for these distinctively different failure modes can be explained as follows: The adhesion of the PRF to the steel is negligible, and in combination with the PRF's tendency to shrink during curing, an initial lack of fit between the adhesive and the threads of the bolt was observed. This results in stress concentrations at the thread/adhesive interface and also a low initial stiffness of the joint. The large stress concentrations lead to the failure at the bolt/adhesive interface region. The PRF adhesive thus works as way to cast threads in the drilled hole and the joint performs more like a bolted connection than an adhesive bond. From the stress-displacement curves, cf. Fig. 4, it is also apparent that there is a considerable amount of frictional work performed during the test. The pitch of the threads used (M16) is 2 mm, and, since the failure takes place at the tip of the threads, an approximately 1 mm deformation implies that the bond line has come to a complete failure.

The curing of the PUR adhesive relies on the possibility of taking up moisture from the adherends and the surrounding air. The chemical reaction forms  $\text{CO}_2$ , which causes bubbles to form in the bondline. In the case of low or no pressure at all during curing, this bubble formation becomes intense. The failure surfaces of the PUR specimens had bubbles of sizes in the order of 0.1–0.5 mm. The bubble formation can be expected to be more intense at the free surface of the adhesive and at the wood interface where more moisture is available. This explains why the fracture surface is located close to the the wood/adhesive interface.

The EPX adhesive gives strong bondlines with good adhesion to the steel, the wood and the FRP rods. The failure is therefore located in the wood, which in this case is the weakest link.

### 3.3 Influence of Adhesive Type and Rod Material

Based on the above discussion of the failure modes, the strength of the adhesives should form a sequence showing increasing strength in the order of: PRF, PUR and EPX. The mean strength as reported above also confirms this. In Fig. 7, hand-drawn mean curves, one for each adhesive, show the influence on the stress-displacement response of the adhesive type. A mean curve for the tests performed on the FRP rod is also shown. The curves show the response with the elastic deformation subtracted. It is clear from the curves that the PUR and the EPX are similar with respect to the slope of the descending part of the curve, while the PRF adhesive shows a much more ductile behaviour.

### 3.4 Influence of Wood Density

The influence of the wood density on the strength is complicated to assess since the density of the wood can be expected to have an influence in at least three ways. Firstly, it is often assumed that the density and the strength of the wood are positively correlated; secondly, a change in density could mean a change in adhesion to the wood, and, finally a change of density can result in different modulus of elasticity, which in turn can affect the strength of a glued-in rod due to a change of the stress-distribution. There is a statistically significant difference (0.05 level) in density between the two timber qualities, but this difference only results in a significant difference (0.05 level) in strength for the PRF and EPX adhesives.

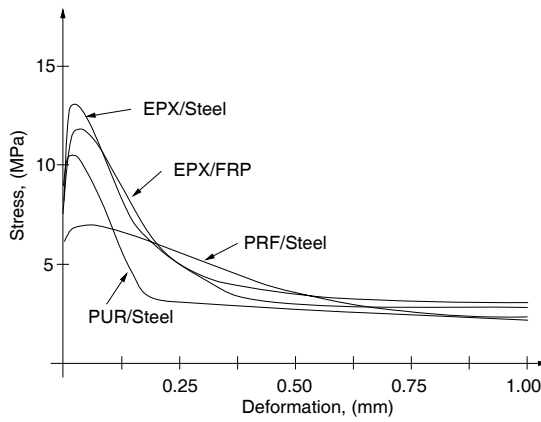


Fig. 7. - Influence of adhesive type and rod material on stress-displacement response. Timber C35,  $0^\circ$  load-to-grain angle.

### 3.5 Influence of Load-to-grain Angle

The influence of the load-to-grain angle on the performance of the bond is of several different types. Changing the load-to-grain angle will affect the effective moduli of elasticity of the adherend. It is also probable that the adhesion of the glue to the wood is different for different orientations, since the surface roughness of the drilled hole depends on the orientation of the grain. Finally it should be emphasised that a load-to-grain angle other than  $0^\circ$  will always result in parts of the wood being stressed in longitudinal shear ( $\tau_{rl}$ ) and other parts in rolling shear ( $\tau_{rt}$ ). Therefore, the results from such a test will be some kind of average, taken in the circumferential direction, which includes both shearing modes. If the strengths in the two directions differ considerably, the fracture will be a propagating one (in the circumferential direction). Such a propagating failure will lead to an apparently ductile behaviour on a larger scale, i.e. the scale on which the present tests are monitored. Fig. 8 shows the influence on the stress-displacement response, with the elastic deformations subtracted. The behaviour of the tests are increasingly ductile as the load-to-grain angle changes from  $0^\circ$  to  $90^\circ$ .

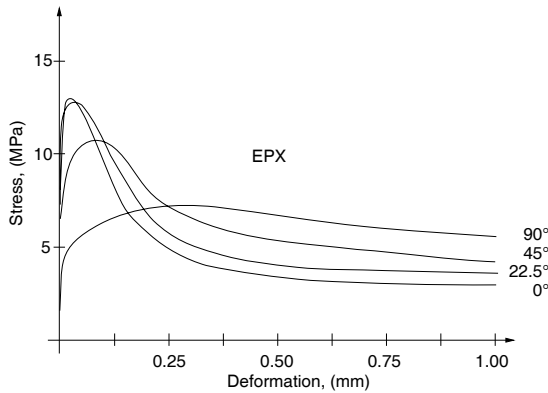


Fig. 8. - Influence of load-to-grain angle on stress-displacement response. Epoxy adhesive, timber C35, steel rod.



## 4 Conclusions

The following conclusions can be drawn from the present work:

- Test methods:
  - Testing for fracture-softening properties is demanding, and several pre-tests to determine a proper test set-up was needed.
  - A test set-up was developed, which proved to work well from a practical point of view and was estimated to give representative and reproducible results.
- Test results:
  - It is possible to obtain the complete shear-stress versus shear-slip response of small glued-in rod specimens.
  - Characteristic and significantly different results were obtained for different adhesives in terms of stress-slip performance, strength, fracture softening and fracture mechanism.
- Methods of test-result evaluation:
  - A method of evaluating the test results in terms of strength and fracture-softening properties has been proposed. The fracture softening is evaluated by using only a part of the stress-displacement curve obtained from tests. This part is defined in terms of the slope of the descending part of the stress-displacement response.

## 5 Acknowledgements

The GIROD project involves the following research institutes: SP – the Swedish National Testing and Research Institute, FMPA Otto-Graf Institute (Germany), the University of Karlsruhe (Germany), TRADA Technology (UK) and Lund University (Sweden). The financial support through grant no. SMT4-CT97-2199 by the European Commission (DG XII) and the co-operation of the partners involved in this research project are gratefully acknowledged.

This research was also in part financially supported by the Swedish Council for Building Research (BFR), project no. 19960633. This support is also gratefully acknowledged.

Finally, a special thanks is directed to Mrs. Rizalina Brillante, for her skilful running of the testing machine.

## References

- [1] Riberholt, H. 'Glued bolts in glulam'. Report R210. (Department of Structural Engineering, Technical University of Denmark, Lyngby, Denmark, 1986).
- [2] Ehlbeck, J. and Siebert, W. 'Praktikable Einleimmethoden und Wirkungsweisen von eingeleimten Gewindestangen unter Axialbelastung bei Übertragung von grossen Kräften und bei Aufnahme von Querkraften in Biegeträgern'. Report. (University of Karlsruhe, Germany, 1987).
- [3] Kangas, J. 'Joints of glulam structures based on glued-in ribbed steel rods.' VTT Publications 196. (Technical research centre of Finland, Espoo, Finland, 1994).
- [4] Deng, J. X. 'Strength of epoxy bonded steel connections in glue laminated timber'. PhD-thesis. Civil engineering research report 97/4. (Dept. of Civil Engineering, University of Canterbury, Christchurch, New Zealand, 1997).
- [5] Aicher, S., Gustafsson, P. J. and Wolf, M. 'Load displacement and bond strength of glued-in rods in timber influenced by adhesive, wood density, rod slenderness and diameter'. Proceedings 1<sup>st</sup> RILEM Symposium on timber engineering, Stockholm, 1999. Ed. L. Boström. (RILEM Publications S.A.R.L. Cachan, France, 1999) pp. 369–378.
- [6] Boström, L. 'Method for determination of the softening behaviour of wood and the applicability of a nonlinear fracture mechanics model'. PhD thesis. Report TVBM-1012. (Lund University, Division of Building Materials, Lund, Sweden, 1992).
- [7] Wernersson, H. 'Fracture characterization of wood adhesive joints'. PhD thesis. Report TVSM-1006. (Lund University, Division of Structural Mechanics, Lund, Sweden, 1994).
- [8] Johansson, C-J., Serrano, E., Gustafsson, P. J. and Enquist, B. 'Axial strength of glued-in bolts. Calculation model based on non-linear fracture mechanics - A preliminary study'. Proceedings CIB-W18. Meeting twenty-eight. Copenhagen, Denmark 1995. (University of Karlsruhe, Germany, 1995).



# *Paper VII*



*A Damage-plasticity Modelling Approach for  
Wood Adhesive Bonds*

*by  
Erik Serrano*





# A Damage-plasticity Modelling Approach for Wood Adhesive Bonds

Erik Serrano

Division of Structural Mechanics, Lund University

## Abstract

In this paper, an interface model based on damage mechanics is suggested for the modelling of wood-adhesive interfaces. The model accounts for joint dilatation and post-cracking friction. Also a homogenisation scheme to combine the proposed model with ordinary plasticity models for the adhesive bulk, is presented. This homogenisation procedure is based on assumptions regarding the stress and strain gradients typical for thin bondlines.

## 1 Introduction

### 1.1 A Micro-structural Background

Three basically different mechanisms could be involved in the formation of a wood adhesive bond [7, 10]:

1. A strictly mechanical bonding by interlocking of glue in the porous structure.
2. *Primary* bonds such as ionic and covalent bonds. These bonds are formed between atoms by the transfer of electrons from one atom to another (ionic) or by sharing electrons (covalent).
3. *Secondary* bonds such as hydrogen bonds, van der Waals bonds and bonds formed by acid-base interactions. These bonds are formed by electrostatic forces between the molecules due to the distribution of electrons.

The experimental evidence of primary, chemical, bond formation for wood adhesives is, however, limited [10], but if possible this type of bond should be the preferred one because of its greater strength and durability.

Marra [10], uses a definition involving nine different materials in a wood adhesive bond. These materials, or “links”, are: the two wood adherends, the two adherend subsurfaces (zones of finite thickness with damaged wood partially penetrated by the adhesive), the adhesive-adherend interface (representing the intermolecular adhesion), an intra-adhesive boundary layer representing a zone with different properties due to the vicinity to the wood and, finally, the adhesive bulk. We will define the adhesive bulk and the wood adherends in the same way, in relation to these nine links. For practical

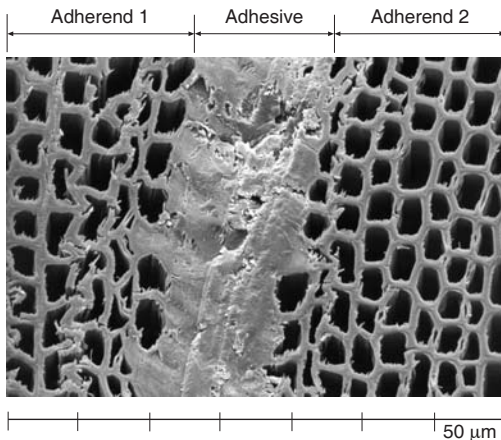


Figure 1: Components of a wood-to-wood adhesive bond, [22].

reasons, however, related to a usable scale in computations of, say,  $10^{-4}m$ , we choose to incorporate the remaining links into interfacial regions. Thus we are left with five regions or “materials”: two adherends, adhesive bulk and two interfaces. The interfacial regions can be expected to have a finite but very small thickness in relation to other dimensions, approximately equal to the penetration of the adhesive into the adherends. The electron-microscope picture in Figure 1 shows a wood-to-wood bondline, glued with a PR adhesive. The penetration of the adhesive seems to be moderate, limited to the first cell row on each side of the bondline.

On the wood surfaces, loose wood fibres are to be found as a result of the machining of the wood prior to gluing. These loose fibres *can* act as a reinforcement of the adhesive, but they probably more often act as mechanically weak sections. Such a weak section is referred to as a mechanically weak boundary layer (MWBL), and the existence of such layers has been the subject of recent research [15]. A MWBL has a similar effect on the joint strength as the chemically weak boundary layer (CWBL), which is defined as a layer on a molecular level with low cohesion [16]. The electron-microscope picture in Figure 2, shows a wood adhesive bond that has fractured. To the left is the wood surface, and to the right we see a part of the adhesive, which has some wood fibres on the surface. These fibres have been a part of the MWBL.

## 1.2 Previous Work

The majority of previous models for adhesive bonds are based on conventional stress analysis or linear elastic fracture mechanics (LEFM) analysis. Using conventional stress analysis, it is possible to obtain straightforward solutions to common engineering problems through standard computer programs and existing material models. For some simple geometries, even analytical solutions may be obtained; a classic example is the so-called Volkersen theory [21]. The main problem in using conventional stress analysis, is that for most situations adhesive bonds include some geometrical features, like sharp corners, which will lead to stress or strain discontinuities. It is not self-evident how to perform, e.g. finite element analysis of such problems, since the discontinuity will

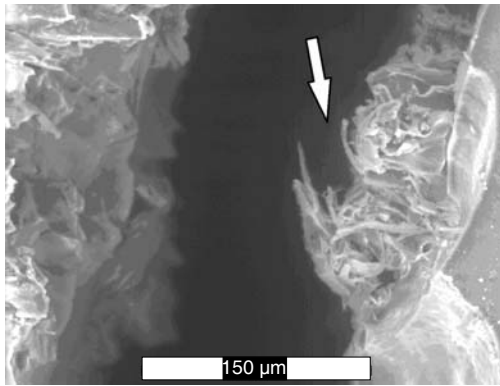


Figure 2: A bundle of fibres are attached to the adhesive after failure in a bondline, [15].

result in a strong mesh dependence of the result in terms of maximum stress. Since the existence of a singular and discontinuous stress field is one of the assumptions in LEFM, such an approach should, in principle, be appropriate in cases of discontinuous geometry or crack-like defects. However, another crucial assumption made within the framework of LEFM, is that the size of the fracture process zone (FPZ) is small, or, strictly speaking, infinitesimal. This means that LEFM is only useful for cases when the real FPZ is small, or at least small in relation to other dimensions of the structure.

Using the concept of a softening model such as, e.g. softening plasticity [13], the fictitious crack model (FCM) [22], crack band models (CBM) [18], continuum damage mechanics (CDM) [8], microplane models [12] or plasticity-damage models [4], it is possible to overcome the above-mentioned drawbacks with stress singularities and the finite size of the FPZ. Within the framework of the so-called generalised Volkersen theory [5], it has been demonstrated that a softening model can be considered the general case, and the perfectly brittle failure according to LEFM and the ductile failure according to an elastic-perfectly plastic model can be considered special cases. For LEFM, it is the fracture energy and the stiffness of the bondline and adherents that govern the strength of the joint, while for an elastic-perfectly plastic model, the local strength is the governing parameter. For any case between these extremes, local strength, stiffnesses and fracture energy are all important to the joint strength.

### 1.3 Aims and Scope of the Present Study

The aims and the scope of this paper are:

- to set up a constitutive model for the wood-to-adhesive interface region of an adhesive bond,
- to combine the interface model with a conventional plasticity model for the adhesive material, and
- to suggest a homogenisation scheme in order to combine these models into a model for the complete bondline



The third item above is especially interesting for applied FE-calculations. The homogenisation concept proposed, a decomposition scheme for *thin* bondlines, should be useful for most situations encountered in practice, since in relation to other dimensions of real structures, most bondlines are, in fact, thin.

## 2 Methods

### 2.1 Definitions and General Assumptions

In the present study, a bondline is defined as the region between two solid adherends. The bondline is subdivided into the adhesive bulk and two interface regions, one in the vicinity of each adherend. Physically, the interface regions have a small but finite thickness, related to the penetration of the adhesive into the wood and to the length of the wood fibres on the adherend surface. Since adhesive bonds are exposed to compressive stresses during curing, resulting in the adhesive penetrating the wood, it seems natural to consider the interface region being a part of the adherend rather than being a part of the adhesive bulk. Normally, in a design situation, the nominal thickness of the bondline, defined as the distance between the two adherend surfaces after curing, is known. However, little or no information is available regarding the penetration of the adhesive into the wood. Therefore, from a practical point of view, it is convenient to define the adhesive bulk thickness as being equal to the nominal thickness of the bondline, and assume the interface region to have a zero thickness.

Figure 3 gives the definitions of the components of a bondline as used in the present paper together with some main notations. The bondline plane is parallel to the  $xz$ -plane. The most important stress components of a bondline, the two in-plane shear components and the peel stress component, would be  $\sigma_{xy}$ ,  $\sigma_{yz}$  and  $\sigma_{yy}$  respectively.

It is assumed that the behaviour of the bondline can be modelled by the behaviour of the adhesive bulk and the interface regions.

The adhesive bulk material is modelled with a plasticity model. It will be assumed that input for such a model can be obtained in tests with specimens consisting of adhesive only. In principle, this can be done by casting small specimens and subject them to a series of tests in order to measure the material model parameters needed. As an example, a shear stress vs. plastic strain recording is sufficient to fit a von Mises plasticity model with isotropic hardening.

The interface response is assumed to be derived from tests with small adhesive bond specimens. A small specimen size will ensure a uniform stress distribution, which is crucial for the test evaluation, and will furthermore facilitate the recording of possible strain softening behaviour. It has been shown by Wernersson [22] and Serrano [17, 20] that tests of this type are possible to perform.

### 2.2 Performance and Analysis at Micro Level

The interface can be considered as consisting of small adhesive droplets trapped in the cavities of the wood and loose fibre ends held in place in the adhesive mainly by frictional forces. A mechanical analogy for such a micro-structure is a bundle of springs, or a network model, bridging a distance equal to the interface thickness. In the present

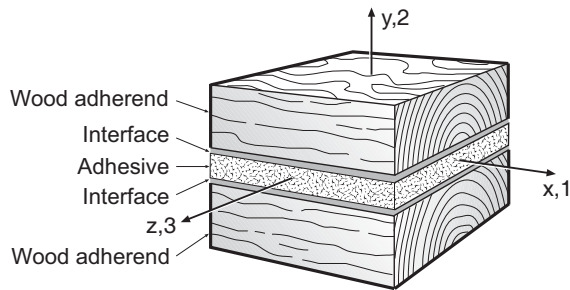


Figure 3: Definition of bondline components.

study, this micro-structure is not modelled in detail. Instead, its response in terms of stress-slip relations is assumed to be known from tests. However, a brief discussion on such models is given here.

For one-dimensional states of e.g. pure tensile stress, a bundle of parallel springs acting in pure tension serves as an analogy for the interface region. Each spring can be assigned a simplified constitutive behaviour, e.g. an elastic-brittle or elastic-perfectly plastic behaviour. The spring characteristics (strength and/or stiffness) can also be assumed to be stochastic variables, correlated or not, and the response of a finite area of the interface is obtained by simply adding up the response of springs acting over the area.

Such a model can be made to coincide with the classic Weibull theory for brittle materials, by assuming that each spring is elastic-brittle with a strength that is Weibull-distributed and acts within an infinitely small area. While the classic Weibull theory assumes a weakest link failure, a strain softening material response with progressive damage will generally be the outcome of the above model. A model based on this concept, but generalised to an orthotropic material for the simulation of fibre-composites, was presented in [1].

An example of a response that can be obtained for a uniaxial state of tensile stress is shown in Figure 4. The curve shown was calculated assuming elastic-brittle behaviour and letting the strength be Weibull-distributed. Note especially that at unloading, the stress-strain relation is directed towards the origin. This is a result of the assumed brittle, linear elastic behaviour of the springs. If the springs are assigned more complex material properties, like e.g. elastic-perfectly plastic behaviour, other responses of the interface region would result. In order to obtain a two- or three-dimensional model, which includes not only stresses perpendicular to the bondline, but also in-plane shear stresses, springs with different, and possibly random, orientation, could be used. More complex network models can also be achieved by using bar or beam elements. Whatever the approach used on this level, in the present study it will be assumed that the response of the interface region can be expressed in terms of stress-strain relations or equivalent stress-relative displacement relations. Transforming stress-strain relations to relative displacement space, involves the introduction of a material length, over which the strains are distributed. The introduction of such a material length is necessary in order to obtain mesh-insensitive results in finite element applications.

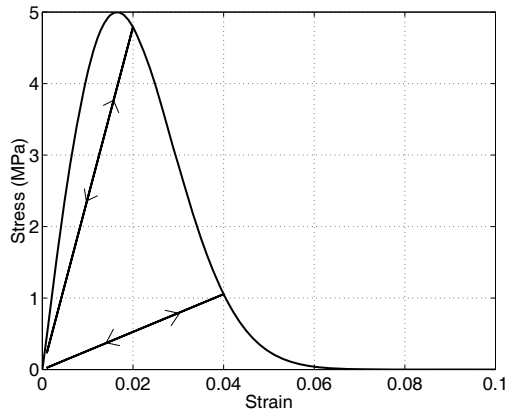


Figure 4: Strain-softening material response obtained with Weibull theory.

## 2.3 An Interface Model Based on Damage

### 2.3.1 Interpretation of Experimental Results

The starting-point of the material model for the interface region is the interpretation of test results. From previous work by Wernersson [22] and Serrano [17] it is known that bondlines can behave in a fracture-softening manner as depicted in Figure 5a.

The first, and crucial, assumption for our derivation is that the plastic response of a bondline is located in the adhesive bulk material, or in the wood adherends. Furthermore, for the interface region we assume a behaviour according to classic continuum damage mechanics (CDM), making the assumption that any additional strains due to damage are fully recoverable. This would lead to an unloading sequence of the complete bondline according to Figure 5b. This unloading behaviour makes it possible to define a set,  $\omega$ , of scalar damage variables,  $\omega_{ij}$ , each scalar  $\omega_{ij}$  being a measure of the loss of effective area, and associated with a certain component of additional strains due to damage as compared to the virgin material. The damage variables can also be interpreted as a loss of stiffness, due to damage, or as a measure of the effective stress acting on the undamaged part of the material. The damage parameters are *not* to be interpreted as second-order tensors. The damage parameters are used so that the one-sidedness of the damage can be modelled, i.e. we make a distinction between the damage parameter in tension and in compression. For the shear damage, however, we will use a formulation which is neutral with respect to the loading direction.

### 2.3.2 Damage Formulation in One Dimension

Consider, as an example, for a one-dimensional case, a material obeying Hooke's law:

$$\sigma = E\epsilon \quad (1)$$

We now assume that damage will evolve in the material as a result of e.g. the mechanical loading, and that the stiffness of the material will be degraded:

$$\sigma = (1 - \omega)E\epsilon \quad (2)$$

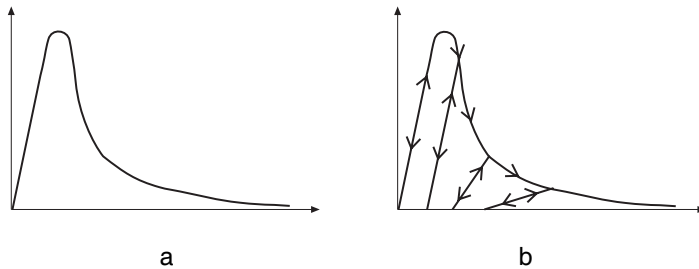


Figure 5: Stress vs. deformation at a) monotonic loading b) unloading with plastic response.

where  $0 < \omega < 1$  is a damage parameter. On the other hand, we could also use the flexibility as a starting-point:

$$\epsilon = \frac{C}{(1 - \omega)} \sigma \quad (3)$$

Of course, Equation (3) could also be interpreted as Hooke's law applied to the undamaged material only:

$$\hat{\sigma} = \sigma / (1 - \omega) = E \epsilon \quad (4)$$

where the effective stress,  $\hat{\sigma}$ , is introduced.

Thus, in this simple one-dimensional case it is trivial, and makes no difference if we use the effective stiffness (Equation (2)), or the effective flexibility, or effective stress (Equations (3) and (4)). As a matter of fact, the relations (2)–(4) can be derived from the free energy of a linear elastic material and with the use of a state law based on this energy, e.g. the Helmholtz free energy,  $\psi$ . For isothermal conditions, we assume the free energy to be a function of strain and damage only:

$$\rho \psi(\epsilon, \omega) = (1 - \omega) \frac{1}{2} E \epsilon^2 \quad (5)$$

In order not to violate the fundamental laws of thermodynamics, it can be shown that the state law

$$\sigma = \rho \frac{\partial \psi}{\partial \epsilon} \quad (6)$$

must be fulfilled – see any textbook on constitutive modelling and thermodynamics, e.g. [14]. Making use of the free energy in the state law then yields the constitutive relation, which in turn, can be interpreted in terms of stiffness degradation, flexibility evolution or effective stress.

### 2.3.3 Damage Formulation in Three Dimensions

For multiaxial stress states, the derivation of a constitutive relation can be made completely analogous to any of the approaches described above. Thus, we choose whether to postulate the evolution of the stiffness degradation, the flexibility, or indeed we give an expression for the free energy directly. However, if we for an anisotropic material derive the constitutive relation from, e.g. the Helmholtz free energy, we will obtain a

complex expression, due to the coupling terms, and the physical interpretation in terms of e.g. stiffness degradation is lost.

Another approach is to postulate the stiffness, or flexibility, in terms of damage, and show that the fundamental laws of thermodynamics are fulfilled. Using such an approach, Matzenmiller *et al.* [11] derived a two-dimensional damage model for orthotropic fibre composites. The damage model was derived by assuming the off-diagonal terms in the flexibility matrix to be unaffected by damage. This was, however, expressed using

$$\begin{bmatrix} \frac{1}{(1-\omega_{11})E_{11}} & -\frac{h_{21}\nu_{21}}{(1-\omega_{22})E_{22}} & 0 \\ -\frac{h_{12}\nu_{12}}{(1-\omega_{11})E_{11}} & \frac{1}{(1-\omega_{22})E_{22}} & 0 \\ 0 & 0 & \frac{1}{(1-\omega_{12})G_{12}} \end{bmatrix} \quad (7)$$

and

$$h_{21} = (1 - \omega_{22}) \quad h_{12} = (1 - \omega_{11}) \quad (8)$$

where (8) was concluded to be realistic, based on experimental evidence and symmetry conditions. The model of Matzenmiller was later extended to a three-dimensional formulation by Borg [1], who used a similar expression for the flexibility. Following the work of Matzenmiller and Borg [1], we will also derive an expression for the flexibility matrix as a function of damage. In the rest of this section we will adopt matrix notation so that stresses and strains are arranged in vectors ( $6 \times 1$ ), and stiffness, flexibility and damage variables are arranged in matrices ( $6 \times 6$ ). With this notation we obtain for a linear elastic material obeying Hooke's law:

$$\boldsymbol{\sigma} = \begin{bmatrix} \sigma_{xx} \\ \sigma_{yy} \\ \sigma_{zz} \\ \sigma_{xy} \\ \sigma_{xz} \\ \sigma_{yz} \end{bmatrix} = \mathbf{D}\boldsymbol{\epsilon} = \begin{bmatrix} D_{11} & D_{12} & D_{13} & D_{14} & D_{15} & D_{16} \\ D_{21} & D_{22} & D_{23} & D_{24} & D_{25} & D_{26} \\ D_{31} & D_{32} & D_{33} & D_{34} & D_{35} & D_{36} \\ D_{41} & D_{42} & D_{43} & D_{44} & D_{45} & D_{46} \\ D_{51} & D_{52} & D_{53} & D_{54} & D_{55} & D_{56} \\ D_{61} & D_{62} & D_{63} & D_{64} & D_{65} & D_{66} \end{bmatrix} \begin{bmatrix} \epsilon_{xx} \\ \epsilon_{yy} \\ \epsilon_{zz} \\ \gamma_{xy} \\ \gamma_{xz} \\ \gamma_{yz} \end{bmatrix} \quad (9)$$

with  $\gamma_{ij}$  denoting the engineering shear strain.

In order to fulfil the fundamental laws of thermodynamics, we will make use of Gibbs' free energy,  $\phi$ , which for a linear elastic material, under isothermal conditions, can be written:

$$\rho\phi(\boldsymbol{\sigma}, \omega_{ij}) = \frac{1}{2}\boldsymbol{\sigma}^T \mathbf{C}(\omega_{ij})\boldsymbol{\sigma} \quad (10)$$

with  $\mathbf{C}$  denoting the flexibility matrix and  $\rho$  the density. The "Clausius-Duhem inequality", see e.g. [9], is for isothermal conditions and uniform temperature in the material:

$$\left( \epsilon_{ij} - \rho \frac{\partial \phi}{\partial \sigma_{ij}} \right) \dot{\sigma}_{ij} + \rho \frac{\partial \phi}{\partial \omega_{ij}} \dot{\omega}_{ij} \geq 0 \quad (11)$$

from which we conclude that:

$$\epsilon_{ij} = \rho \frac{\partial \phi}{\partial \sigma_{ij}} \quad \text{and} \quad \rho \frac{\partial \phi}{\partial \omega_{ij}} \dot{\omega}_{ij} \geq 0 \quad (12)$$

since Equation (11) must hold for arbitrary combinations of  $\dot{\sigma}_{ij}$  and  $\dot{\omega}_{ij}$ .

The loss of effective area will in the general case affect the stress transfer differently in shear and in tension. It is of course possible to introduce a wide range of damage models, using from a single scalar damage variable to tensor-valued parameters. Following the work of Matzenmiller *et al.* we will, however, now introduce the assumption that the off-diagonal entries of  $\mathbf{C}$  are unaffected by damage. We thus introduce six damage parameters,  $\omega_{ij}$ , in the diagonal terms of the flexibility matrix, in a way analogous to Equation (3). The different  $\omega_{ij}$  are denoted with *xyz*-subscripts, analogous to the stress and strain notation defined in (9).

We now define the conjugate forces  $\mathbf{Y}$  (conjugate to  $\boldsymbol{\omega}$ ), according to:

$$\mathbf{Y} = \rho \frac{\partial \phi}{\partial \omega_{ij}} \quad (13)$$

and obtain the “dissipation inequality”, in matrix form written as:

$$\mathbf{Y}^T \dot{\boldsymbol{\omega}} \geq 0 \quad , \quad \dot{\boldsymbol{\omega}} = \left[ \dot{\omega}_{xx} \quad \dot{\omega}_{yy} \quad \dot{\omega}_{zz} \quad \dot{\omega}_{xy} \quad \dot{\omega}_{xz} \quad \dot{\omega}_{yz} \right]^T \quad (14)$$

where we now re-arranged the six active damage variables into vector format.

We now make use of Equation (10) in Equation (13), and obtain for the conjugate forces,  $\mathbf{Y}$ :

$$\mathbf{Y} = \frac{1}{2} \begin{bmatrix} \frac{\sigma_{xx}^2}{(1-\omega_{xx})^2 E_x} \\ \frac{\sigma_{yy}^2}{(1-\omega_{yy})^2 E_y} \\ \frac{\sigma_{zz}^2}{(1-\omega_{zz})^2 E_z} \\ \frac{\sigma_{xy}^2}{(1-\omega_{xy})^2 G_{xy}} \\ \frac{\sigma_{xz}^2}{(1-\omega_{xz})^2 G_{xz}} \\ \frac{\sigma_{yz}^2}{(1-\omega_{yz})^2 G_{yz}} \end{bmatrix} \quad (15)$$

with  $E_i$  and  $G_{ij}$  denoting the engineering constants.

Since all the entries in  $\mathbf{Y}$  are non-negative, one way to fulfil the dissipation inequality is to simply postulate that all the rates of damage are non-negative. Thus:

$$\dot{\omega}_{ij} \geq 0 \quad (16)$$

is a sufficient, but not a necessary condition in order to fulfil (14). The present formulation thus excludes materials with healing capacities, but this is not necessary.

The next step of our derivation is to select suitable expressions to monitor the growth of damage. We therefore define a set of *uniaxial* damage strains,  $\epsilon_{ij}^{d0}$ , defined according to:

$$\epsilon_{xx}^{d0} = \frac{\epsilon_{xx} - \epsilon_{xx}^{f0}}{\epsilon_{xx}^{c0} - \epsilon_{xx}^{f0}}; \quad \epsilon_{yy}^{d0} = \frac{\epsilon_{yy} - \epsilon_{yy}^{f0}}{\epsilon_{yy}^{c0} - \epsilon_{yy}^{f0}}; \quad \epsilon_{yz}^{d0} = \dots \quad (17)$$

where  $\epsilon_{ij}^{f0}$  is a strain component at damage initiation and  $\epsilon_{ij}^{c0}$  is a strain component at complete damage, both referring to uniaxial loading, and assumed to be known from tests.

From tests, resulting in curves similar to those in Figure 5, we can extract the expressions for the damage evolution by measuring the stiffness degradation as a function of  $\epsilon^{d0}$ . These one-dimensional functions are denoted by:

$$\omega_{ij} = g_{ij}(\epsilon_{ij}^{d0}) \quad (18)$$

The damage formulation for three-dimensional cases will be formulated in terms of the one-dimensional functions of the type (18). Together with measured, or previously known values of the virgin-material stiffness, these functions define the complete set of parameters needed.

We assume that the strain at damage initiation,  $\epsilon^f$ , and the strain at complete damage,  $\epsilon^c$  for multi-axial states is described by an interaction of the type:

$$1 = \left(\frac{\epsilon_{xx}^f}{f_0}\right)^m + \left(\frac{\epsilon_{yy}^f}{f_0}\right)^n + \dots + \left(\frac{\epsilon_{yz}^f}{f_0}\right)^r \quad (19)$$

$$1 = \left(\frac{\epsilon_{xx}^c}{c_0}\right)^m + \left(\frac{\epsilon_{yy}^c}{c_0}\right)^n + \dots + \left(\frac{\epsilon_{yz}^c}{c_0}\right)^r \quad (20)$$

Equations (19) and (20) define two hyper surfaces (ellipsoids for  $m = n = \dots = r = 2$ ) in strain space corresponding to the initial elastic, undamaged, region and the complete damage limit. In order to obtain a multiaxial equivalent form of the damage strain in Equation (17) we define the current damage strain,  $\epsilon^d$ , according to

$$\epsilon^d = \frac{|\epsilon| - |\epsilon^f|}{|\epsilon^c| - |\epsilon^f|} \quad 0 \leq \epsilon^d \leq 1 \quad (21)$$

which is a relative measure of the distance from the initial undamaged region, following a radial path in strain space. We now make use of (18) in order to obtain a generalised format for the damage:

$$\omega_{ij} = g_{ij}(\epsilon^d) \quad (22)$$

Thus,  $\epsilon^d$  is used in the three-dimensional case in order to monitor the damage variables  $\omega_{ij}$  in the same way that the strains  $\epsilon_{ij}^{d0}$  are used in the one-dimensional case.

For a general three-dimensional case it would be necessary to determine six one-dimensional functions  $g_{ij}$ . However, since the main application in mind relates to wood adhesive bonds, and since these involve a bi-material interface, it is here assumed that damage will evolve only in one plane which is parallel to the  $xz$ -plane, and that the damage strain  $\epsilon^d$  is a function only of  $\epsilon_{yy}$ ,  $\epsilon_{xy}$  and  $\epsilon_{yz}$ . We then obtain (cf. Equations (19) and (20)):

$$1 = \left(\frac{\epsilon_{yy}^f}{f_0}\right)^m + \left(\frac{\epsilon_{xy}^f}{f_0}\right)^n + \left(\frac{\epsilon_{yz}^f}{f_0}\right)^r \quad (23)$$

$$1 = \left(\frac{\epsilon_{yy}^c}{c_0}\right)^m + \left(\frac{\epsilon_{xy}^c}{c_0}\right)^n + \left(\frac{\epsilon_{yz}^c}{c_0}\right)^r \quad (24)$$

In order to form a closed surface, it is assumed that the terms of Equation (23) and (24) are all non-negative, i.e. the strain ratios are all non-negative. The above expansion to multiaxial conditions leads to the fact that for constant values of  $0 < \epsilon^d < 1$  we have

constant, but different, values of the damage variables. Furthermore, we will always fulfil  $\omega_{yy} = \omega_{xy} = \omega_{yz} = 0$  prior to any damage and  $\omega_{yy} = \omega_{xy} = \omega_{yz} = 1$  (simultaneously) at complete damage. Thus damage is induced at the same moment for all modes, and complete damage is also achieved simultaneously for all modes. If another definition of the damage strain is used, it is possible to obtain damage initiation and complete damage at different instants.

Since we for the present case only consider one potential failure plane, we are dealing with only three active damage variables,  $\omega_{yy}$ ,  $\omega_{xy}$  and  $\omega_{yz}$ . For a general three-dimensional case, we could make use of expressions similar to (21) for every potential failure plane. In the case of a strongly orthotropic material like wood, it is often assumed that three potential planes of failure exist and that these are defined by the principal directions of the material.

The present formulation relies on the fact that we postulate the flexibility of the material and how this changes as the damage grows. This leads to a simple formulation, with which it is easy to fulfil the dissipation inequality, i.e. by postulating the damage to grow monotonically. As mentioned in the introduction to this section, another approach to formulating damage models is to set up expressions for the free energy and from this derive the constitutive relation. The result will, in the general anisotropic and three-dimensional case, be that the physical interpretation of the flexibility of the material is lost due to the complex nature of the Poisson-terms.

### 2.3.4 Active Components and Loading Directions

The present application of the model, a bondline interface, can be expected to have a small, non-zero physical thickness. However, as stated in the introduction, it might be of practical interest to project the response of the interface zone to zero thickness. For this case, the strains are transformed to equivalent shear and normal slips across the interface, and furthermore, the influence of the stresses  $\sigma_{xx}$ ,  $\sigma_{zz}$  and  $\sigma_{xz}$  on the equilibrium, can be disregarded.

Until now we have left unspecified the explicit form of the functions for damage growth. Instead, they were assumed to be available for uniaxial states of stress, and the suggested model generalised them to multiaxial states. It seems reasonable to assume that the functions defining the damage growth associated with the shear stress components should be symmetric with respect to the loading direction. This is indeed achieved by using the above formulation.

In loading cases involving tensile stresses, the model should account for a progressive loss of stiffness and strength and eventually a complete fracture. For compressive stresses, however, this degradation is not as obvious. Therefore, it will be assumed here that damage, as described above, will only evolve for tensile stresses, and that the damage parameter which controls damage for compressive stresses is constant and equal to zero. Thus, we have:

$$\omega_{yy} = \begin{cases} \geq 0 & \text{for } \sigma_{yy} \geq 0 \\ 0 & \text{for } \sigma_{yy} < 0 \end{cases} \quad (25)$$



### 2.3.5 Interface Dilatation and Post-cracking Friction

In order to obtain a more realistic interface model for large slips, the phenomena of dilatation and post-cracking friction can be included. By dilatation is meant a wedging effect of the interface, i.e. a tendency to expand perpendicular to the interface plane at large shear slips. If the expansion is restrained, compressive normal stresses will develop perpendicular to the interface plane. A schematic representation of the damaged material is shown in Figure 6.

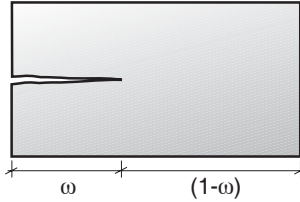


Figure 6: Schematic representation of damaged material.

The dilatational behaviour is based on the assumption that only the completely damaged material is involved, and that if the normal stresses are compressive in the damaged part, all the damaged material is in contact. Since the current model does not account for damage in the compressive regime, the normal stiffness of the interface will change abruptly when contact is regained. In a work on cementitious interface models, Jefferson [6] used a plasticity-damage model and a “contact parameter” to monitor the amount of damaged material in contact. Using such a contact parameter allows for the stiffness transition to be smooth. Since the interface thickness is small, or even zero, it is reasonable to use a high penalty stiffness in the damaged part for large compressive normal stresses. This high stiffness resembles the fact that it is difficult to regain the original thickness of the interface after damage has evolved. The present model activates a high penalty stiffness when the normal strains are less than a specified fraction of the unconstrained dilatational displacement.

In order to exemplify how the dilatation and frictional components are introduced, we make use of an orthotropic elastic virgin material with three damage variables and consider three active stress components. We assume that the dilatancy is the result of the surface roughness of the damaged material. Here we will assume a linear dependency of the free dilatation on shear slip according to Figure 7. Note that this figure shows the dilatation in the damaged part of the material. In order to be monotonically increasing the dilatation is also assumed to be irreversible.

Referring to Figures 6 and 7 we write for the stresses active in the failure plane considered:

$$\boldsymbol{\sigma} = \mathbf{D}\boldsymbol{\epsilon} + \boldsymbol{\sigma}^{dil} \quad \text{with} \quad \left\{ \begin{array}{l} \boldsymbol{\sigma}^{dil} = \begin{bmatrix} \omega_{yy} E_c^0 (\epsilon_{yy} - \eta_0) \\ \tau_{xy}^f \\ \tau_{yz}^f \end{bmatrix} \quad \text{if } (\epsilon_{yy} - \eta_0) < 0 \\ 0 \quad \quad \quad \text{otherwise} \end{array} \right. \quad (26)$$

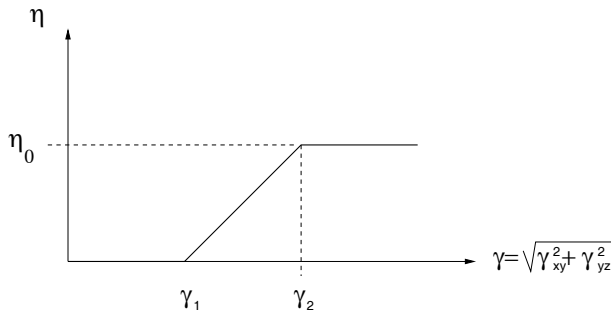


Figure 7: Free dilatation (i.e.  $\sigma_{yy} = 0$  in the damaged part), vs. shear slip.

where  $\mathbf{D}$  denotes the stiffness matrix of the material, which is a function of damage,  $E_c^0$  denotes the modulus of elasticity in compression and finally  $\tau^f$  denote the frictional shear stresses, which for compressive normal stress in the damaged part of the material are given by:

$$|\tau_{xy}^f| \leq |\mu\omega_{xy}E_c^0(\epsilon_{yy} - \eta_0)| \quad (27)$$

$$|\tau_{yz}^f| \leq |\mu\omega_{yz}E_c^0(\epsilon_{yy} - \eta_0)| \quad (28)$$

The friction model thus corresponds to the simplest possible isotropic rigid-perfectly-plastic behaviour, but of course a more complex model could also be appropriate. The stiffness in compression in the damaged part of the material,  $E_c^0$ , is thought to be of orders of magnitude less than the stiffness of the undamaged material. This can be explained by the fact that only a part of the damaged material is actually in contact, due to the surface roughness.

## 2.4 Using Plasticity Models for Wood Adhesive Bonds

The present study aims at developing a new interface model, and combining this with an appropriate plasticity model for the adhesive bulk. Thus it is not the aim to develop a new plasticity model. However, for the sake of completeness, a short derivation of classic theory of plasticity will be given here, largely following the outline given in [13]. The presentation is based on small strain theory, in contrast to the fact that for some types of adhesives like PVAc's, extremely large strains can develop across the bondline [17, 22]. However, the large strains observed in tests (sometimes in the order of 100% engineering shear strain, prior to peak stress) can be contributed also to damage, and still for other, more commonly used adhesives, the strains prior to peak stress are small. Since it is beyond the scope of the present paper to derive a plasticity model for adhesives, we merely conclude that it is possible to use large strain plasticity theory, but that the choice of *which* large strain plasticity theory to use is far from being obvious [14].

The starting-point of small-strain plasticity theory is the split of the total deformation into an elastic, recoverable, and a plastic, irrecoverable, part (in this section we will use index notation  $i = 1, 2, 3$ ):

$$u_i = u_i^e + u_i^{pl} \quad (29)$$

According to small strain theory, the strain tensor is defined according to:

$$\epsilon_{ij} = \frac{1}{2} \left( \frac{\partial u_i}{\partial x_j} + \frac{\partial u_j}{\partial x_i} \right) \quad (30)$$

Since this relation is linear in  $u_i$ , it follows that

$$\epsilon_{ij} = \frac{1}{2} \left( \frac{\partial u_i^e}{\partial x_j} + \frac{\partial u_j^e}{\partial x_i} \right) + \frac{1}{2} \left( \frac{\partial u_i^{pl}}{\partial x_j} + \frac{\partial u_j^{pl}}{\partial x_i} \right) = \epsilon_{ij}^e + \epsilon_{ij}^{pl} \quad (31)$$

which is the well-known assumption of the additive decomposition of the total strain tensor. This decomposition can be done since the strain measure used is linear. For large strain plasticity, such an additive split cannot be unambiguously defined [14]. We also note that the elastic strains are determined by Hooke's law, so that we obtain:

$$\dot{\sigma}_{ij} = D_{ijkl} (\dot{\epsilon}_{kl} - \dot{\epsilon}_{kl}^{pl}) \quad (32)$$

where it is assumed that the elasticity tensor  $D_{ijkl}$  is constant. We now define a yield criterion,  $F$ , which is a function of the stress and a set of hardening parameters, which define the change of the yield surface as a function of plastic loading,  $K^\alpha$  ( $\alpha = 1, 2, 3, \dots$ ):

$$F(\sigma_{ij}, K^\alpha) = 0 \quad (33)$$

The hardening parameters,  $K^\alpha$ , are assumed to depend on a set of internal variables,  $\kappa^\alpha$ , which monitor the plastic loading history of the material. This in turn means that for elastic loading, i.e. no evolution of plastic strain, we have

$$\dot{K}^\alpha = \frac{\partial K^\alpha}{\partial \kappa^\alpha} \dot{\kappa}^\alpha = 0 \quad (34)$$

We note that during yielding the stresses should remain on the yield surface, which means that the consistency relation

$$\dot{F} = \frac{\partial F}{\partial \sigma_{ij}} \dot{\sigma}_{ij} + \frac{\partial F}{\partial K^\alpha} \dot{K}^\alpha = 0 \quad (35)$$

must be fulfilled. The flow rule,

$$\dot{\epsilon}_{ij}^{pl} = \dot{\lambda} \frac{\partial G}{\partial \sigma_{ij}} \quad (36)$$

determines the evolution of plastic strain, and states that the plastic strain rate is directed parallel to the normal of the plastic potential,  $G$ . The scalar  $\dot{\lambda}$  is called the plastic multiplier. If we assume the evolution laws of the internal variables to be homogeneous functions of time we can write:

$$\dot{\kappa}^\alpha = k^\alpha(\dot{\lambda}, \sigma_{ij}, K) = \dot{\lambda} k^\alpha(\sigma_{ij}, K) \quad (37)$$

Introducing the evolution law (37) into Equation (34) and using the result in the consistency relation (35) yields:

$$\frac{\partial F}{\partial \sigma_{ij}} \dot{\sigma}_{ij} - H \dot{\lambda} = 0 \quad (38)$$

where  $H$  is the generalised plastic modulus and is defined by:

$$H = -\frac{\partial F}{\partial K^\alpha} \frac{\partial K^\alpha}{\partial \kappa^\beta} k^\beta \quad (39)$$

Now, making use of Hooke's law (32) in the flow rule (36), we get

$$\dot{\sigma}_{ij} = D_{ijkl} \dot{\epsilon}_{kl} - \dot{\lambda} D_{ijmn} \frac{\partial G}{\partial \sigma_{mn}} \quad (40)$$

Multiplying this by  $\frac{\partial F}{\partial \sigma_{ij}}$  and inserting it into the consistency relation (38), we obtain

$$\frac{\partial F}{\partial \sigma_{ij}} (D_{ijkl} \dot{\epsilon}_{kl} - \dot{\lambda} D_{ijmn} \frac{\partial G}{\partial \sigma_{mn}}) - H \dot{\lambda} = 0 \quad (41)$$

which after re arranging results in

$$\dot{\lambda} = \frac{\frac{\partial F}{\partial \sigma_{ij}}}{H + \frac{\partial F}{\partial \sigma_{ij}} D_{ijmn} \frac{\partial G}{\partial \sigma_{mn}}} D_{ijkl} \dot{\epsilon}_{kl} \quad (42)$$

Inserting this into the flow rule (36) finally results in

$$\dot{\epsilon}_{ij}^{pl} = \frac{\frac{\partial F}{\partial \sigma_{kl}} D_{klmn} \dot{\epsilon}_{mn} \frac{\partial G}{\partial \sigma_{ij}}}{H + \frac{\partial F}{\partial \sigma_{ij}} D_{ijmn} \frac{\partial G}{\partial \sigma_{mn}}} \quad (43)$$

This result shows that the plastic strain rate can be calculated if we have the total strain rate,  $\dot{\epsilon}_{ij}$ , and after inserting (42) into (40), we obtain

$$\dot{\sigma}_{ij} = D_{ijkl} \dot{\epsilon}_{kl} - \frac{D_{ijmn} \frac{\partial G}{\partial \sigma_{mn}} \frac{\partial F}{\partial \sigma_{st}} D_{stkl}}{H + \frac{\partial F}{\partial \sigma_{ij}} D_{ijmn} \frac{\partial G}{\partial \sigma_{mn}}} \dot{\epsilon}_{kl} = D_{ijkl}^{ep} \dot{\epsilon}_{kl} \quad (44)$$

This defines the rate independent elasto-plastic stiffness tensor,  $D_{ijkl}^{ep}$ . Since the total strain rate is used in this relation, it is referred to as a *strain driven* format.

For the present study it is enough to conclude that the strain driven format derived above is used in the integration of the elasto-plastic constitutive equations, in order to update the unknown stresses for the next step of an incremental solution procedure. For a load step involving purely plastic behaviour we write formally

$$\boldsymbol{\sigma}^{i+1} = \boldsymbol{\sigma}^i + \int_{\boldsymbol{\epsilon}_i}^{\boldsymbol{\epsilon}^{i+1}} \mathbf{D}^{ep} d\boldsymbol{\epsilon} \quad (45)$$

## 2.5 A Strain Decomposition Scheme for Thin Bondlines

In this section, a strain decomposition scheme, which can be used for thin bondlines is proposed. This scheme is a part of a homogenisation procedure on a material point level. The basic idea is to characterise an adhesive bond by a single ‘‘bondline material layer’’, whose characteristics depend on the two layers referred to as adhesive bulk and interface respectively.

### 2.5.1 General Remarks on Thin Bondlines

A typical engineering approximation is to say that a bondline is thin if its thickness is small in relation to other dimensions. In this sense we may conclude that, for common design situations in timber engineering involving structural-sized components, the thickness of a wood adhesive bondlines is indeed small, since a typical bondline thickness is in the range of  $10^{-4}$ – $10^{-3}m$  and a typical dimension is in the range of  $10^{-1}$ – $10^1m$ . Another definition of a thin bondline might be to state that it is thin if the stress perpendicular to the bondline plane and the two in-plane shear components are constant with respect to the thickness direction.

In other words, we assume the stresses  $\sigma_{xy}$ ,  $\sigma_{yz}$  and  $\sigma_{yy}$  all to be constant with respect to  $y$ . This is a reasonable assumption to make, since for continuity reasons, this must be fulfilled in the limit as the bondline thickness approaches zero. Using the same continuity argument, we can conclude that the strains  $\epsilon_{xx}$ ,  $\epsilon_{zz}$  and  $\epsilon_{xz}$  also can be assumed to be constant with respect to the thickness direction.

For linear elastic stress analyses, geometric discontinuities, like the sharp corners of a single overlap joint, will give rise to singular stress fields. But also for an approach assuming the stresses in the bondline to be finite, which of course is a more realistic assumption, we still have large stress gradients at failure initiation. We might then conclude that the use of the thin bondline assumptions may lead to erroneous results in analysing the load-bearing capacity. However, for wood adhesive bonds, previous research results have demonstrated that progressive failure can take place, and that it often can be of importance for the load bearing capacity [22, 17, 19]. Presumably, the mechanical behaviour of wood adhesive bonds is highly influenced by the quasi-brittle behaviour of the wood. For solid wood there are also investigations demonstrating that wood, in tensile loading perpendicular to grain and in longitudinal shear, indeed can be regarded as a quasi-brittle, strain-softening material, [2, 3].

### 2.5.2 General Assumptions and Notation

In the following, it will be assumed that the bondline consists of two layers, denoted by preceding superscripts 1 and 2, with different thicknesses,  $t_1$  and  $t_2$ . The stresses, strains and stiffnesses of this homogenised material are denoted with a star superscript. It is not assumed that  $t_1$  is larger than  $t_2$ , but bearing the present application in mind, it is natural to think of the two layers as being the adhesive bulk and the interface region on one side of the bondline. For clarity we will only consider one interface layer, but this will not, in principle, influence on any of the derivations.

We will assume the bondline to be thin in relation to other dimensions, so that we can make use of the above-mentioned assumptions regarding stress and strain components. The constitutive relations of the two layers are assumed to be given in a rate form like the one used in plasticity theory. Here, the following matrix notation will be used:

$${}^1\dot{\sigma} = {}^1D^1\dot{\epsilon}, \quad {}^2\dot{\sigma} = {}^2D^2\dot{\epsilon}, \quad \dot{\sigma}^* = D^*\dot{\epsilon}^* \quad (46)$$

where the matrix dimensions are consistent with the number of active stress components. This means that the stiffness matrices are of dimensions  $(6 \times 6)$  and the stress and strain vectors are of dimensions  $(6 \times 1)$ . For the different components we will use the following notation:

$$\dot{\sigma}^1 = \begin{bmatrix} {}^1\dot{\sigma}_{xx} \\ {}^1\dot{\sigma}_{yy} \\ {}^1\dot{\sigma}_{zz} \\ {}^1\dot{\sigma}_{xy} \\ {}^1\dot{\sigma}_{xz} \\ {}^1\dot{\sigma}_{yz} \end{bmatrix} = \begin{bmatrix} {}^1\dot{\sigma}_1 \\ {}^1\dot{\sigma}_2 \\ {}^1\dot{\sigma}_3 \\ {}^1\dot{\sigma}_4 \\ {}^1\dot{\sigma}_5 \\ {}^1\dot{\sigma}_6 \end{bmatrix} \quad {}^1\mathbf{D} = \begin{bmatrix} {}^1D_{11} & {}^1D_{12} & {}^1D_{13} & {}^1D_{14} & {}^1D_{15} & {}^1D_{16} \\ {}^1D_{21} & {}^1D_{22} & {}^1D_{23} & {}^1D_{24} & {}^1D_{25} & {}^1D_{26} \\ {}^1D_{31} & {}^1D_{32} & {}^1D_{33} & {}^1D_{34} & {}^1D_{35} & {}^1D_{36} \\ {}^1D_{41} & {}^1D_{42} & {}^1D_{43} & {}^1D_{44} & {}^1D_{45} & {}^1D_{46} \\ {}^1D_{51} & {}^1D_{52} & {}^1D_{53} & {}^1D_{54} & {}^1D_{55} & {}^1D_{56} \\ {}^1D_{61} & {}^1D_{62} & {}^1D_{63} & {}^1D_{64} & {}^1D_{65} & {}^1D_{66} \end{bmatrix} \quad (47)$$

where the indices of the terms relate to their row-column position.

According to the thin bondline assumptions we write:

$${}^1\dot{\sigma}_2 = {}^2\dot{\sigma}_2 = \dot{\sigma}_2^* \quad ; \quad {}^1\dot{\sigma}_4 = {}^2\dot{\sigma}_4 = \dot{\sigma}_4^* \quad ; \quad {}^1\dot{\sigma}_6 = {}^2\dot{\sigma}_6 = \dot{\sigma}_6^* \quad (48)$$

for the stresses. This can be interpreted as a series system of stress transfer, a mechanical analogy being two end-joined bars. In order to assure displacement continuity for the homogenised material in relation to the displacement in the two layers, we must have (for constant strains within each layer):

$${}^1\dot{\epsilon}_2 t_1 + {}^2\dot{\epsilon}_2 t_2 = \dot{\epsilon}_2^*(t_1 + t_2) \quad (49)$$

$${}^1\dot{\epsilon}_4 t_1 + {}^2\dot{\epsilon}_4 t_2 = \dot{\epsilon}_4^*(t_1 + t_2) \quad (50)$$

$${}^1\dot{\epsilon}_6 t_1 + {}^2\dot{\epsilon}_6 t_2 = \dot{\epsilon}_6^*(t_1 + t_2) \quad (51)$$

We also make the following assumption regarding the strains

$${}^1\dot{\epsilon}_1 = {}^2\dot{\epsilon}_1 = \dot{\epsilon}_1^* \quad ; \quad {}^1\dot{\epsilon}_3 = {}^2\dot{\epsilon}_3 = \dot{\epsilon}_3^* \quad ; \quad {}^1\dot{\epsilon}_5 = {}^2\dot{\epsilon}_5 = \dot{\epsilon}_5^* \quad ; \quad (52)$$

which can be derived from continuity requirements in the limiting case of zero thickness. Equation (52) can be seen as a parallel system in stress transfer, the mechanical analogy being a fibre bundle loaded in tension. Finally, in order to ensure that the forces on the two layers and on the homogenised material are statically equivalent we must also have (for constant stress within each layer):

$${}^1\dot{\sigma}_1 t_1 + {}^2\dot{\sigma}_1 t_2 = \dot{\sigma}_1^*(t_1 + t_2) \quad (53)$$

$${}^1\dot{\sigma}_3 t_1 + {}^2\dot{\sigma}_3 t_2 = \dot{\sigma}_3^*(t_1 + t_2) \quad (54)$$

$${}^1\dot{\sigma}_5 t_1 + {}^2\dot{\sigma}_5 t_2 = \dot{\sigma}_5^*(t_1 + t_2) \quad (55)$$

### 2.5.3 Decomposition of Strains

We are looking for such an expression that for a given total strain in the homogenised material we can calculate the strains in layers 1 and 2. If the layerwise strains are known, we can use the constitutive relations (46) in order to obtain the layerwise stresses. Once they are obtained, we can use the relations (48) and (53)–(55) to obtain the stresses in the homogenised material. In order to obtain the tangential stiffness matrix of the homogenised material, we can prescribe the strains according to six (in the three-dimensional case) basic uniaxial states, and the resulting stresses are then equivalent to the columns of the stiffness matrix,  $\mathbf{D}$ .

We assume the total strains to be known, and we can then write, using (52):

$${}^1\dot{\boldsymbol{\epsilon}} = \begin{bmatrix} \dot{\epsilon}_1^* \\ {}^1\dot{\epsilon}_2 \\ \dot{\epsilon}_3^* \\ {}^1\dot{\epsilon}_4 \\ \dot{\epsilon}_5^* \\ {}^1\dot{\epsilon}_6 \end{bmatrix} \quad {}^2\dot{\boldsymbol{\epsilon}} = \begin{bmatrix} \dot{\epsilon}_1^* \\ {}^2\dot{\epsilon}_2 \\ \dot{\epsilon}_3^* \\ {}^2\dot{\epsilon}_4 \\ \dot{\epsilon}_5^* \\ {}^2\dot{\epsilon}_6 \end{bmatrix} \quad (56)$$

resulting in three unknown strain components in each layer. To solve these, we proceed in the following manner:

First we make use of the constitutive relations (46) which enable us to set up two expressions for the stresses  ${}^1\dot{\sigma}_2$  and  ${}^2\dot{\sigma}_2$  respectively.

$${}^1\dot{\sigma}_2 = {}^1D_{21}{}^1\dot{\epsilon}_1 + {}^1D_{22}{}^1\dot{\epsilon}_2 + {}^1D_{23}{}^1\dot{\epsilon}_3 + {}^1D_{24}{}^1\dot{\epsilon}_4 + {}^1D_{25}{}^1\dot{\epsilon}_5 + {}^1D_{26}{}^1\dot{\epsilon}_6 \quad (57)$$

$${}^2\dot{\sigma}_2 = {}^2D_{21}{}^2\dot{\epsilon}_1 + {}^2D_{22}{}^2\dot{\epsilon}_2 + {}^2D_{23}{}^2\dot{\epsilon}_3 + {}^2D_{24}{}^2\dot{\epsilon}_4 + {}^2D_{25}{}^2\dot{\epsilon}_5 + {}^2D_{26}{}^2\dot{\epsilon}_6 \quad (58)$$

Now we make use of Equation (56) in (57), and using (49)–(51) we eliminate the strains  ${}^2\dot{\epsilon}_2$ ,  ${}^2\dot{\epsilon}_4$  and  ${}^2\dot{\epsilon}_6$ . We obtain

$${}^1\dot{\sigma}_2 = {}^1D_{21}\dot{\epsilon}_1^* + {}^1D_{22}{}^1\dot{\epsilon}_2 + {}^1D_{23}\dot{\epsilon}_3^* + {}^1D_{24}{}^1\dot{\epsilon}_4 + {}^1D_{25}\dot{\epsilon}_5^* + {}^1D_{26}{}^1\dot{\epsilon}_6 \quad (59)$$

$$\begin{aligned} {}^2\dot{\sigma}_2 &= {}^2D_{21}\dot{\epsilon}_1^* + {}^2D_{22}t_a\dot{\epsilon}_2^* - {}^2D_{22}t_b{}^1\dot{\epsilon}_2 + {}^2D_{23}\dot{\epsilon}_3^* + {}^2D_{24}t_a\dot{\epsilon}_4^* - {}^2D_{24}t_b{}^1\dot{\epsilon}_4 + \\ &{}^2D_{25}\dot{\epsilon}_5^* + {}^2D_{26}t_a\dot{\epsilon}_6^* - {}^2D_{26}t_b{}^1\dot{\epsilon}_6 \end{aligned} \quad (60)$$

where the notations  $t_a = (t_1+t_2)/t_2$  and  $t_b = t_1/t_2$  were introduced. Using Equation (48), we can subtract the second equation from the first in order to eliminate  ${}^1\dot{\sigma}_2$  and  ${}^2\dot{\sigma}_2$ . In matrix form we then get

$${}^1\mathbf{a}{}^1\hat{\boldsymbol{\epsilon}} = {}^1\mathbf{b}\dot{\boldsymbol{\epsilon}}^* \quad (61)$$

with

$$\begin{aligned} {}^1\mathbf{a} &= \left[ {}^1D_{22} + {}^2D_{22}t_b \quad {}^1D_{24} + {}^2D_{24}t_b \quad {}^1D_{26} + {}^2D_{26}t_b \right] \\ {}^1\hat{\boldsymbol{\epsilon}} &= \left[ {}^1\dot{\epsilon}_2 \quad {}^1\dot{\epsilon}_4 \quad {}^1\dot{\epsilon}_6 \right]^T \\ {}^1\mathbf{b} &= \left[ {}^2D_{21} - {}^1D_{21} \quad {}^2D_{22}t_a \quad {}^2D_{23} - {}^1D_{23} \quad {}^2D_{24}t_a \quad {}^2D_{25} - {}^1D_{25} \quad {}^2D_{26}t_a \right] \\ \dot{\boldsymbol{\epsilon}}^* &= \left[ \dot{\epsilon}_1^* \quad \dot{\epsilon}_2^* \quad \dot{\epsilon}_3^* \quad \dot{\epsilon}_4^* \quad \dot{\epsilon}_5^* \quad \dot{\epsilon}_6^* \right]^T \end{aligned}$$

In order to keep the number of arithmetic expressions to a minimum, we will only show this part of the derivation and simply conclude that the above calculations can be performed in a completely analogous way for the remaining unknown stress components  ${}^1\dot{\sigma}_4$ ,  ${}^2\dot{\sigma}_4$ ,  $\dot{\sigma}_4^*$ ,  ${}^1\dot{\sigma}_6$ ,  ${}^2\dot{\sigma}_6$  and  $\dot{\sigma}_6^*$ . The result can be written

$$\begin{bmatrix} {}^1\mathbf{a} \\ {}^2\mathbf{a} \\ {}^3\mathbf{a} \end{bmatrix} {}^1\hat{\boldsymbol{\epsilon}} = \begin{bmatrix} {}^1\mathbf{b} \\ {}^2\mathbf{b} \\ {}^3\mathbf{b} \end{bmatrix} \boldsymbol{\epsilon}^* \quad (62)$$

and with obvious notation we arrive at

$$\mathbf{A} {}^1\hat{\boldsymbol{\epsilon}} = \mathbf{B} \boldsymbol{\epsilon}^* \quad (63)$$

The explicit form of the matrices  $\mathbf{A}$  and  $\mathbf{B}$  are

$$\mathbf{A} = \begin{bmatrix} {}^1D_{22} + {}^2D_{22}t_b & {}^1D_{24} + {}^2D_{24}t_b & {}^1D_{26} + {}^2D_{26}t_b \\ {}^1D_{42} + {}^2D_{42}t_b & {}^1D_{44} + {}^2D_{44}t_b & {}^1D_{46} + {}^2D_{46}t_b \\ {}^1D_{62} + {}^2D_{62}t_b & {}^1D_{64} + {}^2D_{64}t_b & {}^1D_{66} + {}^2D_{66}t_b \end{bmatrix} \quad (64)$$

$$\mathbf{B} = \begin{bmatrix} {}^2D_{21} - {}^1D_{21} & {}^2D_{22}t_a & {}^2D_{23} - {}^1D_{23} & {}^2D_{24}t_a & {}^2D_{25} - {}^1D_{25} & {}^2D_{26}t_a \\ {}^2D_{41} - {}^1D_{41} & {}^2D_{42}t_a & {}^2D_{43} - {}^1D_{43} & {}^2D_{44}t_a & {}^2D_{45} - {}^1D_{45} & {}^2D_{46}t_a \\ {}^2D_{61} - {}^1D_{61} & {}^2D_{62}t_a & {}^2D_{63} - {}^1D_{63} & {}^2D_{64}t_a & {}^2D_{65} - {}^1D_{65} & {}^2D_{66}t_a \end{bmatrix} \quad (65)$$

The solution of Equation (63) is found by inversion of  $\mathbf{A}$  and we finally obtain the solution sought

$${}^1\hat{\boldsymbol{\epsilon}} = \mathbf{A}^{-1} \mathbf{B} \boldsymbol{\epsilon}^* \quad (66)$$

We can now calculate the unknown strains in the respective layer for a given state of homogenised strains. The strains in layer 2 are calculated by simply inserting  $\hat{\boldsymbol{\epsilon}}$  and  $\boldsymbol{\epsilon}^*$  into (49)–(49). The expression for  $(\mathbf{A}^{-1} \mathbf{B})$  is extremely lengthy for the general, anisotropic, case. For the case of both material stiffnesses  ${}^1\mathbf{D}$  and  ${}^2\mathbf{D}$  being orthotropic, the general case reduces to a somewhat more handy expression:

$$\begin{bmatrix} \frac{{}^2D_{21} - {}^1D_{21}}{{}^1D_{22} + {}^2D_{22}t_b} & \frac{{}^2D_{22}t_a}{{}^1D_{22} + {}^2D_{22}t_b} & \frac{{}^2D_{23} - {}^1D_{23}}{{}^1D_{22} + {}^2D_{22}t_b} & 0 & 0 & 0 \\ 0 & 0 & 0 & \frac{{}^2D_{44}t_a}{{}^1D_{44} + {}^2D_{44}t_b} & 0 & 0 \\ 0 & 0 & 0 & 0 & 0 & \frac{{}^2D_{66}t_a}{{}^1D_{66} + {}^2D_{66}t_b} \end{bmatrix} \quad (67)$$

The above derivation of the strain decomposition is equivalent to applying cyclic boundary conditions to a part of the bondline of an infinitesimal area  $dx \cdot dy$ , and assuming the stresses and strains to be constant within each layer. The resulting strain states are equivalent to those obtained for a two-element mesh (with cyclic boundary conditions applied) as the one depicted in Figure 8. The example shows a nominal uniaxial shear strain in the homogenised material, which is decomposed into the shear strains of the two layers. In this example, the stiffness matrices for the two layers were assumed to be anisotropic. This results in that the nominal shear strain of the homogenised material is decomposed into shear strains of opposite signs in the two layers.

In order to use the above described decomposition scheme for general incremental solution procedures, we must for each increment not only perform the strain and stress decomposition but also calculate the tangential stiffness matrices of the materials. We



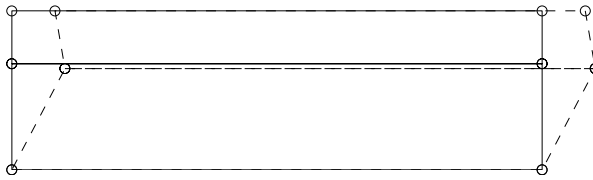


Figure 8: Homogenised pure shear.

assume that we have obtained, from a previous increment, an estimate of the stiffness matrices. Typically, in a finite element implementation, we must now, for given homogenised strain increments, calculate the new homogenised stiffness matrix and the corresponding stresses. First we use Equation (63) to calculate the layerwise strains for six uniaxial, adjoint, strain rates, e.g.  $\dot{\epsilon}^* = [\dot{\epsilon}_{xx}^* \ 0 \ 0 \ 0 \ 0 \ 0]^T$ ,  $[0 \ \dot{\epsilon}_{yy}^* \ 0 \ 0 \ 0 \ 0]^T$  etc. In this strain decomposition, we use the last known estimate of the tangential stiffness matrix. Following this, Equation (46) is used to calculate the corresponding stress rates in the respective layers. Finally, we calculate the stress rates in the homogenised material, using Equations (48) and (53)–(55). The vector formed with the six homogenised stress rates divided by the strain component now equals the columns of the new estimate of the tangential stiffness matrix. Repeating this scheme for all the fundamental strain states results in the complete tangential stiffness matrix. Thus we have obtained the first estimate of the strain decomposition within this increment and a new estimate of the tangential stiffness matrix. The above procedure is repeated until a suitable error norm, of e.g. the homogenised stresses, in two subsequent steps has converged.

## 3 Results and Discussion

In this section, the interface model presented is tested for some fundamental uniaxial loading states as well as for general multiaxial states. In the implementation, the model response is expressed in terms of stress vs. displacement instead of stress vs. strain.

### 3.1 Interface Responses

#### 3.1.1 General Remarks

For clarity, we consider the case of plane conditions, i.e. we disregard the influence of any stresses or strains in the  $z$ -direction, cf. Figure 3. We furthermore project the interface layer response on a zero thickness. Due to the zero thickness we also disregard the influence of the longitudinal normal stress,  $\sigma_{xx}$ . Thus the remaining stress components are  $\sigma_{yy}$  and  $\sigma_{xy}$ . From tests on bondlines we assume to have derived the response curves  $\sigma$  vs.  $\epsilon^d$  for the two stresses considered. This can be done if we know the response of the adhesive bulk and assume this response to be elasto-plastic. Alternatively, we can use an analytical expression based on, e.g. Weibull theory, as mentioned in the introduction.

We will refer to some of the loading paths discussed below as being monotonic. By this is meant a loading path such that damage is always increasing, i.e.  $\dot{\omega}_{yy} > 0$  and  $\dot{\omega}_{xy} > 0$ .

### 3.1.2 Uniaxial Response

From previous research results [17, 22] we use as input the stress vs. deformation of the interface response according to the piecewise linear approximation of Figure 9. It is assumed that these curves correspond to the behaviour at uniaxial loading i.e. at zero shear and normal deformation respectively. With the current modelling, this uniaxial loading, will give the same result as uniaxial stress loading, if the dilatation is set to zero. The curves in Figure 9 are piecewise linear approximations of test results obtained on wood-to-wood adhesive bondlines glued with a phenol-resorcinol adhesive [22, 22], and they are also close to what one would expect for solid wood [2]. Here, four linear parts are used for each uniaxial curve, but any number could be used.

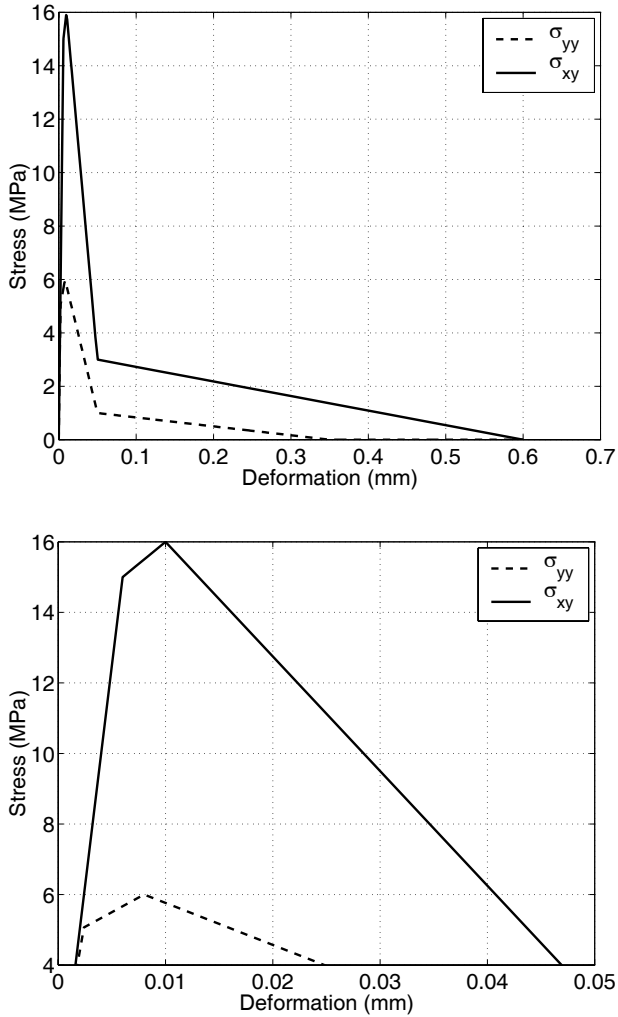


Figure 9: Upper: Stress vs. deformation. Lower: Magnification of the region close to peak stress.

For the uniaxial cases we obtain the  $\omega_{xy}$  and  $\omega_{yy}$  curves shown in Figure 10. In uniaxial, monotonic loading we obtain, of course, curves identical to those in Figure 9, since they are the starting-point of the model. However, for non-monotonic loading we get the responses of Figure 11 for the case of the coefficient of friction,  $\mu$  and the dilatation constant,  $\eta^0$ , both being zero. Figure 12 shows the response for the same cyclic loading paths for  $\mu=0.5$  and  $\eta^0=0.1$  with the shear stress curve from Figure 9 given again for comparison (dashed-dotted). The dilatation was assumed to depend linearly on shear deformation as defined in Figure 7 with  $\gamma_1$  being defined by the linear elastic limit and  $\gamma_2$  by the strain at the sharp break-point of the shear stress-deformation curve (the deformation at this point is 0.05 mm).

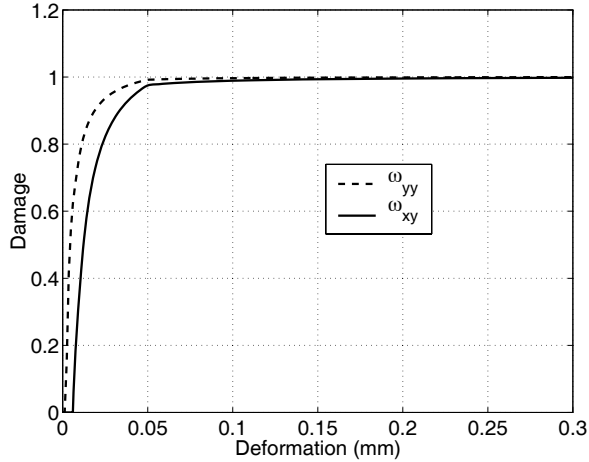


Figure 10: Damage vs. deformation in uniaxial loading

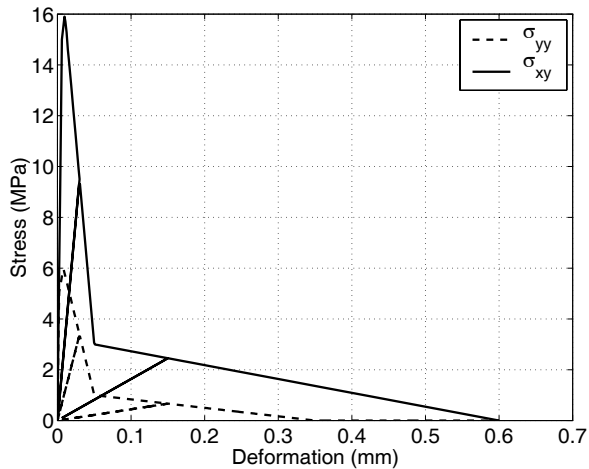


Figure 11: Stress vs. deformation for two uniaxial loading paths. Cyclic loading.  $\mu = 0$ ,  $\eta=0$ .

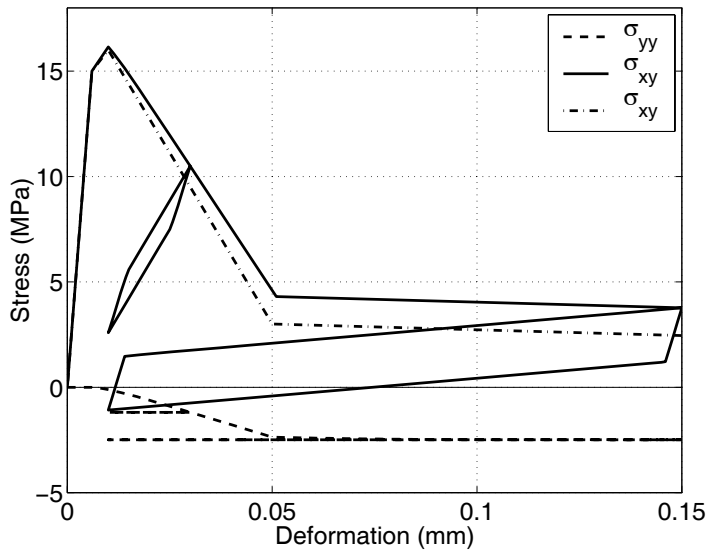
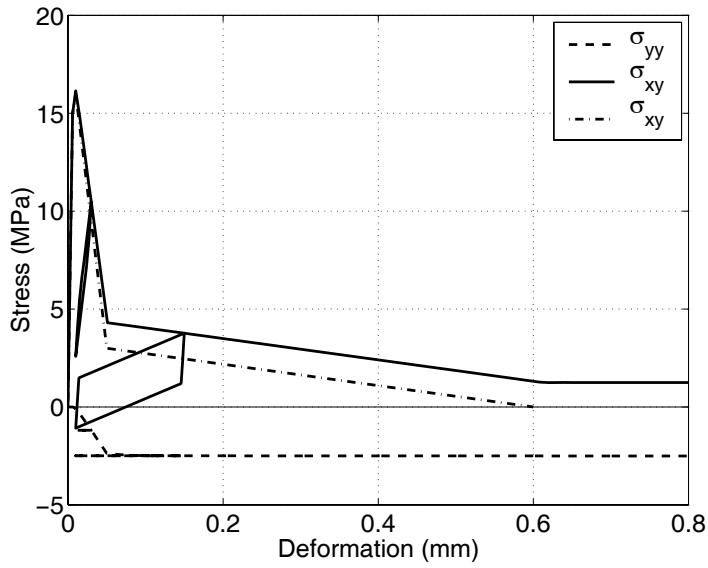


Figure 12: Upper: Stress vs. shear deformation in uniaxial shear ( $\epsilon_{yy}=0$ ). Cyclic loading in pure shear. Solid and dashed lines are for  $\mu=0.5, \eta=0.1$ , while the dashed dotted line is for the case of  $\mu=\eta=0$ . Lower: Magnification of the upper curves.

### 3.1.3 Mixed-mode Response

For mixed-mode loading, we have to define the powers in the interaction expression, cf. Equations (23) and (24). Here we assume that  $m = n = 2$ , which has shown to give a reasonable fit for the strength of a PR adhesive [22, 17]. For monotonic loading paths, it is then possible to represent the stresses as surfaces in strain space. This is shown in Figure 13 for the case of  $\mu$  and  $\eta^0$  both being zero.

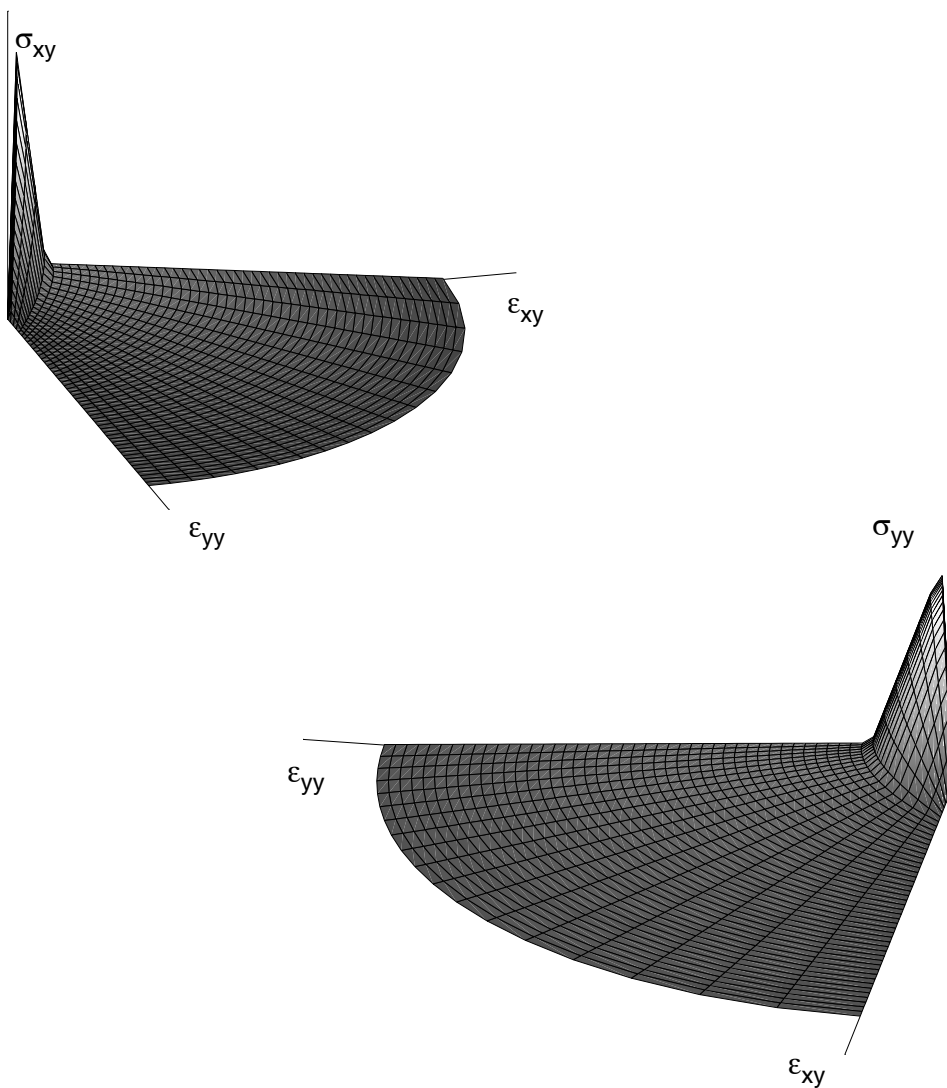


Figure 13: Stress-deformation response for monotonic loading.

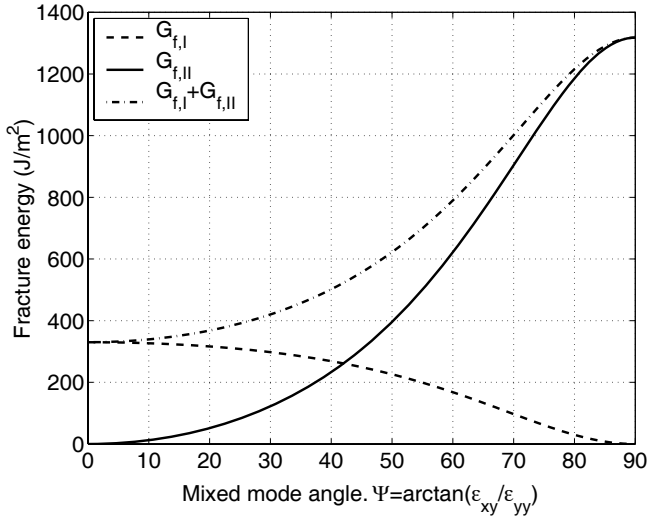


Figure 14: Fracture energy vs. mixed mode angle in radial, monotonic loading.

For monotonic loading paths the present model is path independent in terms of stress and deformation, but the amount of dissipated energy is path dependent. Since the fracture energies in mode I and II are different, it is possible to predict the dependence of fracture energy on the loading direction for radial loading paths. In Figure 14 this dependence of the fracture energy, as predicted by the current model, is shown for monotonic paths.

### 3.1.4 A Typical Loading Path

For many applications a typical loading path for the most stressed parts of a bondline is far from radial. Considering the end of a single overlap joint, we can conclude that initially, due to bending effects, the loading must include both peel stresses perpendicular to the bondline as well as shear stresses. As the loading continues, the amount of loading perpendicular to the bondline is gradually reduced, so that at maximum load a state of pure shear is almost obtained. The amount of loading perpendicular to the bondline depends mainly on the joint geometry and adherend material stiffness, but also to some extent on the bondline response.

In order to show the present interface modelling response of such a general loading path, we use the one depicted in Figure 15. This path initially follows a mixed-mode loading with an equal amount of shear slip and normal opening. At subsequent loading, the direction is increasingly dominated by pure shear slip. The response in terms of stress versus shear slip is shown in Figure 16. Both  $\mu$  and  $\eta^0$  were assumed to be zero.

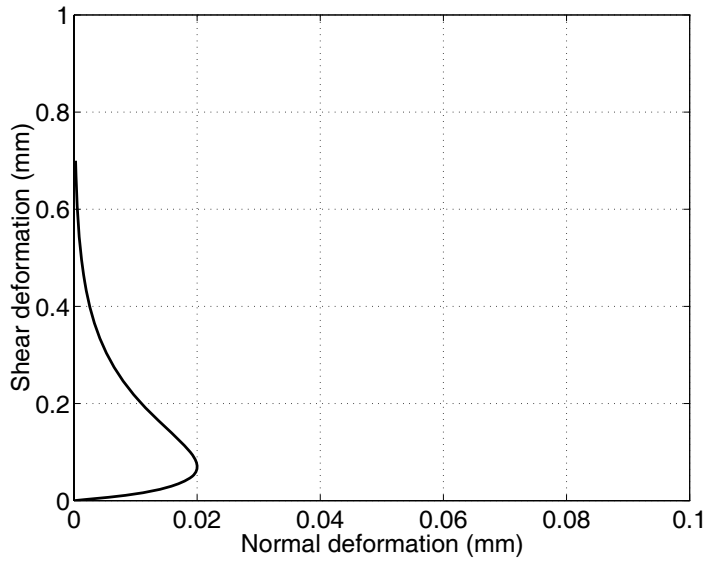


Figure 15: Non-radial deformation path. Note the different scales on the axes.

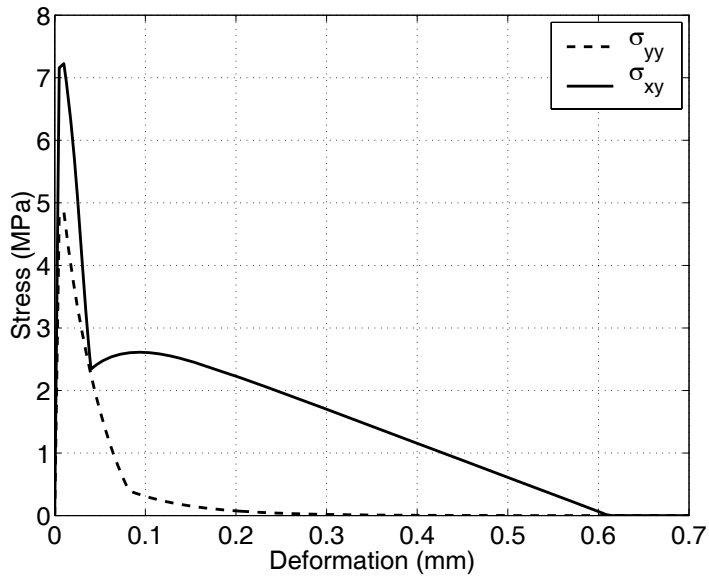


Figure 16: Stress vs. deformation response for the non-radial path depicted in Figure 15.

## 3.2 Conclusions and Future Developments

### 3.2.1 Conclusions

This paper can be summarised in the following concluding remarks:

- A new, damage-based, interface model for wood adhesive bonds, which includes the phenomena of joint dilatation and friction was developed
- A decomposition scheme was proposed, in order to use the interface model together with a plasticity model to obtain a homogenised “bondline” material.

### 3.2.2 Future Developments

The following aspects have not been covered in this paper but should present an interesting challenge for future research.

- The modelling approach presented has a phenomenological background, which is related to the micro-structure of wood adhesive bonds, but the concept should, in principle, be possible to apply to other situations such as modelling the fracture of solid wood.
- The implementation of the model into finite element codes.
- The use of plasticity theory for the wood adhesive. We left unspecified the plasticity model to use, but in general, any model which can be expressed in the strain-driven format of Equation (44) could be used.
- It is still an open question how to implement the strain-decomposition scheme in practice. However, a possible strategy has been outlined, although it has not been tested.
- The development of a material model should be accompanied by test results in order to verify it.

## 4 Acknowledgements

The financial support by the Swedish Council for Building Research (BFR project no. 19960633), which made this work possible, is gratefully acknowledged. A special thanks is also directed to Dr. Micael Stehr at the Division of Wood Technology and Processing at the Royal Institute of Technology, Stockholm, for supplying the electron microscope picture.



## References

- [1] Borg, R., *An Orthotropic Material Model with Damage*. Thesis No. 703. LIU-TEK-LIC-1998:38. Division of Solid Mechanics, Department of Mechanical Engineering, Linköping University, Linköping, Sweden, 1998.
- [2] Boström, L., *Method for Determination of the Softening Behaviour of Wood and Applicability of a Nonlinear Fracture Mechanics Model*. Report TVBM-1012, Division of Building Materials, Lund University, Sweden, 1992.
- [3] Daudeville, L., *Fracture in spruce: experiment and numerical analysis by linear and nonlinear fracture mechanics*. Holz als Roh- und Werkstoff, 57 pp. 425–432, 1999.
- [4] Edlund, U., *Mechanical Analysis of Adhesive Joints: Models and Computational Methods*. Dissertations No. 291. Division of Solid Mechanics, Department of Mechanical Engineering, Linköping University, Linköping, Sweden, 1992.
- [5] Gustafsson, P. J., *Analysis of generalized Volkersen-joints in terms of non-linear fracture mechanics*. In: Mechanical Behaviour of Adhesive Joints, pp. 323–338. Edition Pluralis, Paris, France 1987.
- [6] Jefferson, A. D., *Plastic-Damage Model for Interfaces in Cementitious Materials*. Journal of Engineering Mechanics, ASCE, 124(7) pp. 775–782, 1998.
- [7] Kinloch, A. J., *Adhesion and Adhesives. Science and Technology*. Chapman and Hall, London, UK, 1990.
- [8] Krajcinovic, D., *Damage mechanics*. Mechanics of Materials 20(4) pp. 125–152, 1995.
- [9] Malvern, L. E., *Introduction to the Mechanics of a Continuous Medium*. Prentice-Hall, Inc. Englewood Cliffs, New Jersey, USA, 1969.
- [10] Marra, A. A., *Technology of Wood Bonding. Principles in practice*. Van Nostrand Reinhold, New York, USA, 1992.
- [11] Matzenmiller, A., *A constitutive model for anisotropic damage in fiber-composites*. Mechanics of Materials 8(2) pp. 117–197, 1989.
- [12] Ožbolt, J. and Aicher, S., *Macroscopic modeling of wood using microplane theory*. In: Proc. of the Int. Conf. on Wood and Wood Fiber Composites. Edited by S. Aicher. pp. 253–264. COST Action E8, Otto-Graf Institute, University of Stuttgart, Germany, 2000.
- [13] Ottosen, N. S. and Olsson, K-G., *Hardening/Softening Plastic Analysis of Adhesive Joint*. Journal of Engineering Mechanics, ASCE, 114(1) pp. 97–116, 1988.
- [14] Ristinmaa, M. and Ottosen, N. S., *Large Strain Plasticity and Thermodynamics*. Solid Mechanics Report TFHF-3072. Solid Mechanics, Lund University, Sweden, 1996.

- [15] Stehr, M., *Adhesion to Machined and Laser Ablated Wood Surfaces*. Doctoral thesis. Report TRITA-TRÄ R-99-42. Division of Wood Technology and Processing, Department of Manufacturing Systems, Royal Institute of Technology, Sweden, 1999.
- [16] Stehr, M., *Laser Ablation of Machined Wood Surfaces. Part 2. Effect on End-Grain Gluing of Pine (*Pinus silvestris* L.)*. *Holzforschung*, 53 pp. 655–661.
- [17] Serrano, E., *Finger-joints for laminated beams. Experimental and numerical studies of mechanical behaviour*. Report TVSM-3021, Lund University, Division of Structural Mechanics 1997.
- [18] Serrano, E., *Glued-in rods for timber structures. A 3-D model and finite element parameter studies*. Accepted for publication. *International Journal of Adhesion and Adhesives*.
- [19] Serrano, E., *Glued-in rods for timber structures. An experimental study of softening behaviour*. Submitted for publication. *Materials and Structures*.
- [20] Serrano, E. and Gustafsson, P. J., *Influence of bondline brittleness and defects on the strength of timber finger-joints*. *International Journal of Adhesion and Adhesives*. 19(1) pp. 9–17, 1999.
- [21] Volkersen, O., *Die Nietkraftverteilung in Zugbeanspruchten Nietverbindungen mit Konstanten Laschenquerschnitten*. *Luftfahrtforschung*, (15) pp. 41–47, 1938.
- [22] Wernersson, H., *Fracture characterization of wood adhesive joints*. Report TVSM-1006, Lund University, Division of Structural Mechanics 1994.